Journal of
Materials Chemistry A

Materials for energy and sustainability

Accepted Manuscript

This article can be cited before page numbers have been issued, to do this please use: A. Balakrishnan, M. Tom, N. Rajamohan, B. Weng, F. P. Mathew, M. M. Varghese, M. Chinthala and A. K. S. Che, *J. Mater. Chem. A*, 2026, DOI: 10.1039/D5TA07511D.

ROYAL SOCIETY OF CHEMISTRY

rsc.li/materials-a

View Article Online
DOI: 10.1039/D5TA07511D

Engineered Cellulose-Supported Photocatalysts for Clean Energy and Environmental Remediation: Progress and Prospects

Akash Balakrishnan[1*], Frency P. Mathew[1], Milan Tom Joseph[1], Mona Mary Varghese[1], Aryamol K.S.[1], Mahendra Chinthala[2], Natarajan Rajamohan[3**], Bo Weng[4,5***]

[1]Innovative Catalysis and Sustainability Group, Department of Chemical Engineering, Saintgits College of Engineering (Autonomous), Kottayam, Kerala 686532, India

[2]Process Intensification Laboratory, Department of Chemical Engineering, National Institute of Technology Rourkela, Odisha 769 008, India

[3]Chemical Engineering Section, Faculty of Engineering, Sohar University, Sohar, Oman

[4]State Key Laboratory of Advanced Environmental Technology, Institute of Urban Environment, Chinese Academy of Sciences, Xiamen 361021, P.R. China

[5]University of Chinese Academy of Sciences, Beijing 100049, China

Corresponding authors Email: akash.balakrishnan@saintgits.org (Akash Balakrishnan); rnatarajan@su.edu.om (Natarajan Rajamohan); bweng@iue.ac.cn (Bo Weng)

View Article Online
DOI: 10.1039/D5TA07511D

Abstract

The growing global demand for sustainable energy and environmental remediation has accelerated interest in efficient, metal-free photocatalysts. Cellulose, with its abundance, biodegradability, tunable chemistry, high surface area, and mechanical robustness, has emerged as an ideal support material for photocatalytic systems. This review presents a comprehensive evaluation of cellulose-supported photocatalysts, detailing their structural forms, physicochemical properties, preparation strategies, and design principles. The classification into cellulose-based composites and structured architectures such as hydrogels, aerogels, membranes, and sponges highlights the versatility of cellulose in enhancing catalyst dispersion, charge separation, visible-light activity, and reusability. The applications include hydrogen and hydrogen peroxide generation, nitrogen fixation, CO_2 reduction, wastewater treatment, and disinfection. Strengths, weaknesses, opportunities, and threats (SWOT) analysis provide insights into strengths, limitations, and research gaps, emphasizing challenges in large-scale fabrication, stability, and commercial viability. Furthermore, the review highlights the significance of environmental and economic analyses to guide sustainable scale-up and market adoption. Future directions focus on heterostructure engineering, defect modulation, green synthesis, AI-guided optimization, and integration into real-world systems. By bridging materials science, catalysis, and environmental engineering, cellulose-supported photocatalysts hold significant potential for scalable, eco-friendly, and multifunctional solutions in agreement with the fundamentals of circular economy, green chemistry, and the United Nations Sustainable Development Goals.

Keywords: Catalyst; Environmental; Energy; Photocatalysis; SWOT analysis

View Article Online
DOI: 10.1039/D5TA07511D

1. Introduction

The accelerating convergence of global energy insecurity and environmental degradation driven by unchecked industrialization, urban sprawl, and fossil fuel dependence has intensified the demand for transformative solutions that can safeguard both ecological integrity and human well-being. [1,2]. The conventional systems for energy production and wastewater treatment are no longer sufficient to meet the rising expectations for sustainability, particularly under the framework of the United Nations Sustainable Development Goals [3]. The emergence of persistent organic pollutants, antibiotic-resistant microbes, and the limited scalability of traditional treatment technologies further exacerbates this shortfall [4,5]. Simultaneously, the intermittent nature of renewable energy sources underscores the need for integrative systems that offer both environmental remediation and energy valorization [6]. Bridging this gap necessitates multifunctional, low-cost, sustainable, and environmentally benign technologies that can integrate clean energy generation with efficient pollutant mitigation [7].

In this context, photocatalysis have emerged as efficient method for the mineralization of noxious contaminants and in energy-related applications such as hydrogen generation and nitrogen fixation [8–11]. Despite different photocatalysts, such as TiO_2 [8], ZnO [12], ZnS [13], CdS [14], g-C_3N_4 [15], In_2S_3[16] and WO_3 [17] are commonly employed for energy and environmental remediation due to their higher redox potential and stability, but these catalysts face several practical challenges that limit their real-world applications [18]. The key issues include limited absorption of the visible light spectrum as seen in TiO_2 and ZnO, minimal adsorption capacity against recalcitrant compounds, recombination of charge carriers, poor catalyst dispersion in aqueous media, tedious and difficult catalyst recovery, and reusability [19–21]. Moreover, specific catalysts like CdS raise toxicity concerns, which further restrict their environmental applicability, mandating the need for environmentally benign and efficient photocatalysts [22]. Doping [23], co-doping [24], heterojunction construction [25], defect engineering [26], and morphology control [27] proposed to overcome the limitations of photocatalysts. These approaches have proven effective in enhancing visible light harvesting, charge separation, and efficiency [28]. However, incorporating suitable support materials can further enhance catalyst stability, prevent aggregation, improve pollutant adsorption, and facilitate catalyst recovery and reuse, making the system more practical and efficient for real-world applications [29,30].

The concept of using support materials plays a crucial role in advancing photocatalytic systems, particularly by enhancing catalyst stability, reusability, and recovery in aqueous media [31]. Conventional supports such as silica, clay, perlite, and synthetic polymers have been utilized to mitigate challenges like catalyst aggregation and poor separation [18]. Notably, biopolymers have gained attention as eco-friendly alternatives, with cellulose standing out due to its abundance, renewability, and unique physicochemical features [32]. Its higher surface area, excellent hydrophilicity, tunable porosity, mechanical flexibility, and chemical modifiability make it highly effective in anchoring photocatalysts, improving pollutant adsorption, light harvesting, and reusability [33]. Additionally, cellulose is environmentally benign, cost-effective, and compatible with green fabrication methods, making it highly attractive for scalable energy and environmental technologies [34]. These unique attributes of cellulose-supported photocatalysts make them capable in energy generation and ecological remediation [30,35,36]. The publication trend from 2015 to 2025 shows a steady rise in research output, peaking in 2023 before gradually declining in the subsequent years. This pattern

View Article Online
DOI: 10.1039/D5TA07511D

highlights a period of accelerated research activity and collaboration during 2020–2023, likely influenced by increased focus on emerging scientific challenges. The recent decline suggests a stabilization phase, indicating scope for renewed strategies to sustain consistent contributions (**Fig. 1**). However, a comprehensive review of cellulose-supported photocatalysts specifically tailored for energy and environmental applications is still lacking.

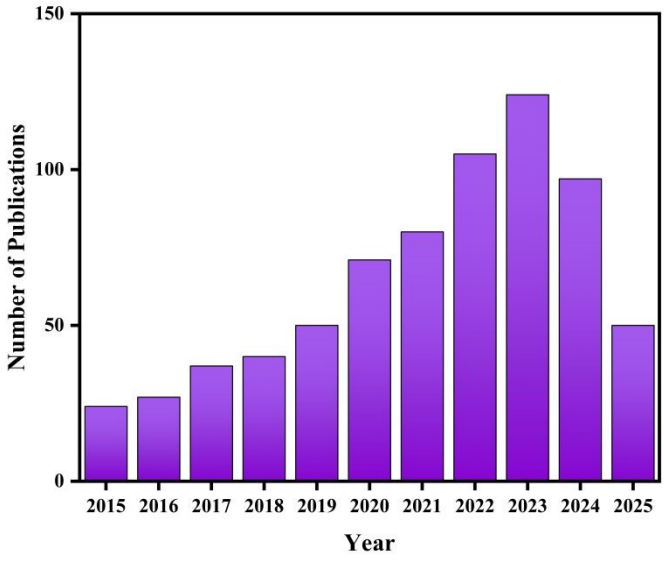

Fig. 1. Annual publication trends on cellulose photocatalysts from 2015 to 2025 (Source: Web of Science)

This review paper emphasizes recent advancements in cellulose-supported photocatalysis for energy and environmental applications (**Fig. 2)**. It begins with detailed insights into photocatalytic mechanisms, along with a critical evaluation of the common challenges and limitations in existing photocatalytic systems. A dedicated section focuses on cellulose, describing its types, structural features, and physicochemical properties relevant to composite formation. The review also discusses why cellulose is an ideal support material, highlighting its natural abundance, renewability, high surface area, mechanical strength, chemical modifiability, and biocompatibility, which together enhance photocatalyst dispersion, stability, and reusability. This is followed by an in-depth analysis of cellulose-supported photocatalysts, including key design considerations and preparation methods. Various categories of cellulose-supported catalysts are examined, such as metal oxide-based, metal sulfide-based, metal-organic frameworks (MOFs), hydrogels, aerogels, and membranes. The review explores their wide-ranging applications, including photocatalytic hydrogen peroxide generation, hydrogen production, nitrogen fixation, carbon dioxide reduction, wastewater treatment, and disinfection. The final section outlines the advantages, limitations, and prospects of these systems, offering insights into their potential for scalable, multifunctional photocatalytic technologies.

View Article Online
DOI: 10.1039/D5TA07511D

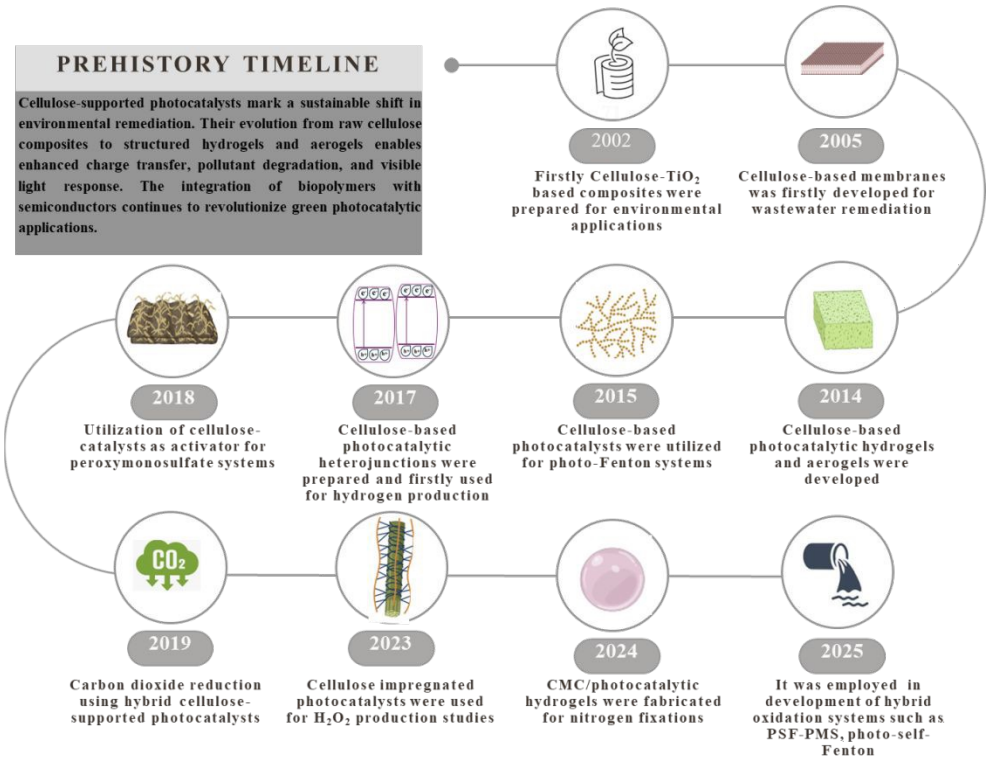

Fig. 2 Milestones in the evolution of cellulose-supported photocatalysts from 2002 to 2025. The timeline highlights key innovations ranging from early TiO_2-cellulose composite and wastewater membranes to modern hybrid systems enabling energy generation and multi-pollutant degradation. This chronological progression reflects the growing sophistication and multifunctionality of cellulose-integrated photocatalytic systems.

2. Photocatalysis

Photocatalysis is emerging as a cost-effective and environmentally sustainable strategy for both energy and environmental applications. For broader adoption, photocatalysts must be optimized to achieve high quantum yields, broad-spectrum light absorption, and enhanced reaction selectivity [37]. Advancing photocatalytic technology requires addressing several aspects, such as band gap tuning, catalyst immobilization, morphology control, reactor efficiency, and effective charge separation [4,38]. A key determinant of photocatalyst performance is its band gap, which describes the minimum photon energy needed to initiate the photocatalytic process. The photocatalytic process begins with photon absorption, exciting electrons from the valence band to the conduction band, forming electron-hole pairs [39]. These charge carriers generate reactive oxygen species like superoxide anion ($\bullet O_2^-$), hydroxyl radical (HO•), hydrogen peroxide (H_2O_2), and hydroperoxyl radicals ($HO_2\bullet/HO_2^-$) [40,41]. These ROS oxidize pollutants, mineralize them into CO_2 and H_2O on the photocatalytic surfaces, further improving electron transfer efficiency, with oxygen acting as a key electron acceptor [42]. In oxygen-rich environments, the photocatalytic process proceeds efficiently, transforming organic pollutants into intermediate hydroxylated compounds and eventually attaining complete mineralization into carbon dioxide and water [31,43]. Simultaneously, photogenerated holes in the valence band react with donor species, further promoting the breakdown of organic matter. Pre-adsorption of oxygen and water onto the photocatalytic

View Article Online
DOI: 10.1039/D5TA07511D

surface enhances electron transfer, with oxygen serving as the primary electron acceptor in environmental remediation contexts. Thus, the interaction of ROS, free electrons, and holes with various pollutants, such as organic, inorganic, bacteria, and viruses, facilitates their complete decomposition into non-toxic by-products [44,45]. On the other hand, ROS species such as superoxide radicals undergo electron-assisted reduction reaction to yield sustainable fuels such as hydrogen, ammonia, and hydrogen peroxide, as discussed in Section 6 [46–48].

The bandgap is a fundamental property that governs the electronic behavior and light absorption capacity of photocatalysts. The practical band gap engineering is essential to maximize solar light harvesting and enhance photocatalytic activity [37]. One widely adopted approach involves modifying the photocatalytic structures by incorporating suitable dopants. While such doping can narrow the band gap and enhance visible light absorption, it may also introduce recombination centers that hinder charge carrier mobility, thereby reducing photocatalytic efficiency [49,50]. To address this, alternative strategies have been explored, such as doping, material coupling, heterojunction, and dye sensitization (**Table 1**) [20]. The photocatalysis is a multifaceted process involving simultaneous optical, electrical, and chemical interactions. While photocatalysts are central to these interactions, the efficacy of the overall process is influenced by the compatibility and stability of the support materials used. The synergy between the photocatalyst and its support is critical for maintaining optimal light utilization, separation of charge carriers, and surface reactions throughout the process [31,51].

Table 1 Comparison of different design engineering strategies adopted in photocatalysis [3,18,22,37,52,53]

Method	Explanation	Advantages	Disadvantages
Single-atom anchoring	Anchoring isolated single metal atoms (Cobalt, Nickel, etc.) onto the surface of a 2D photocatalyst to serve as active sites.	1. Improve charge separation 2. Tunable catalytic sites 3. Maximizes atom utilization	1. Complex synthesis methods 2. Stability issues 3. Single atoms may agglomerate under reaction conditions
Defect engineering	Introduction of vacancies, dislocations, or other structural defects to modify electronic and catalytic properties.	1. Enhance active site density 2. Tune the band gap 3. Improve light absorption	Defects may act as recombination centers, and controlling their concentration is challenging.
Elemental doping	The incorporation of metal or non-metals into the lattice alters the electronic structure and optical properties.	1. Expands light absorption range 2. Improve conductivity 3. Tunes band gap	Leaching of dopants and probable risk of forming unwanted recombination centers.
Coordination activation	Modifying the coordination environment around active metal sites to optimize catalytic performance.	Ensures specific reaction pathways and improves the binding of target molecules	Requires precise control over coordination chemistry.

View Article Online
DOI: 10.1039/D5TA07511D

Organic ligand modification	Attaching organic ligands or molecules to modify surface properties, band structure, and dispersion.	1. Improves solubility and dispersibility 2. Selective adsorption of reactants	The possibility of photodegradation of ligands and steric hindrances may influence active sites.
Heterojunction	Combining two or more semiconductors to form an interface that facilitates charge transfer.	Promote efficient charge separation and reduce the recombination ratio	Complexity in catalyst preparation and potential difference lattice matching.

Following the exciton dissociation, the generated free electrons and holes drive redox reactions, which are an essential step in photocatalysis. The dissociation efficacy is dependent on factors such as exciton binding energy, carrier mobility, and charge lifetime. However, structural defects in the photocatalyst can trap charge carriers, leading to recombination losses [31]. To overcome this, heterojunction structures have been extensively explored to promote charge separation and minimize recombination [54]. A heterojunction photocatalyst is formed at the interface between two semiconductors or a semiconductor and a metal with mismatched band structures and electronic properties [55]. The proper design facilitates directional charge transfer, thereby enhancing photocatalytic performance by suppressing electron-hole recombination [56]. Commonly employed heterojunction types include type- I, II, and III, p-n junction, Schottky junction, Z-scheme, S-scheme [52]. More details about different design strategies are described in **Table 1**.

Despite these advancements, the photocatalyst still faces several drawbacks that limit its real-world application. These include poor long-term stability, low efficiency under visible light, susceptibility to photocorrosion, and difficulty in recovering the catalyst after reuse, especially in liquid-phase systems [8,57]. For environmental applications, the aggregation of photocatalyst nanoparticles leads to a loss of active surface area and hinders pollutant contact, while in solar fuel production, rapid recombination of photoinduced charge carriers limits product yields [20,58]. In disinfection, reduced surface interactions with pathogens due to structural instability or fouling affect the efficacy. These challenges underscore the importance of incorporating suitable support materials that can address multiple functional needs [59]. An ideal support enhances the dispersion of photocatalyst particles, maintains structural integrity under operational conditions, improves mass transfer of reactants and products, and enables ease in recovery and reusability [60]. Moreover, it can actively assist in interfacial charge separation, prolong carrier lifetimes and facilitate reaction pathways via synergistic interactions [61].

An ideal support material for environmental applications must meet several key criteria to ensure effective and stable photocatalysis. It should be chemically stable, non-toxic, and have low water solubility to prevent degradation and secondary contamination [62]. Hydrophobicity is essential for attracting organic pollutants, while a dielectric constant in the range of 2.2 to 3.5 helps minimize charge loss. Strong adhesion with the photocatalyst prevents particle detachment, and transparency ensures maximum light utilization [31]. Additionally, flexibility allows application on curved surfaces, and a high surface area enhances interactions with pollutants. These requirements can be grouped into two categories: (a) practical aspects such as chemical stability, reusability, and cost-effectiveness, and (b) features

View Article Online
DOI: 10.1039/D5TA07511D

that enhance photocatalytic performance, including efficient light harvesting, reduced charge recombination, and improved contact with contaminants. Commonly employed photocatalytic supports are silica, glass, alumina, carbon, zeolite, and biopolymers [5]. Based on comparative analysis of different supports (**Table 2**), biopolymers are ideal support materials for photocatalytic applications due to their abundance, renewability, and biodegradability, making them both sustainable and safe [63]. It offers excellent chemical stability and low water solubility, ensuring durability without leaching into treated water. Its high surface area and porous structure enhance pollutant adsorption and photocatalytic activity, while its modifiable surface allows strong adhesion with photocatalysts and tunable hydrophobicity [64,65]. Biopolymers can also facilitate electron transfer due to the presence of OH groups that can interact with photocatalysts, aiding in charge separation and reducing electron-hole recombination [66]. Biopolymers are flexible for use in various reactor configurations, such as thin films, hydrogel, aerogel, composite, and membrane, fulfilling both practical and photocatalytic efficiency requirements [61,67,68]. Among different biopolymers, cellulose is often explored as a versatile biopolymer for energy and environmental applications.

Table 2 Comparative evaluation of different photocatalytic supports such as organic, inorganic, polymeric, biopolymers, and hybrid supports

Parameters	**Supports**				
	Inorganic	***Organic***	***Polymers***	***Biopolymers***	***Hybrid supports***
Examples	TiO_2, SiO_2	Biochar, Graphene oxide	Polyvinyl alcohol, Polyacrylonitrile	Cellulose, Chitosan, and Alginate	MOFs, COFs, and Carbon nitride
Surface area	□	□	□	□	□
Porosity	●	□	□	□	□
Light permeability	●	●	□	□	●
Biodegradability	●	●	●	□	●
Hydrophilicity	□	□	□	□	□
Adsorption potential	□	□	□	□	□
Chemical Versatility	●	□	□	□	□
Charge transfer	□	□	□	□	□
Stability	□	□	□	□	□

View Article Online
DOI: 10.1039/D5TA07511D

Sustainability	●	●	●	□	●
Cost efficiency	□	□	□	□	●
Green compliance	●	●	●	□	●
Thermal stability	□	□	□	□	□
Reusability	□	□	□	□	□
ROS support capability	□	□	□	□	□
Mechanical strength	□	□	□	□	□
Pollutant Selectivity	●	□	□	□	□
Overall rating	□	□	□	□	□

Where □ is good, □ is average and ● is poor

3. Cellulose

Cellulose is the most abundant biopolymer in the world [5]. It is made up of D-glucose monomers $(C_6H_{10}O_5)_n$, which are connected through the β(1→4) glycosidic bonds. The value of n is attributed to the degree of polymerization, which ranges from 10,000 to 15,000, based on cellulose source [69].Its structure is stabilized by extensive intra- and intermolecular hydrogen bonding, yielding a semi-crystalline, mechanically robust, flexible, and biodegradable material sustainable for sustainable applications [5,32]. The dense hydrogen-bonding network imparts excellent barrier properties, enabling its use in packaging, biomedical systems, and environmental remediation [33]. Cellulose can be engineered into various structural forms such as thin films [70], membranes [71], hydrogels [36], aerogels [72], fibers [73], nanoparticles [74], and even 3D-printed architectures [75], making it a versatile platform for integrating photocatalysts in environmental processes.

Cellulose occurs in multiple polymorphic forms (Iα, Iβ, II, III, IV, V, VI), each with distinct stability and structural characteristics [33,76]. The metastable Iα polymorph, predominantly found in algae and bacterial cellulose, can partially transform into the more stable Iβ form through hydrothermal annealing at 260 °C under basic conditions, although the conversion is often incomplete. Cellulose Iβ, the dominant form in higher plants, is the most abundant natural polymorph and is widely studied for industrial applications. Cellulose II, the thermodynamically stable polymorph, is produced via regeneration or mercerization using aqueous NaOH, enabling improved structural integrity, stability, and processability for films, fibers, and related products [77]. Cellulose III is generated from cellulose I or II through ammonia based chemical process, introducing substantial changes in physical and chemical properties [78]. Subsequent

View Article Online
DOI: 10.1039/D5TA07511D

thermal treatment converts cellulose III into cellulose IV, further enhancing stability and expanding material utility [79]. These controlled polymorphic transitions allow fine-tuning of cellulose characteristics for targeted applications. Cellulose is sourced from a wide range of renewable feedstocks, including agricultural residues, industrial waste streams, and lignocellulosic biomass such as cotton linters, wheat straw, sugar beet pulp, bagasse, municipal solid waste, corncob, and fruit/vegetable peels [80-81]. Marine tunicates (Ascidiacea; >2300 species) also provide highly crystalline cellulose. Algae and bacteria serve as important biological sources, offering unique structural variants and high purity cellulose [82].

Cellulose exists in diverse structural forms, each offering specific properties and application potential. These include wood fibres, microcrystalline cellulose (MCC), micro-fibrillated cellulose (MFC), nanocellulose, cellulose nanocrystals (CNCs), algal cellulose, bacterial cellulose, and plant fibres [83]. Bacterial cellulose, primarily produced by *Komagataeibacter xylinus*, exhibits exceptional purity, greater crystallinity, and phenomenal mechanical strength, making it highly attractive towards biomedical, food, and industrial uses [84]. Algal cellulose from red and green algae provides a renewable and biocompatible alternative source, supporting the development of sustainable materials [84]. Wood and plant fibres, typically derived from dissolved pulp, possess a hierarchical micro-scale structure (micron-diameter, millimeter-length) and comparatively lower crystallinity, making them suited for paper, textile, and composite applications [85]. **Table 3** discuss the summary of cellulose structural forms and nano-cellulosic types with key properties and applications.

Table 3 Summary of cellulose structural forms and nano-cellulosic types with preparation strategies, key properties, and applications [86–88]

Category	Types	Preparation strategy	Dimensions	Properties	Major Applications
Bulk forms	Wood/plant fibres	Mechanical pulping, chemical pulping, bleaching	Diameter µm; Length: mm	Hierarchical fibres, moderate crystallinity mechanically robust	Textile, paper, reinforcement
	Microcrystalline cellulose (MCC)	Controlled acid hydrolysis of plant fibres	10-50 µm	High crystallinity, high purity, excellent binding/compressibility	Pharmaceuticals, food, additives
	Algal cellulose	Extraction from red/green algae using alkaline treatment and purification	Varies	Renewable, biocompatible, moderate crystallinity	Biopolymers, biodegradable materials
	Bacterial cellulose (BC)	Microbial fermentation (e.g., *Komagataeibacter xylinus*) under static/ agitated culture	Nanoscale fibrillar network	High crystallinity; exceptional purity; high tensile strength; high water retention	Biomedical implants, wound dressings, membranes
Nano-cellulosic material	Cellulose nanocrystals (CNCs)	Acid hydrolysis (commonly H_2SO_4 or HCl) followed by neutralisation & ultrasonication	3–20 nm (dia.); 50–500 nm (length)	Highly crystalline, stiff, rod-like; strong optical and rheological behaviour	Catalysis, sensing, nanocomposites, packaging
	Micro-fibrillated cellulose (MFC)	High-shear mechanical fibrillation, refining, homogenisation;	10–100 nm (dia.); µm-length	Mixed crystalline–amorphous; flexible; gel-	Coatings, emulsifiers, packaging,

View Article Online
DOI: 10.1039/D5TA07511D

	sometimes enzymatic pretreatment	forming; high water-holding	biomedical scaffolds
Cellulose nanofibrils (CNFs)	Mechanical disintegration (homogenisation, microfluidisation); TEMPO-mediated oxidation optional	5–100 nm (dia.); µm-length	High aspect ratio; strong; flexible; high water retention; shear-thinning	Lightweight composites, barrier films, biomedical materials, paper reinforcement

4. Cellulose-supported photocatalysts

The integration of cellulose with photocatalysts presents a promising strategy to address the limitations of conventional photocatalysts, like lower stability, difficult recovery, and photocatalyst leaching [36]. Numerous studies have highlighted the functionalization of cellulose and its derivatives with various photocatalysts such as MOFs, COFs, carbon nitride, metal oxides, and metal sulfides, which resulted in formation of hybrid catalysts with phenomenal catalytic activity. In most cases, the hybrid systems are stabilized through hydrogen bonding, electrostatic interaction, or covalent bonding between the functional groups on cellulose and the photocatalyst surface [89]. The functional integration results in enhanced dispersion of the catalyst, improved charge separation, and an enhanced surface area leading to greater catalytic activity [66]. Along with this, cellulose also imparts flexibility, biodegradability, and mechanical reinforcement to the hybrid system. The incorporation of cellulose not only facilitates catalyst recovery and reuse but also contributes to the environmental compatibility of the overall system [90,91].

4.1 Design Criterion for Cellulose-Supported Catalysts

The rational design of cellulose-supported photocatalysts requires integrating structural, interfacial, and functional considerations to achieve high activity and operational stability. A primary requirement is establishing strong interfacial interactions between cellulose and the photocatalyst, which facilitates rapid charge transfer and suppresses electron–hole recombination. The inherent OH-rich chemistry of cellulose enables effective anchoring of semiconductor particles and allows targeted surface modification to enhance dispersion, selectivity, and stability [92]. Cellulose derivatives (like nanofibers) offer high surface area and hierarchical porosity, increasing the density of accessible active sites and promoting efficient mass transport. The coupling these supports with visible-light-responsive semiconductors such as carbon nitride, ZnO, or bismuth-based materials, and introducing heterojunctions or defect states (e.g., oxygen vacancies), further improves light harvesting and charge-separation efficiency [66,93]. The chemical crosslinking or polymer–inorganic hybridization enhances the mechanical robustness, suppresses photocatalyst leaching, and enables repeated reuse, supporting scalability for continuous applications. The environmental compatibility must also be considered; renewable cellulose and non-toxic semiconductor phases minimize secondary pollution and align with green chemistry principles. The critical design considerations are detailed as follows (**Fig. 3**) [3,94–97]

- Strong interfacial interactions: Efficient charge transfer between the cellulose support and photocatalyst is fundamental to suppress electron-hole recombination, which directly affects the photocatalytic efficacy. This

View Article Online
DOI: 10.1039/D5TA07511D

is attained through the formation of robust physical or chemical bonds at the interface, which can include hydrogen bonding, covalent bonding, or coordination interaction based on the functional group present.

- Chemical functionality of cellulose: The surface of cellulose is rich in OH groups, which provide versatile sites for chemical modification and anchoring of photocatalytic nanoparticles. The functionalization strategies, such as carboxylation and amination, can tailor surface charge, hydrophilicity, and affinity towards specific photocatalysts, improving dispersion and preventing agglomeration, thus enhancing catalytic activity and selectivity.
- Porous architecture and surface area: Cellulose derivatives such as nanofibers, aerogels, and hydrogels offer a 3D porous network with greater surface area. This structure facilitates the abundant number of catalytic sites and ensures efficient diffusion of reactants and products, which reduces mass transport limitations and enhances the photocatalytic reaction rate [82].
- Mechanical robustness and reusability: Chemical crosslinking or hybridization of cellulose with other polymers or inorganic materials significantly enhances its mechanical strength, minimizes photocatalyst leaching, and enables easy recovery and reuse. These modifications extend the catalyst's operational lifespan and lower the costs related to frequent replacement or disposal.
- Environmental compatibility and sustainability: To prevent secondary pollution, both cellulose and the photocatalytic components must be environmentally benign, biodegradable, and non-toxic. Utilizing renewable cellulose as a support material aligns with the principles of green chemistry, while minimizing hazardous substances in the photocatalyst formulation promotes safer and more sustainable applications.
- Selection of sacrificial agents: When sacrificial reagents are employed to scavenge photogenerated charge carriers and boost photocatalytic efficiency, it is essential to evaluate their influence on the system's overall stability and environmental safety. An ideal sacrificial agent should effectively enhance photocatalytic activity without accelerating catalyst degradation or producing hazardous by-products.

View Article Online
DOI: 10.1039/D5TA07511D

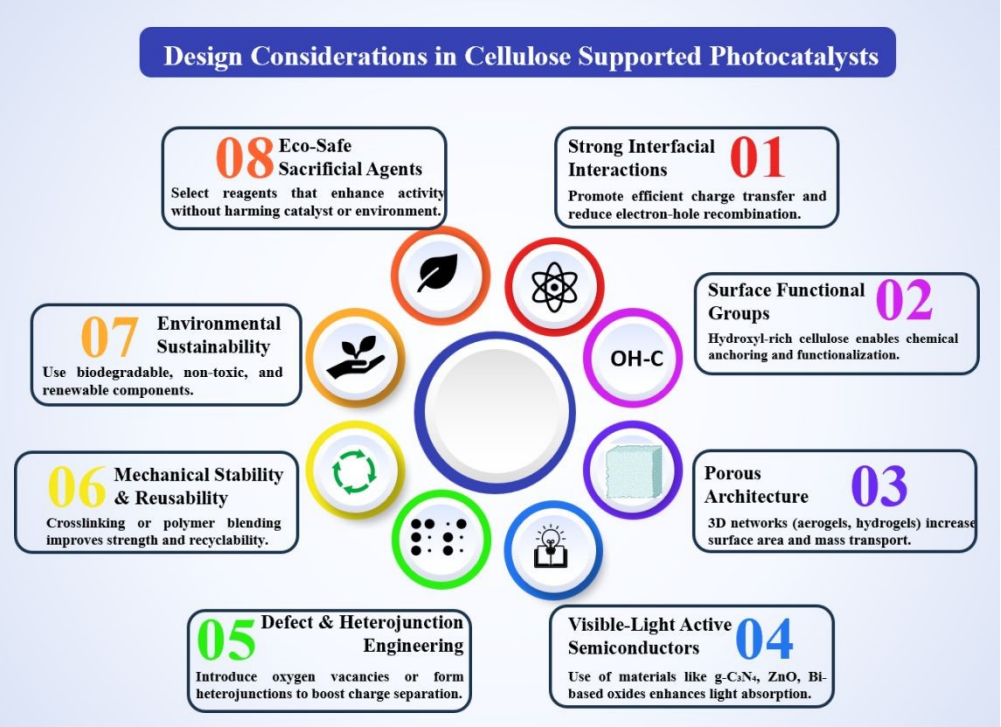

Fig. 3 Design consideration during the fabrication of cellulose-based photocatalysts

4.2 Mechanistic influence of cellulose characteristics on photocatalytic performance

The photocatalytic properties of cellulose-based photocatalysts are influenced not merely by the presence of cellulose as a scaffold, but from a synergistic interplay between its intrinsic morphological features, degree of crystallinity, surface functional chemistry, hierarchical porosity, and the nature of its interfacial electronic coupling with embedded semiconductor. Despite being intrinsically photocatalytically inert, cellulose exerts stronger mechanistic control over composite photocatalysts through its hierarchical architecture from nanofibrils to aerogels. These structural features regulate light management, charge separation, ROS generation and pollutant-catalyst interfacial reaction. The crystallinity, porosity, and surface chemistry govern catalyst dispersion, interfacial electron-hole transfer, and suppression of charge recombination.

4.2.1 Surface chemistry and functional groups

Cellulose exhibits a highly reactive surface enriched with primary, secondary, and tertiary hydroxyl groups which collectively explains the material's interfacial behavior with photocatalysts [98]. These hydroxyl functionalities behave as a versatile coordination site capable of forming hydrogen bonds, dipole-dipole interactions, and metal-ligand complexes with metal oxides, metal ions and semiconductor precursors [99]. Because the electron-rich oxygen atoms of hydroxyl groups present strong affinity towards electropositive transition-metal centers, cellulose provides a chemically active platform that directs nucleation, anchoring, and stabilization of photocatalysts. This interfacial affinity not only prevents photocatalyst agglomeration but also ensures high-density, homogeneous distribution of

View Article Online
DOI: 10.1039/D5TA07511D

photocatalyst domains, which is essential for optimizing light absorption and creating efficient charge-transfer channels in composite systems.

Apart from physical dispersion, cellulose's surface chemistry directly modulates photocatalytic charge-transfer dynamics [100]. Hydrogen-bond network facilitates proton-coupled electron-transfer enabling cellulose to transiently shuttle electrons or protons at the interface of semiconductor, which lowers interfacial charge transfer resistance [101]. The local polarity variations around the hydroxyl groups influence the band alignment of supported photocatalysts, helpful to stabilize photoexcited carriers and reduce recombination ratio [102]. Introducing additional functional groups such as carboxyl, aldehyde, sulfate, or grafted polymeric moieties further enhances metal-ion chelation, and increases nucleation site density, leading to better-defined semiconductor domains and stronger electronic coupling. These chemical modifications can tune surface charge, acidity, and redox potential, ultimately influencing radical generation pathways and reaction selectivity during photocatalysis [103].

The hierarchical distribution of functional groups in nanocellulose also amplifies these effects. CNCs offers high crystallinity and densely packed surface hydroxyls with facilitate strong electronic interaction with semiconductor clusters, whereas CNFs and bacterial cellulose provide more flexible networks capable of dynamically interacting with intermediates and ensuring mass transport [92-34]. The presence of amorphous regions may possibly introduces defects and reactive sites that can promote localized charge accumulation or enhanced adsorption of pollutants prior to oxidation. In aqueous phase photocatalysis, the hydrophilic nature of cellulose, arising directly from its surface chemistry promotes water uptake, swelling, and formation of hydration shells around catalyst nanoparticles. These microenvironments enhance ROS diffusion, promote pollutant catalyst contact, and maintain a continuous supply of reactants, ultimately improving photocatalytic quantum efficiency [104-105].

On the other hand, chemical functionalization further extends cellulose mechanistic role. Oxidized cellulose introduced aldehydes and carboxylates also coordinate with metal ions, improving the robustness of in-situ precipitation, routes and yielding tightly bonded semiconductor-cellulose interface with superior charge-transfer characteristics [92]. Esterification, silylation, and graft polymerization introduce tailored hydrophobic/hydrophilic balances, enabling control over interfacial wettability, pollutant adsorption kinetics, and light-scattering properties. These chemical strategies can shift band gap energy, modulate electron density around catalytic sites, and create a synergistic interfacial electric field which influence photocatalytic rates [106-34]. Overall, the surface functional groups of cellulose are not passive stabilizers but active determinants of photocatalytic performance. By mediating both chemical and electronic interactions, cellulose transforms photocatalysts from simple nanoparticle ensembles into highly integrated, interfacial engineered hybrid systems with greater catalytic performance.

4.2.2 Hierarchical morphology

Cellulose occurs in diverse nanoscale architectures which imparts unique structural features. For example, cellulose nanocrystals (CNC's) are rigid rod like crystallite with extremely high crystallinity and specific surface area. Cellulose nanofibers (CNF) are long flexible fibrils with relatively high aspect ratios, they entangle into continuous 3-D webs. Bacterial cellulose (BC) forms ultra-fine, highly pure nanofibrillar mats that naturally assemble into porous pellicle

View Article Online
DOI: 10.1039/D5TA07511D

with nano or microscale voids [88]. For example, Habibi et al. (2020) CNFs were used as templates to coat TiO_2 via three routes, allowing the influence of CNF morphology and processing method on the final TiO_2 architecture to be evaluated. The CNF hydrogel (**Fig. 4a**) exhibited a highly entangled 3D network of long, flexible nanofibers (10–50 nm diameter), which directly entered the sol–gel process. However, excessive water triggered uncontrolled TTIP hydrolysis, causing TiO_2 nanoparticles to aggregate along the fibers and form fused TiO_2–CNF bundles (**Fig. 4b**). Freeze-drying of the CNF hydrogel collapsed the native fibrous network due to ice-crystal growth, yielding sheet-like structures in the aerogel (**Fig. 4c**). Consequently, the aerogel-TiO_2 composite (**Fig. 4d**) inherited this nanosheet morphology, with TiO_2 deposited on compacted cellulose sheets rather than on discrete fibers. In contrast, the CNF alcogel maintained the original fibrillar architecture (**Fig. 4e**), as solvent exchange with isopropanol prevented network collapse. This intact fibrous template enabled heterogeneous nucleation of TiO_2 along individual CNFs, producing well-defined TiO_2 nanowhiskers (30–50 nm thick, 250–300 nm long) that faithfully replicated the morphology of the parent CNF network (**Fig. 4f**) [107]. In another study, Cellulose substrates with identical hydroxyl content but different network structures (Regenerated cellulose scaffold (RC1W), RC1E, RC1T) were prepared by regeneration in water, ethanol, and tert-butanol baths. Despite their varying pore sizes (276, 599, and 411 nm), all corresponding AZO-loaded composites (AZOC1W/E/T) showed the same flake-like morphology, indicating that cellulose spatial hindrance does not control AZO shape when –OH density is constant. To evaluate the role of hydroxyl content, substrates RC1, RC2, and RC3 were produced with increasing cellulose loadings, giving progressively higher –OH densities. This directly altered AZO morphology: RC1 yielded flake-like AZO, RC2 generated fragmented flower-like structures, and RC3 produced well-defined flower-like architectures. Increasing –OH density enhanced Zn^{2+} coordination and nucleation site availability, driving the assembly of AZO nanosheets into hierarchical flowers. Al doping did not affect morphology, confirming that cellulose hydroxyl density is the dominant regulator of AZO structure [108]. Yan et al. (2023) explained SEM imaging and fractal analysis were used to track morphology evolution during CNF etherification. All etherified samples retained their fibrillar structure, but their surfaces became progressively rougher with increasing DS. This trend was quantitatively confirmed by the box-counting fractal dimension (D), which increased from 1.37 to 1.47, indicating increasingly complex surface contours ($R^2 > 0.98$ for all fits). To eliminate differences in diameter and surface roughness introduced by etherification, the samples were ground proportionally to their D values. After grinding, all CNF and ECNF samples exhibited comparable morphologies, with similar fractal dimensions (1.50–1.53) and high fitting accuracy ($R^2 > 0.98$). ImageJ analysis further verified uniform size distributions: all samples had mean diameters of 23 nm and lengths of ~1.6–1.8 μm. Overall, CNFs with varying electronegative oxygen contents but nearly identical dimensions and surface morphologies were successfully obtained [109]. Shi et al. (2021) described interfacial synthesis enabled the uniform growth of X-COFs on C-CNC surfaces, yielding CNC@Br-COF, CNC@OH-COF, and CNC@OMe-COF nanocomposites (**Fig. 4ii a-b).** Their PXRD patterns retained the characteristic reflections of both COFs and C-CNC, confirming successful hybrid formation (**Fig. 4ii b**). SEM images showed well-defined core–shell structures, with COF shells markedly thicker (Br-COF: 72–107 nm; OH-COF: 64–78 nm; OMe-COF: 125–165 nm) than pristine C-CNC (30 nm) (**Fig. 4 ii c–e**) [110].

View Article Online
DOI: 10.1039/D5TA07511D

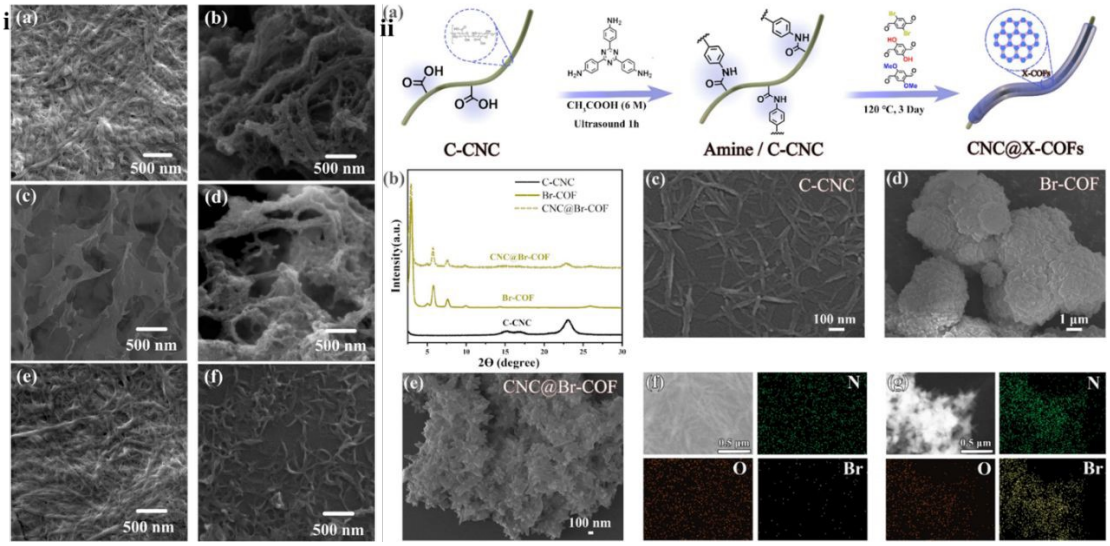

Fig. 4 (i) SEM images of (a) CNF hydrogel, (b) hydrogel-TiO_2, (c) CNF aerogel, (d) Aerogel- TiO_2, (e) CNFs alcogel, (f) Alcogel- TiO_2, Reprinted with permission from ref. [107], Elsevier (2020). (ii) (a) Schematic representation of preparation of CNC@X-COFs, (b) XRD spectra, (c-e) SEM images, and (f-g) EDX spectra of C-CNC and CNC@Br-COFs. Reprinted with permission from ref.[110], Elsevier 2025.

4.2.3 Chirality

Cellulose is intrinsically chiral due to the asymmetric carbon centers in each β-D-glucopyranose unit, which give rise to the helical chain conformations and chiral nematic phases in CNC and CNF-based architectures. The hierarchical chirality influence photocatalysis through acting of chiral surfaces as enantioselective templates during semiconductor nucleation. Wang et al. (2020) helical arrangement of -OH groups can bias crystal orientation of photocatalysts and promotes controlled facet exposure and enhance charge separation. The hierarchical chirality in biopolymeric scaffolds can significantly influence photocatalytic performance by acting as enantioselective templates during semiconductor nucleation. The helical arrangement of surface -OH groups create an asymmetric chemical environment that biases crystal growth, guiding preferential facet exposure in emerging photocatalyst domains. Such chiral templating can modulate charge distribution and electron-hole separation pathways, thereby enhancing photocatalytic efficiency [111]. Few researchers emphasized CNC-based structures as photon architectures. The periodic helical order can generate the photonic band gaps, slow photon transport, and enables local magnetic fields and thereby strengthens visible light harvesting in composite photocatalysts. The hybrid material was constructed by orienting anisotropic AgNWs within an optically tunable cholesteric CNC matrix, giving rise to a well-defined interplay between the CNC photonic bandgap and the localized surface plasmon resonances of the nanowires. The resultant photonic–plasmonic coupling mediated by the interaction of PBG-supported electromagnetic modes with AgNW plasmon modes enables precise control over electromagnetic energy transfer and yields selective modulation of plasmonic features within a confined spectral region. Importantly, this coupling persists under dynamic excitation, as evidenced by pronounced transient optical responses in pump–probe measurements [112]. Overall, cellulose chirality

View Article Online
DOI: 10.1039/D5TA07511D

acted as an optical and interfacial modulator guiding semiconductor growth, tuning light-matter interactions and enhancing photocatalytic pathways.

4.2.4 Surface area

The inherently higher surface area and tunable porosity of cellulose-based scaffolds significantly boosted the photocatalytic performance the facilitating catalyst dispersion and mass transport. Shi et al. (2021) explained the N_2 adsorption–desorption isotherms of the Ag–ZnO/C nanocomposites exhibited a type IV profile, confirming their mesoporous nature. The increasing grinding time significantly influenced the development of the cellulose fiber network, leading to reduced pore diameters (90.43, 54.48, and 43.76 nm for Ag–ZnO/C10, C20, and C30) and increased specific surface areas (25.06, 31.49, and 40.64 $m^2 g^{-1}$, respectively). These trends are consistent with SEM observations, demonstrating that Ag–ZnO/C30 possesses the most developed porous structure, providing a larger effective surface for dye adsorption and photocatalytic degradation [113].

The fibrillar cellulose networks prevent nanoparticle aggregation and maximize the number of exposed catalytic sites, ensures effective interaction with the organic contaminants. For example, Yan et al. (2023) emphasized that the specific surface area of CNF and ethylated CNF (ECNF) samples increases with the degree of substitution (DS), from 28.03 $m^2 g^{-1}$ for CNF to 37.12 $m^2 g^{-1}$ for ECNF-4, while SEM analysis confirms their morphology and size remain similar. The higher content of surface ethoxy groups promotes 3D network formation with increased pore density due to electrostatic repulsion. Nitrogen adsorption–desorption isotherms (type III with H3 hysteresis) and FHH fractal analysis show that surface roughness (D1) increases with DS, whereas the overall structural complexity (D2) remains comparable [109]. On the other hand, interconnected porous architecture provides a large interfacial contact area, promoting rapid adsorption, accelerated reactant diffusion, and oxygen penetration into catalyst unit. Liu et al. (2025) explained the surface, cross-sectional, and longitudinal morphologies of the CTC aerogels reveal a well-developed three-dimensional porous framework with a rough surface. This structure results from the lightweight network formed during the freezing process, with the aerogel density measuring 12.92 mg cm^{-3}. Such a highly porous architecture significantly enhances the surface activity of the composite. The SEM observations further show that TiO_2 nanoparticles are densely and uniformly anchored onto the aerogel skeleton (scale 5 μm), confirming effective integration within the porous network [114]. In short, the porous nano-cellulose scaffolds provide a huge contact area for both catalyst and pollutants, increasing adsorption sites and ensuring the reactants and oxygen, which diffuses quickly into photocatalytic network.

5. Cellulose-supported photocatalysts

Cellulose supported photocatalysts can be broadly classified into two general categories based on their material configuration and functional applications: (a) cellulose-based composite photocatalyst, and (b) cellulose-based functional architectures photocatalysts. The first category, composite photocatalysts involved direct integration of photocatalytic materials into cellulose matrix to form homogenous composites to enhance dispersion, surface area, and charge separation. Structured systems, including hydrogels, aerogels, membranes, and 3D-printed forms, offer defined architecture, improved reusability and efficient mass transfer, making them suitable for continuous and

View Article Online
DOI: 10.1039/D5TA07511D

multifunctional processes. The major difference between the composite photocatalyst, and cellulose-based functional architectures photocatalysts are indicated in **Fig. 5**.

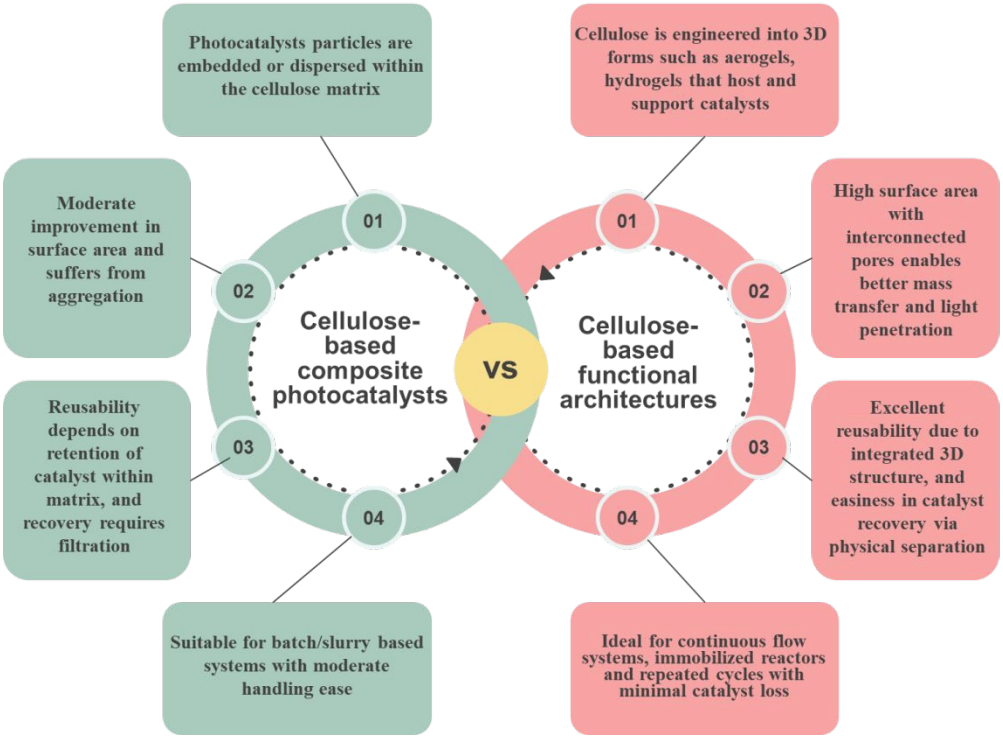

Fig. 5 Comparison between cellulose based photocatalysts such as composite and functional architectures

5.1 Cellulose-based composite photocatalysts

Cellulose-based composite photocatalysts refer to hybrid materials where photocatalytic components such as metal oxides (TiO_2 and ZnO), metal sulfides, carbon nitride, or MOFs are embedded or anchored onto a cellulose matrix. These composites leverage the high surface area, tunable porosity, and abundant functional groups of cellulose to enhance photocatalyst dispersion, light absorption, and pollutant adsorption. They are broadly classified into (i) Metal-oxide Cellulose-composite catalyst, (ii) Metal sulfide cellulose catalyst, (iii) Carbon nitride supported cellulose catalyst, and (iv) MOFs supported cellulose catalyst.

5.1.1 Metal oxides based

Metal oxides (ZnO, TiO_2, SnO_2, and ZrO_2) remain among the most widely employed photocatalysts due to their environmental compatibility, chemical robustness, and cost-effectiveness [115,116]. However, their intrinsic drawbacks such as wider band gaps, fast charge recombination, and morphology-dependent activity often limits visible-light performance [117,118]. Integrating these oxides with cellulose-based biopolymers introduces structural and electronic advantages including improved dispersion, defect engineering, and enhanced adsorption, making cellulose-metal oxide hybrids a promising class of photocatalysts.

View Article Online
DOI: 10.1039/D5TA07511D

TiO_2 and ZnO are the most extensively investigated owing to their stability, abundance, and low toxicity [20,119]. Yet, their wide band gaps (3.2 and 3.37 eV, respectively) inherently restrict solar utilization, highlighting the importance of composite design strategies such as doping, heterojunction formation and morphology modulation [120,121]. Nano-chitosan (NCS), CMC, and TiO_2 was synthesized using a sol-gel strategy, where CMC incorporation induced a visible light absorption a redshift in absorption from 291 nm to 430 nm. The CMC inclusion markedly transformed the TiO_2 morphology, shifting from irregular, ruptured surfaces in NCS/TiO_2 to a more defined, needle-like and highly porous structure. This modification indicates improved TiO_2 dispersion, enhanced lattice defects, and increased surface area, all contributing to more abundant active sites. This is correlated with a 95% degradation of crystal violet, underscoring that cellulose modifications can transcend mere dispersion and actively tune TiO_2 electronic behavior. TGA and DSC analyses revealed high thermal stability, with 44.2% decomposition at 600 °C and a glass transition temperature around 250 °C. These results collectively suggest that the extent to which cellulose influences TiO_2 performance is highly dependent on synthesis strategy and interfacial bonding, not solely on the type of biopolymer employed [122].

ZnO-based systems exhibit similar cellulose-dependent effects. Janpetch et al. (2016) fabricated ZnO/bacterial cellulose (BC) via solution plasma processing (SSP), where the BC nanofiber network served as a 3D scaffold guiding Zn^{2+} diffusion and nucleation. The strong dependence of ZnO morphology such as plate-like, rod-like (zinc nitrate) or multilayered sheets (zinc acetate) on the precursor and synthesis routes highlights a key advantage of cellulose: its ability to modulate nanostructure evolution by ion anchoring and templating. SEM analysis showed that bacterial cellulose exhibited a web-like nanofiber structure, making it ideal for supporting ZnO formation (**Fig. 6 i)**. The ZnO/BC composites synthesized through SPP exhibited strong antibacterial activity against *E. coli* and *S. aureus*, primarily due to the Zn^{2+} ion release mechanism [123]. Li et al. (2020) further demonstrated that the micro/nano-cellulose fibrils (MNCFs) significantly influence ZnO growth kinetics. The porous Al-doped ZnO/cellulose composites via chemical deposition, utilizing micro/nano cellulose fibers (MNCFs) as the substrate. The characterization studies reported a reduced fibers diameter from 100 to 31 nm markedly decreased ZnO crystallite size from 40.6 to 14.2 nm, increased surface area of 27.5 $m^2\ g^{-1}$, and enhanced porosity of 94.6%. Al-doping combined with the cellulose nanofibrils scaffold lowered the band gap from 3.06 to 2.92 eV and yielded 89% degradation of methyl orange under visible light. Notably, this system showcased a synergistic interplay between cellulose microstructure and dopant chemistry, unlike undoped systems where cellulose primarily influence morphology but not electronic structure. The thermal stability increased due to the presence of metal oxides, and UV-Vis analysis revealed a red shift in absorption with Al-doping and fiber interaction. [124].

Cellulose-based-γ-Fe_2O_3-ZrO_2 nanocomposites prepared via simple sol-gel methods demonstrated an even more pronounced electric effects. The ZrO_2 incorporation reduced the γ-Fe_2O_3 band gap from 4.90 eV to 2.28 eV, enabling strong-light absorption, while cellulose enhanced dispersion and surface roughness (**Fig. 6ii)**. The nanocellulose did not considerably alter the band gap, it contributed to better dispersion and morphology, supporting uniform distribution of the metal oxides. Microscopy revealed spherical to oval nanostructures with high surface roughness and porosity, while BET analysis indicated an increase in surface area from 412 $m^2\ g^{-1}$ for pure cellulose to 530 $m^2\ g^{-1}$ for the composite. The cellulose/γ–Fe_2O_3–ZrO_2 nanocomposite exhibited a crystallite size of 41.46 nm.

View Article Online
DOI: 10.1039/D5TA07511D

Nanocellulose serves as a high-surface-area support in γ–Fe_2O_3–ZrO_2 heterojunction photocatalysts, enhancing electron–hole separation and pollutant adsorption, which synergistically boosts visible-light-driven Congo red degradation up to 98.5 %. Nanocellulose, with its high surface area, acts as an effective support for γ–Fe_2O_3–ZrO_2 heterojunction photocatalysts, synergistically enhancing electron–hole separation and pollutant adsorption. Compared to ZnO and TiO_2 systems, Fe_2O_3–ZrO_2 heterojunction clearly benefitted more from cellulose-induced charge handling enhancements than from mere structural templating [125].

The green synthesis of cellulose/ZrO_2 nanocomposites was prepared using a co-precipitation method via incorporation of tetragonal ZrO_2 into the cellulose matrix without altering the crystal phase of cellulose. The FESEM and TEM analyses revealed uniform dispersion of ZrO_2 nanoparticles within the biopolymer matrix, with no aggregation. The optical studies indicated a bathochromic shift in the UV–Vis absorption spectrum of the nanocomposite (from 258 nm to 288 nm) and a corresponding decrease in band gap from 4.81 eV (ZrO_2) to 4.31 eV (cellulose/ZrO_2), attributed to enhanced crystallinity and quantum confinement effects. The cellulose/ZrO_2 nanocomposite exhibited enhanced photocatalytic degradation of methyl orange, achieving 76 % within 50 min compared to 66 % in pure ZrO_2 nanoparticles over 80 min [126]. This comparatively lower performance highlights that cellulose-metal oxide synergy varies strongly with oxide electronic structure, wide band gap materials like ZrO_2 requires additional interface engineering beyond cellulose incorporation to achieve meaningful photocatalytic gains.

Across, the metal oxide based photocatalytic systems, a clear trend emerges (i) cellulose enhances dispersion, porosity, and adsorption in all systems, (ii) electronic tuning occurs only when cellulose participates in chemical coordination or when combined with dopants or heterojunctions, and (iii) mixed oxides shows the strongest synergistic enhancement due to complementary band structures and improved interfacial charge transfer. Thus, performance window (76 to 98% degradation under visible light) is dictated not by the cellulose type alone but by the interplay between oxide electronic structure cellulose-oxide interfacial chemistry, and morphological engineering. These insights highlight cellulose-metal oxide composites as modular platforms where targeted chemical and structural design can unlock significantly enhanced visible-light photocatalytic activity for diverse applications.

5.1.2 Metal sulfides

The metal sulphide-based semiconductor has emerged as a promising photocatalyst due to its narrow band gaps, strong visible light absorption, abundant active sites, and favorable redox potentials [127]. Compared to conventional metal oxides, metal sulfides like CdS, CuS, ZnS, MoS_2, and Bi_2S_3 exhibit superior hydrogen generation capabilities and enhanced photoactivity towards wastewater remediation. Their electronic structures featuring d^{10} cations and S 3p orbitals contribute to efficient charge separation and light harvesting [128]. Moreover, the unique nanostructures and surface-active sites, particularly at the S-edge and defect zones, further boost their catalytic activity. Integrating these metal sulfides with cellulose enhances dispersion, stability, and reusability. The synergistic combination holds great potential for developing efficient and eco-friendly photocatalytic systems.

Zhang et al. engineered a uniformly anchored CuS–cellulose composite using polydopamine (PDA) as a robust bio-inspired adhesive. The PDA enabled strong Cu^{2+} chelation through abundant catechol groups, promoting

View Article Online
DOI: 10.1039/D5TA07511D

homogeneous CuS nucleation on cellulose fibers and effectively suppressing photocorrosion. The pre-doping strategy ensured maximal metal–ligand coordination, while in situ polymerization and sulfide treatment yielded a flexible CuS-coated cellulose paper through conventional papermaking. The SEM/EDS analysis confirmed that PDA transformed the inherently agglomerated CuS morphology into a densely distributed nanostructure, while BET measurements revealed a markedly increased surface area (48 $m^2\ g^{-1}$). The improved dispersion and the PDA-mediated charge-separation pathway enhanced photocatalytic activity, with the composite showing up to 5.8-fold higher degradation efficiency than CuS on untreated fibers [129]. Wang et al. constructed a multifunctional photocatalytic paper by coupling reduced graphene oxide (rGO) and CuS with dialdehyde cellulose fibers (DACF) through hyperbranched polyamide-amine (HPAMAM), which served as both a covalent linker and a nanoreactor for controlled CuS growth. The Schiff-base bonding between DACF and HPAMAM/rGO facilitated stable immobilization, while the branched polymer confined CuS nucleation into uniformly dispersed nanoclusters. The structural analyses showed retention of the cellulose I framework with increased amorphous character, weakened rGO stacking, and well-defined CuS diffraction peaks. SEM revealed that HPAMAM was essential for avoiding rGO/CuS agglomeration and achieving intimate nanoscale contact. The hierarchical structure improved charge separation and mechanical stability, leading to a 2.7-fold increase in the RhB degradation rate and excellent reusability (>90 % after ten cycles) [130].

Xu et al. (2022) synthesized rime-like carbon paper@Bi_2S_3 hybrids via a one-step solvothermal process (**Fig. 6 iii**), where the precursor concentration controlled the density and morphology of Bi_2S_3 nanorods. The cellulose-derived carbon fibers (8 μm), retaining surface hydroxyl residues, intrinsic chirality, and a naturally wrinkled porous texture, provided abundant nucleation sites that directed Bi_2S_3 crystallization. The low precursor levels (CB-1) yielded sparse deposition, whereas CB-2 and CB-3 supported dense, flower-like Bi_2S_3 clusters formed by elongated nanorods through accelerated axial growth and Ostwald ripening. The XRD, Raman, and XPS confirmed orthorhombic Bi_2S_3, preserved carbon structure, and strong Bi–S–C interfacial contact. Importantly, the hierarchical carbon scaffold enhanced Bi_2S_3 anchoring, improved interfacial polarization, and strengthened impedance matching attributes directly tied to the cellulose-origin hydroxyl functionality, chiral microstructure, and high porosity. These synergistic interfaces enabled multiple attenuation pathways, resulting in significantly improved microwave absorption performance [131].

Jiang et al. (2020) synthesized berry-like CdS/MoS_2 structures using bacterial cellulose (BC) as a bio-template, where the intrinsic hydroxyl-rich, chiral nanofibrillar network of BC played a decisive role in directing CdS nucleation. The abundant surface –OH groups and the naturally twisted, porous architecture enabled uniform Cd^{2+} anchoring and confined CdS crystallization into nanoscale domains, effectively suppressing agglomeration and increasing active surface area. Subsequent integration of ultrathin MoS_2 nanosheets produced tightly interfaced CdS–MoS_2 heterojunctions that facilitated rapid charge transfer. The optimized composite exhibited a higher surface area (21.8 $m^2\ g^{-1}$) and enlarged mesopores (6.95 nm), attributes arising from the BC-derived scaffold that enhanced light harvesting and reaction-site accessibility. High-resolution analyses confirmed intimate MoS_2–CdS contact and homogeneous elemental distribution. Benefiting from both the heterojunction and the cellulose-origin structural features (hydroxyl coordination, chiral fiber templating, and hierarchical porosity), the composite achieved an

View Article Online
DOI: 10.1039/D5TA07511D

impressive H_2 evolution rate of 63.59 ± 1.20 mmol g^{-1} h^{-1} with strong recyclability driven by stabilized charge separation and improved catalyst dispersion [132]. Tavker et al. (2020) synthesized MoS_2 nano-petals anchored onto cellulose through an in-situ hydrothermal method, where the hydroxyl-rich, chiral, and porous microfibrillar structure of cellulose acted as a sustainable scaffold that directed MoS_2 nucleation and orientation. The abundant –OH groups on cellulose promoted strong interfacial bonding with Mo precursors, enabling uniform MoS_2 growth and preventing nanosheet restacking, while the intrinsic helical fibril arrangement and porous network provided spatial confinement for the formation of petal-like architectures. The XRD, XPS, HRTEM, and SAED confirmed well-defined MoS_2 nano-petals with robust MoS_2 cellulose interactions. The resulting composite displayed a high surface area (60 m^2 g^{-1}) and reduced pore size (2 nm), enhancing dye adsorption and light utilization. This cellulose-guided architecture facilitated efficient charge transfer, suppressed electron–hole recombination, and improved carrier mobility, while the hierarchical nano-petals increased light scattering and active-site density. Consequently, the MoS_2@cellulose system delivered rapid photocatalytic degradation of RhB and industrial dyes within 25 min, with performance directly linked to the synergistic effects of cellulose's hydroxyl functionality, chiral templating, and porous structure [133].

Liao et al. (2023) constructed a 3D Z-scheme In_2S_3–C/Fe_3C photocatalyst in which the conductive carbon framework, derived from cellulose, played a central role in mediating charge flow and stabilizing the active components. The cellulose precursor rich in OH groups, chiral microfibril ordering, and hierarchical porosity enabled uniform impregnation and carbonization, generating a high-surface-area carbon scaffold with abundant anchoring sites for In_2S_3 nucleation. The band alignment and photo-deposition results showed that In_2S_3 and Fe_3C serve as the reduction and oxidation centers, respectively, while DFT calculations revealed that Fe_3C lowers the barrier for *CO → *COH coupling and weakens In–S bonds, enhancing acetate selectivity. Compared with pristine In_2S_3 (λ < 545 nm), the composite exhibited broad-spectrum absorption due to the metallic carbon–Fe_3C matrix. The Z-scheme electron-transfer pathway between Fe_3C and In_2S_3 facilitated by the cellulose-derived conductive network suppressed photocorrosion, promoted charge separation, and increased accessible active sites. These synergistic effects resulted in efficient and selective acetate production (11.33 μmol h^{-1} g^{-1}, 89 % selectivity) with excellent structural and photocatalytic stability, directly linked to the templating, porosity, and electron-transport properties imparted by the cellulose backbone [134].

Liang et al. (2023) synthesized a Bi_2O_3/$Zn_3In_2S_6$ (BO/ZIS) S-type heterojunction via a hydrothermal route and immobilized it on sugarcane-bagasse-derived cellulose (SBC). The SEM imaging confirmed that the flower-like $Zn_3In_2S_6$ and flaky Bi_2O_3 were assembled into compact nanospheres that were uniformly anchored onto the cellulose fibers. The abundant -OH groups, hierarchical porosity, and microfibrillar network of SBC promoted strong interfacial bonding, homogeneous nanoparticle dispersion, and efficient deposition of the BO/ZIS units. The BET analysis revealed that supporting the catalyst on SBC significantly increased the specific surface area (91.79 m^2 g^{-1}) while preserving mesoporosity, thereby improving pollutant adsorption and reactant–catalyst contact. The photophysical characterization (PL, photocurrent response, EIS) demonstrated that the cellulose scaffold further enhanced charge separation within the S-type heterojunction by providing a conductive, low-resistance interface that facilitated electron transport and reduced recombination. The improved dispersion and stabilized interfacial architecture contributed to

View Article Online
DOI: 10.1039/D5TA07511D

faster mass transfer, higher density of accessible active sites, and better utilization of photogenerated carriers. Catalytically, SBC/BO/ZIS-30 achieved 97 % degradation of 2,4-DCP at neutral pH (0.3 g L^{-1}), outperforming the unsupported BO/ZIS composite [135].

Across these reports, the response of different metal sulfides to cellulose support varies according to their crystal structures, intrinsic stability, and surface chemistry. The CuS, which readily undergoes photocorrosion, shows the strongest improvement when cellulose introduces chelating groups (PDA–catechol) that stabilize Cu^{2+} and promote uniform nucleation. Differently, CdS benefits primarily from photocorrosion suppression and heterojunction formation, where the BC scaffold regulates particle size and enables intimate CdS–MoS_2 contact. The layered MoS_2 interacts differently, as cellulose templating directs nanosheet or petal formation, increasing edge-site density and accelerating charge transport. In contrast, Bi_2S_3 an anisotropic 1D sulfide exhibits morphology-dependent growth on carbonized cellulose due to improved axial orientation and interfacial polarization. For In_2S_3, cellulose-derived carbon frameworks provide conductivity and Z-scheme electron mediation, mitigating self-corrosion. The $Zn_3In_2S_6$ shows enhanced photocatalytic response when cellulose stabilizes S-type heterojunctions and maintains mesoporosity. These differences demonstrate that cellulose does not act uniformly across all metal sulfides; rather, its hydroxyl-rich, porous, and tunable surface interacts uniquely with each sulfide's growth mechanism, band structure, and stability, generating distinct performance outcomes.

5.1.3 Cellulose-based Carbon Nitride Photocatalysts

Cellulose-based carbon nitride photocatalysts represent a rapidly emerging class of metal-free hybrid materials engineered to overcome the intrinsic drawbacks of pristine g-C_3N_4 (GCN), namely its low surface area, limited active sites, and inefficient charge separation. Across recent studies, cellulose has consistently demonstrated a dual functional role: (i) a structural scaffold enabling nanoscale dispersion, hierarchical porosity, and chemical stability; and (ii) an electronic/proton mediator, introducing interfacial interactions that facilitate charge transport, suppress recombination, and enhance redox reaction kinetics. A critical comparison of representative systems highlights how cellulose chemistry, morphology, and surface functionality directly dictate photocatalytic outcomes.

In the GCN/ hydroxyethyl cellulose (HEC) system reported by Zhang et al., HEC acts as a solid proton donor, creating hydrogen-bond networks that promote proton-coupled electron transfer (PCET). Although HEC reduces the BET surface area (71.70 to 51.79 m^2 g^{-1}). SEM and TEM confirm that GCN/HECc retains nanosheet morphology while HEC uniformly modifies GCN, slightly expanding interplanar spacing, which facilitates enhanced charge transfer and H_2O_2 generation. The characteristic peaks at 27.64° and 13.19° indicated the presence of the conjugated aromatic stacking and tri-s-triazine units, with a crystallite size of 9.3 nm (**Fig. 6iv a**). TGA/DTG analysis (**Fig. 6 iv b**) shows that HEC undergoes major decomposition (73%) at 220–380 °C, while g-C_3N_4 remains stable, and CN/HEC composites exhibit only slight weight loss (0–5.1%) that increases with HEC content. The SEM (**Fig. 6 ivc-d)**and XRD evidence show expanded interlayer spacing and improved nanosheet integrity, enabling more efficient charge transport. The ptical absorption studies revealed that the band gap (2.93 eV) remained unchanged upon HEC modification, indicating no significant alteration in electronic structure. The resulting 52.6 % enhancement in H_2O_2

View Article Online
DOI: 10.1039/D5TA07511D

production and a twofold increase in photocurrent explicitly validate cellulose's role as an electronic modulator, independent of surface-area-driven pathways [136].

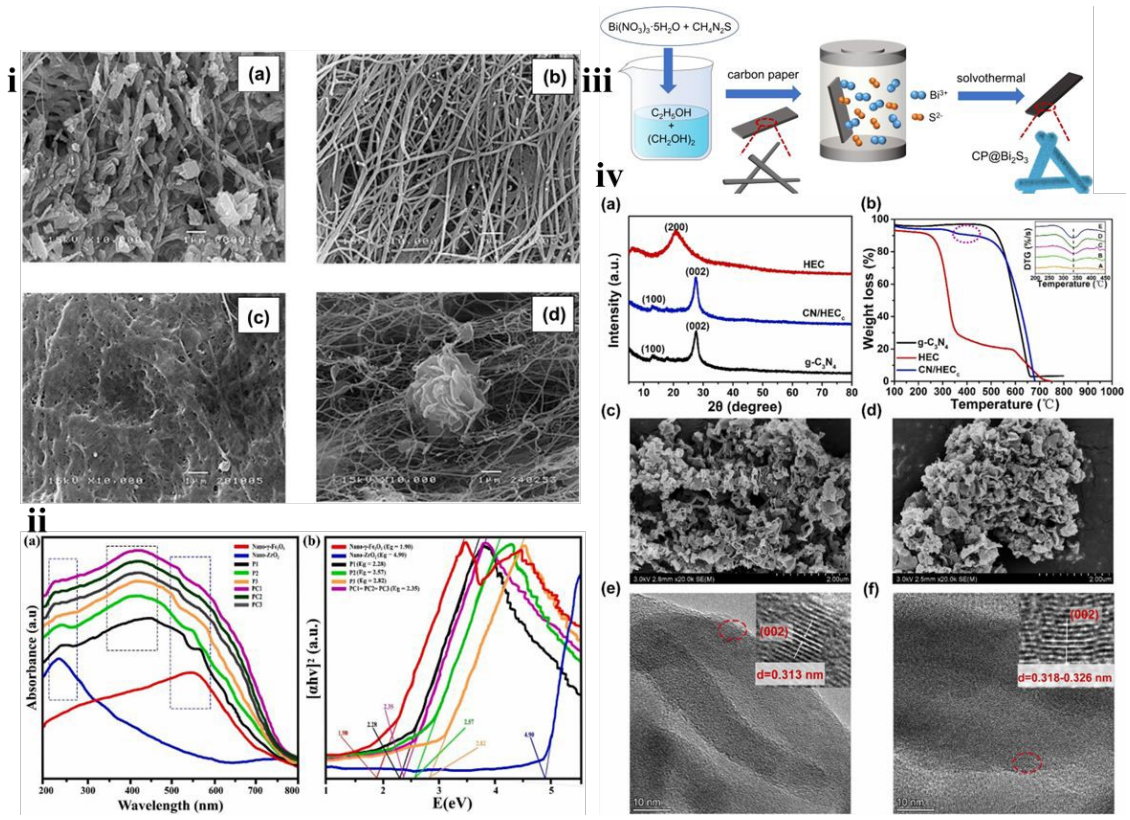

Fig. 6 (i a-d) SEM images of ZnO/BC composites. Reprinted with permission from ref.[123], Elsevier (2016). **(**ii) UV-Vis DRS spectra and band gap energy of different catalysts. Reprinted with permission from ref. [125], Elsevier (2022). (iii) Preparation of rime-like carbon paper@Bi_2S_3 hybrids via a one-step solvothermal process. Reprinted with permission from ref. [131], Elsevier (2022). (iii) (iv) (a) XRD spectra, (b) TGA curve of GCN-based photocatalyst, SEM images of (c) GCN, (d) GCN/HEC's, TEM images of (e) GCN, (f) GCN/HEC's. Reprinted with permission from ref. [136], Elsevier (2022).

Xu et al. (2023) synthesized a $BiYO_3$/GCN/CNF composite via electrostatic self-assembly, achieving notable improvements in visible-light photocatalytic activity. The formation of a heterojunction between $BiYO_3$ and GCN facilitates efficient charge separation and transfer, mitigating rapid electron-hole recombination commonly observed in pure GCN. The CNFs act as a high-surface-area, porous scaffold, preventing nanoparticle agglomeration and enhancing dispersibility, which increases accessibility to active sites and improves pollutant adsorption. The SEM and TEM analyses revealed $BiYO_3$ nanosheet petals and GCN nanoflakes forming a tight nanosheet structure, enabling intimate interfacial contact for rapid photogenerated carrier migration. The BET and BJH measurements showed that the inclusion of CNFs increased surface area from 47 to 66 $m^2 g^{-1}$ and pore volume to 0.35 $cm^3 g^{-1}$, directly correlating with enhanced adsorption of tetracycline (TC) molecules and faster photocatalytic reactions. The optical studies demonstrated narrowed band gaps for GCN (2.54 eV) and $BiYO_3$ (2.61 eV), with well-aligned conduction and valence

View Article Online
DOI: 10.1039/D5TA07511D

band positions, promoting effective electron transfer within the heterojunction. Consequently, the $BiYO_3$/GCN/CNF composite achieved 97% TC degradation. Critically, the CNFs not only serve as a structural support but also synergistically enhance photocatalytic performance by combining adsorption with light-driven charge separation, while facilitating easy catalyst recovery and recyclability [137].

Zhao et al. (2021) constructed a ternary Z-scheme photocatalyst composed of carbon-doped GCN and WO_3, which was synthesized through a multi-step process involving hydrothermal impregnation with nanocrystals, high-temperature calcination, and electrostatic self-assembly with WO_3 nanocuboids. The prepared composites benefited from a porous structure, a high specific surface area of 57 m^2 g^{-1}, carbon substitution, and the construction of a Z-scheme heterojunction. These features collectively contributed to a narrowed band gap, enhanced visible light absorption, improved charge carrier separation, and redox capabilities [138]. Kapok fiber (t-KF), a cellulose-based microtubular structure, has been employed as a solid electron donor to enhance the photocatalytic activity of carbon-doped GCN (CCN) via a ligand-to-metal charge transfer (LMCT) mechanism. The cellulose scaffold provides a high-surface-area, biocompatible support that improves CCN dispersibility, structural integrity, and accessibility of active sites. Using succinic acid (SA) as a cross-linker, CCN was successfully grafted onto t-KF through a hydrothermal process, forming a hybrid complex with uniform CCN distribution on the fiber surface and inner tubular structure. FESEM and TEM analyses confirmed the well-dispersed, thicker CCN layers in CCN-SA/t-KF, while FTIR spectra indicated effective immobilization of CCN without altering its characteristic structure. BET/BJH analysis revealed that SA incorporation enhanced surface area and mesoporosity, further facilitating reactant adsorption and charge transfer. The LMCT interactions between the hydroxyl groups of cellulose and amine groups on CCN synergistically improved interfacial electron transfer, resulting in 1.8-fold higher H_2O_2 generation under visible light compared to pristine GCN. This study underscores the critical role of cellulose as a structural and functional support, enabling better dispersion, enhanced charge separation, and improved photocatalytic performance [139].

Cellulose is not a passive support but an active photocatalytic co-participant whose chemical identity, degree of substitution, and multiscale morphology determine the governing mechanism such as PCET (HEC), adsorption–charge synergy (CNFs), or LMCT (t-KF). Key comparative insights include: (i) Charge Transport: HEC and t-KF outperform CNFs in electronic modulation due to stronger proton- or ligand-mediated coupling with g-C_3N_4. (ii) Surface Area and Adsorption: CNFs deliver the most substantial textural enhancements, resulting in superior pollutant preconcentration and more complete degradation pathways. (iii) Interfacial Integration: Kapok fibers enable the thickest and most uniform CN deposition, enhancing long-term recyclability and mechanical durability. Collectively, these studies underscore that cellulose selection is a decisive variable not a secondary material component in dictating g-C_3N_4 photocatalyst architecture, interfacial electronic coupling, and reaction kinetics. Strategic control over cellulose chemistry and multiscale structure enables tailored hybrid systems with enhanced redox potential, enriched active sites, and superior charge–mass transport characteristics. The high-level synergy between cellulose frameworks and GCN thus represents a powerful blueprint for next-generation sustainable photocatalysts, with direct implications for environmental remediation, energy conversion, and green chemical synthesis.

5.1.4 Cellulose-supported MOFs

View Article Online
DOI: 10.1039/D5TA07511D

The integration of metal–organic frameworks (MOFs) with cellulose has emerged as a powerful strategy to overcome longstanding challenges associated with MOF fragility, particle agglomeration, and limited processability. MOFs offer exceptional porosity, tunable chemistry, and strong visible-light responsiveness; however, their standalone performance is often compromised by poor mechanical robustness and inefficient charge utilization. Cellulose whether as carboxymethyl cellulose (CMC), bacterial cellulose (BC), carbonized fibers (CCF), or cotton fabric functions as more than a passive support. Its hydroxyl-rich, hydrophilic, and hierarchically structured architecture enables precise control over MOF nucleation, dispersion, charge transport, and macroscopic formability, making cellulose-supported MOFs a compelling platform for photocatalysis. [140,141] [142].

Khodayari et al. (2024) reported the successful fabrication of CMC/MIL-101(Fe)/CuO biocomposites for photocatalytic applications. The MIL-101(Fe) retains its characteristic octahedral morphology upon integration with CMC and CuO, indicating high structural stability. FTIR, XRD, SEM, and DRS analyses confirmed the successful synthesis of the CMC/MIL/CuO biocomposite, with CMC providing abundant OH^- groups that enhance binding, dispersion, and stability of MIL-101(Fe) and CuO. The amorphous CMC matrix acts as a scaffold, preventing aggregation and preserving the crystalline structure of MIL-101(Fe), while promoting synergistic interactions that lower the band gap to 2.1 eV. Here, CMC not only enhances the dispersion of MIL-101(Fe) and CuO but also promotes interfacial charge transfer, enabling >90% pollutant removal under visible light. The synergistic interaction between the hydroxyl groups of CMC and Fe-O clusters of MIL-101(Fe) demonstrates cellulose's ability to modulate electronic structure through chemical coupling [143]. Zheng et al. (2024) developed a photocatalyst by integrating MOF-derived carbon skeletons (MDCS)-encapsulated Ni nanoparticles and BiOBr onto carbonized cellulose fibers (CCF) using polydopamine as a template and anchoring agent. In contrast, CCF/PDA-C/Ni@MDCS/BiOBr composites employ cellulose fibers as a thermally resilient scaffold that enables targeted growth of Ni-MOFs, which convert into MOF-derived carbon skeletons (MDCS). The resulting hierarchical structure (surface area >1100 $m^2\ g^{-1}$) significantly enhances charge mobility and reactant diffusion. Here, cellulose indirectly governs photocatalytic performance by dictating the spatial organization of Ni nanoparticles and BiOBr nanosheets, yielding narrowed band gaps (1.49 eV) and high stability over 10 cycles. The study exemplifies cellulose's ability to accommodate multi-component hybrid architectures without compromising structural coherence. This highlights the synergistic role of CCF in improving photocatalytic efficiency, structural robustness, and reactant diffusion [144].

Cellulose nanocrystals (CNCs), owing to their inherent helical rod-like morphology, impart topological chirality when integrated into ZIF-8, forming CNCs@ZIF-8 3D networks that link individual ZIF-8 crystals into ordered architectures. This chiral structuring enhances spatial confinement of micro- and nanoscale reaction sites, improves light penetration, and facilitates mass transport, distinguishing it from pristine ZIF-8, which lacks optical activity and forms isolated truncated rhombic dodecahedra. Optical characterization reveals that CNCs@ZIF-8 exhibits positive optical rotation (α = +12.224 to +21.290) and circular dichroism signals, with higher chirality correlating positively with photocatalytic CO_2 reduction (up to 301.16 μmol g^{-1} for α = +21.290, 9.43 times higher than ZIF-8), highlighting the functional role of chirality in enhancing light–matter interactions and charge separation. The interfacial formation of Zn–O–S and Zn–N–S bonds promote electron delocalization and reduces electron-hole recombination, as confirmed

View Article Online
DOI: 10.1039/D5TA07511D

by photoluminescence studies, while negative surface charges from CNCs stabilize the 3D network via electrostatic assembly. Despite a decrease in specific surface area and mesoporosity at higher CNC content (from 1084.27 to 226.25 $m^2\ g^{-1}$), the chiral network maintains recyclability and structural robustness over multiple cycles, underscoring the dual structural and electronic role of CNCs. Overall, CNCs function not merely as passive scaffolds but as active chiral auxiliaries that simultaneously modulate network topology, optical properties, and electron transport, providing a novel strategy for enhancing the performance of metal-free photocatalysts in CO_2 reduction [145].

Jiang et al. (2024) proposed a Zr-MOF exhibiting strong aggregation-induced emission that was successfully synthesized in situ on bacterial cellulose, forming fluorescent nanofibers. By optimizing the $ZrCl_4$ to BC ratio and using regulators, uniform monolayer MOF coating was attained using the solvothermal method. The hydroxyl-rich BC served as a growth template, enabling uniform MOF deposition and yielding a core-shell, string-bead morphology with well-dispersed 150 nm MOF nanoparticles. This composite displayed a significantly enhanced surface area of 1116 $m^2\ g^{-1}$ and microporous structure, outperforming pristine MOFs due to restricted agglomeration and optimized crystal growth via BC's spatial confinement. Additionally, BC@Zr-MOF showed improved thermal stability and stronger fluorescence with better pH resistance compared to pure MOFs, highlighting its potential in optical sensing and catalytic applications [146]. Yuan et al. (2023) constructed shapeable and rebuildable MIL-53@cellulose fiber composites via ultrasonically integrating MIL-53(Fe) with cellulose fibers. Nitrogen adsorption isotherms showed type IV behavior with pronounced hysteresis, confirming well-developed mesoporosity and a surface area of 9.75 m^2/g. The MIL-53 (De) crystals uniformly grew on CF and bonded with surface nanofibrils via hydrogen bonding and physical crosslinking, yielding a high compressive strength of 3.53 MPa. Cellulose provided abundant hydroxyl groups that facilitated adsorption and supported uniform photocatalyst dispersion, enabling >95% TC degradation in 15 min with H_2O_2 under visible light. CF enhances porosity and surface area, reinforces mechanical strength, and ensuring both structural integrity and high adsorption/photocatalytic performance [147].

Across these systems, three unifying structure–property relationships emerge: (i) Dispersion nd interface Engineering: Cellulose's abundant –OH groups strongly interact with MOF metal nodes and organic linkers, preventing aggregation and enabling uniform nanoparticle distribution. Systems with highest uniformity (e.g., Ni@MDCS/BiOBr, Zr-MOF@BC) exhibit the largest improvements in charge separation efficiency and photocatalytic rate constants. (ii) Hierarchical Porosity and mass Transport: Cellulose supports from nanofibrils to woven cotton govern macroscopic porosity, facilitating reactant accessibility and light penetration. Composites with multiscale porosity (CCF/PDA-C/Ni@MDCS/BiOBr) consistently achieve superior dye degradation due to enhanced substrate–catalyst contact. (iii) Electronic modulation and band-gap Tailoring: Interfacial interactions with cellulose can tune band gaps and alter defect states, as observed in CMC/MIL-101(Fe)/CuO and Ag_3VO_4@MIL-125-NH_2@cotton. The cellulose–MOF junction promotes charge transfer by creating local electric fields, improving photocatalytic quantum efficiency. Overall, cellulose acts as a structural, chemical, and electronic regulator within MOF-based photocatalysts. Its influence extends from nanoscale MOF nucleation and band-gap engineering to macroscopic reusability and processability. The current body of work unequivocally demonstrates that cellulose is not merely a support material

View Article Online
DOI: 10.1039/D5TA07511D

but a decisive performance-enabling component, determining photocatalytic efficiency, stability, and architectural versatility.

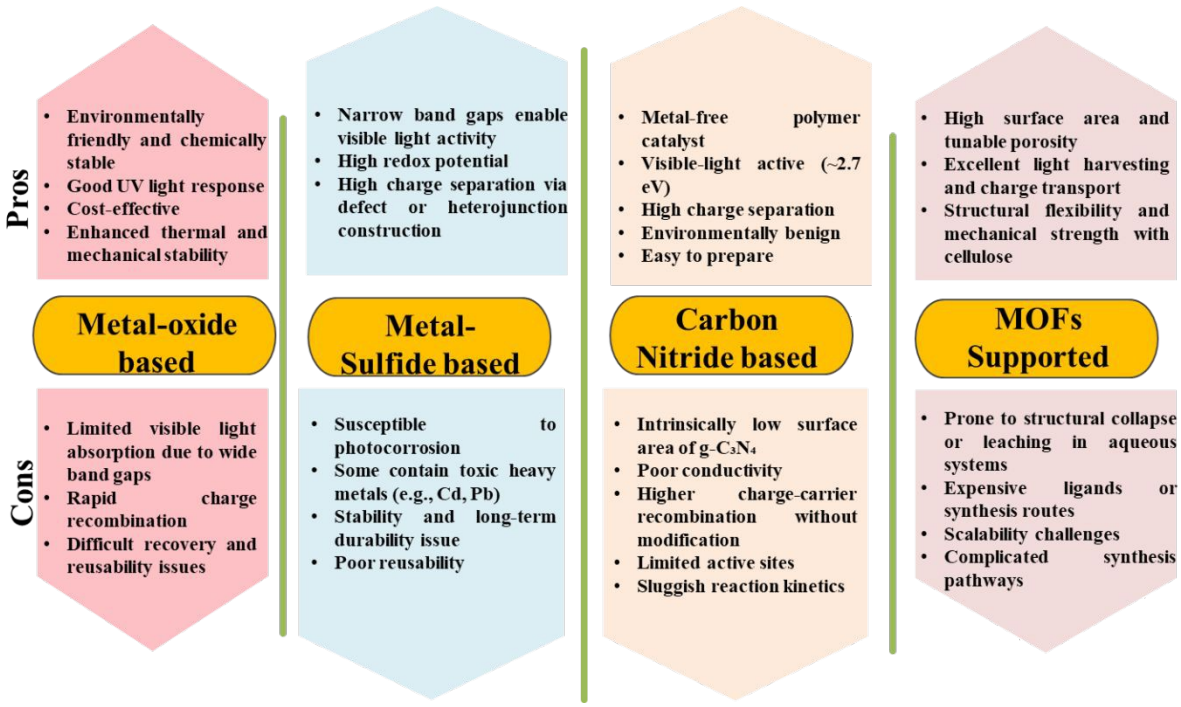

Fig. 7 Pros and Cons of cellulose-based composite photocatalysts employed for diverse applications

A horizontal comparison of cellulose based composite catalysts illuminate that cellulose not only enhance the catalytic activity, instead it influence is governed by the intrinsic band structure, chemistry and stability of the photocatalyst. **Fig. 7** Overview of the advantages and limitations of four major classes of cellulose-supported photocatalysts. In metal oxides, cellulose primarily improves dispersion, introduces hydroxyl-rich anchoring sites, and enhances pollutant adsorption, however the broader band gap and higher recombination ratios limits the utilization of visible light even in presence of cellulose. Metal sulfides exhibit a more pronounced response because their narrow band gaps and defect densities permits stronger interfacial electronic coupling with cellulose via electron/proton donation, though photocorrosion remains a major performance limiting parameter that cellulose can partially mitigate in photocatalysis. The cellulose-GCN hybrids displays strongest synergistic effects via hydrogen-bonded networks, proton coupled electron transfer pathways, and strengthened heterointerfaces significantly boost charge mobility, lower recombination ratio, and enrich the availability of active sites. MOF-supported systems feature tunable porosity, large surface area, and structural synergy with cellulose, but face issues of structural collapse in aqueous media, high synthesis costs, and scalability constraints. These differences arise from variations in interfacial electron transfer compatibility with cellulose functional group, band alignment and charge-carrier kinetics, cellulose ability to modulate electron density at the interface of semiconductor.

5.2 Structured cellulose-based photocatalytic systems

View Article Online
DOI: 10.1039/D5TA07511D

Cellulose-derived functional structures are engineered materials developed from cellulose that are designed to perform specific tasks such as catalysis or adsorption, often through chemical modification and incorporation of functional agents. The processing of cellulose into forms such as sponges, hydrogels, or aerogels serves as a porous, flexible, and mechanically stable scaffold. The construction of functional structures is ideal for photocatalytic applications due to (i) improved utilization of visible light via electron supply, (ii) higher reusability and ease of recovery, (iii) enhanced oxygen adsorption, (iv) excellent structural stability and mechanical strength, (v) tunable porosity for efficient mass transfer, and (vi) the ability to support multifunctional catalytic sites for synergistic reactions. **Table 4** describes a detailed comparison of the overview of cellulose-based hydrogels, sponges, aerogels, and membrane-based photocatalysts.

Table 4 Comparative Overview of Cellulose-Based Hydrogel, Sponge, Aerogel, and Membrane for Photocatalysis

Criteria	**Hydrogel**	**Sponge**	**Aerogel**	**Membrane**
Structure	3D-crosslinked hydrophilic network; water-swollen	Macroporous 3D framework with moderate porosity	Ultra-light 3D porous network with very high porosity and surface area	Thin 2D layer or fibrous mat with controlled porosity
Porosity	Moderate to high	Moderate	Very high (>90%)	Variable, often lower than aerogels
Preparation methods	Simple polymerization and crosslinking	Freeze-drying or thermal foaming	Sol-gel process and freeze drying	Electrospinning, casting, and phase inversion
Mechanical Strength	Soft, elastic, weak when swollen	Higher strength, compressible	Fragile without reinforcement	High mechanical stability and flexibility
Surface Area	Moderate	Low to moderate	High (up to 500 $m^2 g^{-1}$)	Moderate
Photocatalytic Efficiency	Moderate; affected by diffusion limits	Moderate; better for floating catalysts	High due to high active area	High with good contact and flow-through operation
Reusability	Can be reused; shape may deform	Reusable; compressible	Reusable; may need crosslinking for stability	Highly reusable; easy to handle and wash
Advantages	-Biocompatible - High water uptake - Easy synthesis	- Easy handling - Good mechanical stability - Suitable for floating systems	- Highest porosity and surface area - Lightweight - Excellent for adsorption-photocatalysis	- Good scalability - Ideal for continuous-flow systems

View Article Online
DOI: 10.1039/D5TA07511D

Criteria	Hydrogel	Sponge	Aerogel	Membrane
Disadvantages	- Swelling can weaken the structure - Low mechanical integrity	- Lower surface area - Limited catalyst loading	- Brittle unless reinforced - Complex fabrication - Not ideal for flow systems	- Possible nanoparticle leaching - Lower surface area than aerogels
Challenges	- Maintaining shape and structure during operation - Ensuring catalyst stability	- Uniformity in structure - Long-term stability in harsh conditions	- High energy consumption for drying - Scaling up with uniformity	- Achieving homogeneous nanoparticle distribution - Managing fouling and long-term use

5.2.1 Hydrogels

Cellulose-based hydrogels have emerged as a versatile class of photocatalytic platforms owing to their intrinsic biodegradability, hydrophilicity, and facile chemical tunability. However, pristine cellulose hydrogels suffer from low mechanical strength, insufficient visible-light activity, and limited adsorption capacity, restricting their standalone photocatalytic applicability. Recent studies address these limitations through rational integration of functional nanomaterials, and a comparative evaluation of these systems highlights the active, system-defining role of cellulose far beyond that of a passive supporting matrix [32]. Ren et al. (2022) demonstrated that cellulose can serve as an interfacial engineering framework, enabling the in-situ nucleation and homogeneous distribution of SiO_2 and ZnO within a hydrogel. Unlike conventional hydrogel scaffolds where inorganic fillers tend to aggregate, the abundant –OH groups on cellulose nanofibrils functioned as specific nucleation centers, generating a highly interconnected ZnO/SiO_2 heterojunction with defect-rich interfaces. This controlled architecture not only enhanced electron migration (ZnO → SiO_2 impurity levels) but also improved mechanical integrity and porosity. Consequently, this system achieved 95% MB degradation within 120 min and maintained >90% efficiency after eight cycles, underscoring cellulose's critical role in structural robustness and long-term catalytic durability [148].

A distinct yet complementary function of cellulose is evident in the CMC–NGO–ZnO–ZnO_2 hydrogel. Here, CMC directed the nanoscale dispersion and chemical integration of dual Zn-based phases on amine-modified graphene oxide. SEM and TEM analyses revealed that the cellulose matrix prevented rod-like ZnO and particulate ZnO_2 aggregation while mediating tight heterojunction interfaces conditions essential for rapid interfacial charge migration. Chemical analyses (FTIR and XPS) confirmed strong bonding between CMC, NGO, and Zn-based oxides. These interactions not only lowered the band gap (3.17 eV → 3.11 eV) but also promoted synergistic radical generation ($\bullet O_2^-$, •OH), enabling 100% dye degradation. The contrast with the Ren et al. system highlights an important distinction: while cellulose in ZnO/SiO_2 strengthened mechanical and interfacial frameworks, CMC here functioned as an electron transport mediator and heterojunction stabilizer, directly influencing band structure and charge

View Article Online
DOI: 10.1039/D5TA07511D

dynamics [149]. Comparing these two systems underscores that the functional form of cellulose (nanofibrillar cellulose vs. CMC) fundamentally dictates the photocatalyst architecture, interface chemistry, and electronic behavior, positioning cellulose as an active modulator of both physicochemical and photocatalytic properties.

Qi et al. (2024) employed cellulose nanofibrils (CN) as a high-surface-area reinforcement scaffold in a titanate nanofiber–CdS (TN–CdS) hydrogel. Unlike the previous two systems, where cellulose primarily served interfacial electronic roles, here cellulose dictated mass transfer, swelling behavior, and accessible surface area. The formation of a 3D porous hydrogel increased the BET surface area dramatically (31.9 $m^2 g^{-1}$ vs. 6.70 $m^2 g^{-1}$ for CN and 0.56 $m^2 g^{-1}$ for TN–CdS). This cellulose-enabled structural openness significantly improved nanoparticle dispersion and facilitated efficient light harvesting and reactant diffusion. As a result, the composite achieved a reduction rate constant of 0.0586 min^{-1}. Additionally, CdS functioned within a Z-scheme mechanism, benefiting from the stable, hydrated cellulose matrix that prevented nanoparticle recombination and deactivation. In this system, cellulose is not primarily an electronic mediator but a mass-transfer enhancer and structural stabilizer, enabling high photocatalytic efficiency through improved accessibility and reactant mobility [150].

The integration of photocatalysts into cellulose-based hydrogels enables the creation of multifunctional composites where cellulose governs mechanical durability, porous architecture, charge separation dynamics, and catalytic stability. A critical comparison reveals that cellulose's role transitions from structural stabilizer (ZnO/SiO_2) to electron-mobility facilitator (CMC–NGO–ZnO–ZnO_2) to mass-transfer enhancer (CTH–TN–CdS), positioning cellulose as a uniquely adaptive material capable of driving performance enhancements in diverse photocatalytic systems. Future work should prioritize mechanistic mapping of cellulose–photocatalyst interactions and controlled structural optimization to fully unlock cellulose's potential in scalable environmental remediation technologies.

5.2.2 Sponge

Sponges are 3D, porous, and mechanically resilient architectures values for their high surface area, low density, and efficient fluid uptake-release dynamics, which collectively enable rapid mass transfer during photocatalytic reactions [151]. Its commonly fabricated from natural or synthetic polymers, their interconnected microporous networks facilitate efficient photon penetration, reactant diffusion, and pollutant-catalyst interaction [4,152]. Among natural sponge matrices, cellulose-based sponges stand out due to their biodegradability, abundant surface OH groups, and chemical tunability, enabling diverse functionalization strategies and nanoparticle anchoring [153]. Such features make cellulose a privileged scaffold for designing next-generation photocatalytic platforms.

Liu et al. (2023) employed hydrothermally induced phase separation coupled with in-situ synthesis nucleation to immobilize $NaBiS_2$ within chitosan/cellulose sponges. The resulting hierarchical macro-sponges ranging from 150-1500 μm, and supported with uniformly distributed $NaBiS_2$ nanoparticles of 70-90 nm. The sponges exhibited a narrow band gap of 1.18 eV, high photocurrent density (0.74 μA cm^{-2}), and excellent mechanical compressibility. The combination of cellulose's hydrogen-bonded framework with chitosan's functionality enabled enhanced mechanical stability and efficient light harvesting. NaBiCCSs combine their high affinity for dyes with a synergistic adsorption–photocatalytic degradation process, achieving a methylene blue removal efficiency of 98.38 % under visible light and

View Article Online
DOI: 10.1039/D5TA07511D

showing excellent reusability. [30]. Similarly, You et al. (2022) fabricated ZnS nanoparticle-decorated cellulose-chitosan sponges via hydrothermal decomposition of xanthates and in situ synthesis of ZnS nanoparticles. The sponges exhibited high porosity, very low bulk density, and uniform distribution of ZnS, while maintain structural integrity even after severe 80% compression fatigue cycles. Their reduced band gap of ZnS sponges (3.2-3.55 eV), relative to bulk ZnS arose from quantum confinement due to minimized agglomeration, an effect made possible by the cellulose scaffold preventing particle coalescence. This underscores cellulose's critical role in stabilizing nanoscale photocatalysts. ZnCCSs exhibit a high Congo red removal efficiency of 96.53 % and maintain excellent stability over multiple reusability cycles [154].

In another example, self-supporting and floating photocatalytic cellulose sponges were engineered by anchoring BiOX nanosheets, aided by sodium alginate to improve electrostatic attraction of Bi and O ions which helps in promoting nucleation of BiOX crystals. The hybrid sponges exhibited visible-light-active band gaps of 1.85 eV, and a hydrophobic water contact angle of 125^{o}, attributed to the ordered nanosheet alignment. Their buoyancy allowed enhanced light exposure and oxygen availability conditions that is unavailable in denser slurry catalysts. The hydrophobicity places the sponge in a transitional wetting state between Wenzel and Cassie models, suggesting balanced interfacial properties suitable for aqueous-phase photocatalysis [153]. Cellulose's low density and modifiable surface chemistry were essential in achieving these functionalities. Assanvo et al. (2023) developed a low-cost, environmentally friendly, and biodegradable magnetic hybrid biosponge composite using collagen and kenaf fibre cellulose (KFCC) loaded with TiO_2 and Fe_3O_4. The hybrid sponges exhibited ferromagnetism (saturation magnetization =8.6 emu g^{-1}) tunable mesoporosity (40 m^2 g^{-1}), surface area of 40 m^2 g^{-1}. and pore volume (0.042 cm^3 g^{-1}). The as-prepared magnetic hybrid bio-sponge achieved a photocatalytic degradation efficiency of 91.2 % for crystal violet under visible light and 86.6 % under direct sunlight [155]. Recently, Xia et al. (2025) synthesized $ZnIn_2S_4$ nanoparticles loaded cellulose/chitosan composite sponges via in-situ hydrothermal phase separation. The $ZnIn_2S_4$ composite sponges displayed interconnected macropores of 150–500 µm, with uniformly distributed nanoparticles of 15 nm in size, a narrow band gap of 2.88 eV, and excellent compressibility. The abundant hydroxyl and amino groups on cellulose/chitosan facilitated dense nanoparticles anchoring and improved adsorption of pollutants, enabling synergistic adsorption-photocatalyst performance. The prepared $ZnIn_2S_4$ composite sponge achieved a tetracycline removal efficiency of up to 91.5 % under sunlight irradiation and retained its performance after eight consecutive cycles [156].

In summary, cellulose-based photocatalytic sponges function as lightweight, microporous and chemically versatile platforms that uniquely support high nanoparticle dispersion, tunable band structures, and robust mechanical behavior. Across the surveyed systems- from $NaBiS_2$ to ZnS, BiOX, TiO_2–Fe_3O_4, and $ZnIn_2S_4$ the role of cellulose is consistently central: it governs nanoparticle nucleation, minimizes agglomeration, enhances charge transfer interfaces, enabling floating or magnetically recoverable designs and provides abundant active sites for adsorption-photocatalysis coupling. This attributed highlight cellulose not merely as a structural filler but as a functional co-component that significantly elevates photocatalytic efficiency. Collectively, cellulose-engineered sponges represent a low-cost,

View Article Online
DOI: 10.1039/D5TA07511D

sustainable, and highly adaptable class of photocatalyst with strong potential for large scale environmental remediation.

5.2.3 Aerogels

Aerogels are highly porous, lightweight solid materials characterized by lower density, higher surface area, porosity, and adsorption capacity [157]. These spongy-like structures are formed by replacing the liquid component of gel with gas, while preserving the solid network, which makes them suitable for environmental applications [158]. Aerogels ensure rapid diffusion of pollutants and efficient interaction with active sites. For example, Amaly et al. (2022) explained the construction of a flexible and reusable metal-free aerogel composite composed of montmorillonite hosting methylene blue and microcrystalline cellulose (MCC). The MCC served as the base for aerogel construction, thanks to its strength, water compatibility, and affordability. Additionally, montmorillonite was incorporated to support MB and enhance pollutant adsorption through an ion exchange process with Al^{3+}. The hydrogen bonds between MCC and montmorillonite helped to form a highly stable structure, and the freeze drying of hydrogels leads to the formation of lightweight, porous aerogels. The surface area and density of aerogel were 148 $m^2 g^{-1}$ and 40 mg cm^{-3}, respectively. The MCC/MT-MB aerogel achieved 97% tetracycline removal within 120 min, owing to the MCC-derived 3D porous network that enhanced pollutant adsorption, improved catalyst dispersion, and accelerated mass transfer throughout the photocatalytic process [159].

Liu et al. (2025) developed GCN/reduced graphene oxide (rGO)/CNF aerogels through a facile bidirectional freeze drying and thermal reduction strategy. The rGO acted both as a support and an electron transfer channel, helping to speed up electron-hole separation and transport. The dispersed CNFs supported the structure and likely improved the mechanical strength of the aerogel. The GCN/rGO/CNF aerogels exhibited a very low density of 6.45 mg cm^{-3} and layered structures with 19 micrometer spacing. On the other hand, the aerogels made without CNF collapsed and lost shape, showing that the CNF helped to prevent rGO/GCN restacking and acted as a structural skeleton to enhance strength. The carbon nitride/rGO/CNF aerogels exhibited superior compressibility and strength, retaining 96.1% height and 92.7% stress after 100 cycles, due to strong interactions between rGO and carbon nitride layers. The GCN/rGO/CNF aerogels had a specific surface area of 32.85 $m^2 g^{-1}$ and a pore volume of 0.11 $cm^3 g^{-1}$, which increased with carbon nitride content, reaching a maximum surface area of 66.63 $m^2 g^{-1}$. The GCN/rGO/CNF aerogels exhibit enhanced visible light absorption and suppressed recombination, which is ascribed to a 3D structure that promotes multiple light reflections [114]. Hexagonal nanocrystalline CdS was synthesized via a solvothermal method, loaded onto PEI-modified cellulose, and fabricated into aerogels (PNFCA/CdS-2) through freeze drying. The resulting aerogel exhibited a staggered 3D network with uneven mesopores (2-50 nm), offering high surface area, and abundant active sites conductive to the transport of pollutants and adsorption. Nitrogen adsorption-desorption isotherms confirmed type IV behavior, indicating mesoporosity. The hybrid aerogels exhibited higher surface area, enhancing photocatalytic performance by enhancing redox-active sites and promoting visible light absorption. The PNFCA/CdS-2 exhibited a band gap of 1.9 eV, from 2.17 eV (CdS), also facilitating efficient electron generation and transfer under visible light irradiation. Under optimized conditions, MO and MB removal efficiencies reached 99.56% and 100%, respectively [160].

View Article Online
DOI: 10.1039/D5TA07511D

Zou et al. (2022) developed a sulfated lignocellulose nanofibril/TiO_2 (C-SLCNF–TNP) hybrid aerogel using a deep-eutectic-solvent-assisted extraction route that introduced ionic groups and weakened internal hydrogen bonding, enabling formation of a highly porous, hydroxyl-rich 3D network. The resulting aerogel exhibited high surface area (95 $m^2 g^{-1}$), elevated charge density (1.78 mmol g^{-1}), low swelling, and strong mechanical stability, providing an ideal scaffold for uniform TiO_2 anchoring through covalent and hydrogen-bond interactions. These cellulose–TiO_2 interfacial interactions reduced the band gap from 3.20 to 2.74 eV and enhanced charge separation by enabling the SLCNF matrix to act as an electron acceptor. The porous lignocellulosic framework delivered exceptional adsorption capacity toward tetracycline (70 mg g^{-1}), far exceeding cellulose-only and TiO_2-only controls, while the integrated adsorption–photocatalysis system achieved 94.9% removal [161]. While cellulose-based aerogels demonstrate impressive photocatalytic efficiencies owing to their high porosity, 3D mass-transfer pathways, and ease of functionalization, several key limitations remain unresolved. Most reported systems rely on optimized laboratory conditions, and their performance under realistic matrices, variable pH, or competing pollutants is largely untested. Moreover, differences in fabrication routes including freeze-drying, solvothermal loading, bidirectional freezing introduce challenges in reproducibility and scalability that are rarely quantified. Although band-gap tuning and heterojunction engineering improve visible-light response, mechanistic understanding of charge migration within the cellulose framework is still limited. Overall, cellulose aerogels offer a compelling platform, but their practical deployment will require standardized benchmarking, long-term stability assessment, and scalable synthesis strategies.

5.2.4 Membranes

Cellulose-based photocatalytic membrane have emerged as highly versatile platforms for environmental remediation, combining sustainability, mechanical robustness, and excellent film-forming ability [162]. Unlike conventional polymeric supports, cellulose function as an active functional matrix, whose abundant hydroxyl groups enable strong anchoring of photocatalytic nanoparticles, facilitates surface modification, and regulate interfacial interactions. These properties enhanced mass transfer, light penetration, and pollutant adsorption, establishing cellulose as a key determinant of membrane performance [163].

For example, Lu et al. (2021) fabricated a cellulose-based β-FeOOH@MIL-100(Fe)/polyvinyl pyrrolidone electrospun nanofiber membrane via electrospinning and in situ synthesis. Here, deacetylated cellulose acetate/polyvinyl pyrrolidone nanofibers serve as a flexible porous core, supporting a photocatalytically active sheath of β-FeOOH@MIL-100(Fe) heterojunctions. The cellulose's high surface reactivity, tunable porosity, and abundant hydroxyl groups enable strong anchoring and uniform dispersion of catalysts. This core-sheath structured ENM features ultrahigh catalyst loading (78 wt%), large surface area (1105 $m^2 g^{-1}$), and enhanced hydrophilicity, transitioning from a WCA of 133° to super hydrophilic (0°) after surface functionalization. The flexible biodegradable matrix ensured environmental safety, while the rough, hydrophilic surface architectures boost oil-water separation [164]. Similarly, cellulose-MIL-88A membranes prepared via one-step deposition highlighting cellulose-mediated MOF immobilization through hydrogen bonding and coordination interactions. The hydrophilicity of the membrane increased with higher MIL-88A loading, as evidenced by a reduction in water contact angle from 86.2° to 4.8° facilitated water permeation and promoted efficient radical generation during photo-Fenton reaction (100%

View Article Online
DOI: 10.1039/D5TA07511D

degradation). The fibrous morphology and hydrogen-bond network also provide mechanical flexibility, and structural integrity enabling repeated filtration–regeneration cycles. This underscores cellulose's dual role like stabilizing the catalyst while actively controlling mass transport and catalytic efficiency [165].

Mixed matrix membrane (MMMs) represents a promising class of composite materials that synergistically integrates the desirable properties of polymeric matrices with functional fillers, such as photocatalysts, to enhance the separation performance, stability, and functionality. Wu et al. (2020) constructed a mixed matrix membrane composed of carbon-sphere-TiO_2 as the core-shell and hydrophilic CNF via a simple vacuum filtration method. In CNF membranes embedding TiO_2-carbon spheres, cellulose fibers create a porous, interwoven network that ensures uniform particle dispersion, improved mesoporosity, and enhanced water permeability. These features make TiO_2@carbon spheres more effective for photocatalytic water treatment than their Pt/TiO_2 counterparts. In contrast, Pt/TiO_2 nanoparticles tend to aggregate, limiting light scattering and reducing photocatalytic efficiency. Here, cellulose not only supports the filler physically but modulates light penetration, mass transport, and antifouling properties, resulting in superior water treatment performance compared to conventional polymeric MMMs. The presence of CNF in the membrane scatters light and modulates light penetration, impacting photocatalytic activity, water permeability, and antifouling performance [166]. Rajeswari et al. (2017) explained that the cellulose acetate-polyurethane membrane incorporated with ZnO nanoparticles was fabricated using a blending technique. The SEM analysis revealed the uniform rod-like morphology of ZnO and pore formation on the membrane surface, indicating an asymmetric structure with microcavities. AFM analysis showed that ZnO incorporation led to a smoother, more uniform surface with reduced surface roughness compared to the valley-like texture of the pristine CA-PU membrane. Thermal analysis demonstrated enhanced thermal stability in the ZnO-loaded membrane, with maximum degradation shifting from 170 to 280 °C, attributed to solvent evaporation and water loss. The ZnO-blended CA–PU membrane exhibited enhanced water flux and superior photocatalytic degradation of Reactive Red 11 and Reactive Orange 84 dyes [167].

Yin et al. (2022) developed a superhydrophobic cellulose membrane through in situ deposition of MnO_2 micro/nanoparticles followed by stearic acid (STA) modification. The membrane exhibited enhanced mechanical strength (+2.6%) and remarkable environmental durability, including resistance to acids, alkali, high temperature, abrasion, and self-cleaning functionality. FESEM images confirmed that MnO_2 nanoparticles tightly anchored onto cellulose microfibers, creating a multiscale rough architecture essential for superhydrophobicity. STA encapsulation further established a stacked, air-trapping interface. This synergistic roughness–chemistry combination yielded an ultrahigh water contact angle of 162 ± 2°. The structural analyses (XRD, FT-IR, XPS) verified MnO_2 incorporation and reduced surface energy after STA coating. The superhydrophobic CM sample showed strong photocatalytic performance, achieving over 98% degradation of MB. cellulose's reactive hydroxyl groups, tunable porosity, and flexible fiber network enabled efficient nanoparticle immobilization and hierarchical roughness formation [168].

Across these systems, cellulose consistently acts as the primary performance regulator: it dictates catalyst dispersion, interfacial interactions, wettability, mass transfer, and structural stability. While the choice of photocatalyst governs chemical activity, cellulose determines how efficiently these catalysts are deployed in practical membranes. Its hydroxyl-rich fiber network enables hydrogen-bonding and coordination interactions, modulates light scattering, and

View Article Online
DOI: 10.1039/D5TA07511D

creates stable hydration layers, facilitating superior water permeability, pollutant accessibility, and recyclability. Compared to conventional polymeric supports, cellulose-based membranes integrate multifunctionality, structural resilience, and environmental compatibility, establishing cellulose as an indispensable component in next-generation photocatalytic membranes.

6. Applications of Cellulose-based Photocatalysts

6.1 Energy

The extensive use of fossil fuels has enabled industrial and economic growth but has caused major environmental issues, including pollution, greenhouse gas emissions, and resource depletion [169], which threaten both human and ecological well-being. As a result, global research is shifting toward clean, renewable energy options [170]. Solar energy, being abundant and sustainable, is especially attractive, and its conversion into fuels such as hydrogen provides a strong pathway toward energy security and reduced environmental impact [46]. In this context, cellulose-semiconductor photocatalysis has gained attention for solar-driven production of hydrogen, H_2O_2, NH_3, and CO_2-derived value-added carbon products (**Fig. 8**). Photocatalysis operates by absorbing sunlight in a semiconductor with a suitable bandgap, producing electron–hole pairs. The excited electrons drive reductions of H^+, O_2, N_2, or CO_2, while holes oxidize water or sacrificial agents to balance charge. The efficiency of these reactions relies on strong charge separation, proper band-edge alignment with redox potentials, and effective adsorption and activation of reactants.

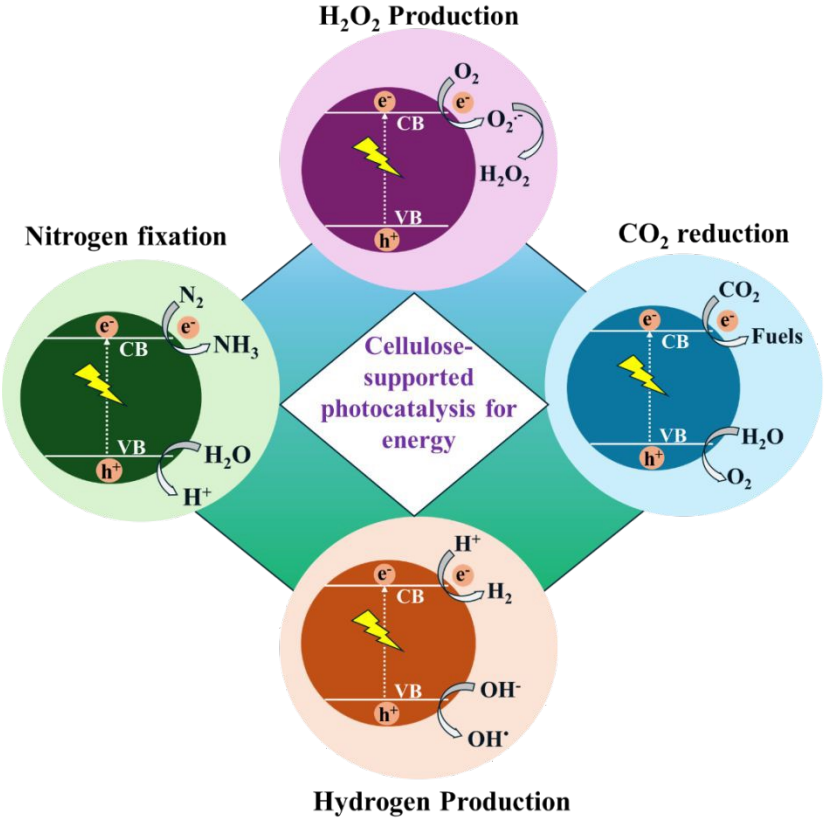

View Article Online
DOI: 10.1039/D5TA07511D

Fig. 8 Potential applications of cellulose-supported photocatalysts in energy remediation, including hydrogen, hydrogen peroxide, ammonia production, and carbon dioxide reduction

6.1.1 Hydrogen production

Photocatalysis harnesses sunlight to generate electron–hole pairs that drive redox reactions, enabling the direct conversion of solar energy into chemical fuels. One of the most promising applications of this process is water splitting for sustainable hydrogen production. During the hydrogen evolution reaction (HER), photoexcited electrons reduce protons at the catalyst surface to generate hydrogen gas, while the corresponding holes oxidize water or a sacrificial agent [171]. This dual process prevents electron–hole recombination and maintains charge neutrality, ensuring continued photocatalytic activity.

Zhou et al. (2019) developed a 2D porous CdS nanosheet supported on bacterial cellulose (BC@CdS), which was synthesized via a bio-templating method. The BC scaffold provided structural control and enhanced photocatalytic performance under visible light, achieving a H_2 evolution rate of 928 μmol h^{-1} g^{-1} with a reusability of five cycles. The enhanced performance arises from: (i) a clean 2D CdS architecture that increases light absorption, accelerates charge separation, and improves redox ability; and (ii) tunable BC nano-windows that promote efficient interfacial contact and mass diffusion. The FTIR analysis revealed strong interactions between CdS nanocrystals and BC hydroxyl groups, evidenced by broadening of the -OH peaks and shifts in δC–H vibrations[172]. The hierarchical bi-nano-composites foam composed of $Zn_xCd_{1-x}S$ nanoparticles embedded within BC has demonstrated higher visible light-driven H_2 production. The photocatalysts were synthesized via templated mineralization and ion exchange seeded growth. The optimized $Zn_{0.09}Cd_{0.91}S$/BC composite achieved an impressive H_2 evolution rate of 1450 μmol h^{-1} g^{-1} with an apparent quantum efficiency of 12% at 420 nm. The photocatalytic activity of $Zn_xCd_{1-x}S$/BC is highest for $Zn_{0.09}Cd_{0.91}S$/BC, correlating with its large surface area, abundant surface defects (lowest PL intensity), and suitable band gap (2.33 eV). These features enhance electron–hole separation and provide more active sites for water-splitting H_2 evolution, with S^{2-} and SO_3^{2-} acting as hole scavengers, highlighting the integrated role of surface structure, defects, and crystallinity in boosting photocatalytic performance [173].

Chen et al. (2023) developed an edge-modified CN photocatalyst (CHC–CN5) by grafting cellulose-derived carbon species onto CN edges, where the cellulose component served as electron-attracting sites that promoted directional electron migration, enhanced charge separation, and reduced e^--h^+ recombination. This modification also broadened light absorption and improved carrier transport by lowering resistivity, leading to superior photocatalytic performance with a hydrogen evolution rate of 3436 μmol h^{-1} g^{-1} and 80.2 % tetracycline degradation in 60 min, markedly outperforming pristine CN (**Fig. 9 ia-b**) [174]. The CdS nanoparticles immobilized within porous regenerated cellulose films have been explored for hydrogen production under visible light. By adjusting the cellulose solution concentration, the mean pore size of the RC films was tuned from 57 to 20 nm with a simultaneous increment in CdS loading. The embedded CdS nanoparticles were well dispersed within the cellulose matrix, which enhanced the light absorption and improved mechanical properties. The Pt-loaded CdS/RC film prepared from 4.5% cellulose solution exhibited a high H_2 evolution rate of 1.323 mmol h^{-1} g^{-1} (**Fig. 9 i c**), attributed to efficient light harvesting, rapid

View Article Online
DOI: 10.1039/D5TA07511D

charge transfer, and robust catalyst–electrolyte interaction [175]. In the CF/PDA/ZnS composite paper, cellulose fibers act as a robust, porous scaffold that enhances mechanical stability, provides high surface area for uniform ZnS nanoparticle dispersion, and ensures strong anchoring of the photocatalyst via PDA, preventing particle loss during repeated cycles. This structural support facilitates efficient contact between reactants and active sites, while the ZnS/PDA type-II heterojunction on the cellulose surface promotes directional electron transfer, reduces electron–hole recombination, and boosts photocatalytic redox activity. Consequently, the composite exhibits superior hydrogen evolution (18,706 μmol h^{-1} g^{-1}), high apparent quantum yield (11.6 %), and excellent durability (96 % retention after three cycles) (**Fig. 9 i d**) [176].

The integration of cellulose with semiconductor photocatalysts presents a sustainable and versatile platform for hydrogen production (**Table 5**). Cellulose-supported photocatalysts demonstrate dramatically improved performance over their non-cellulose counterparts. For example, porous CdS sheets anchored on cellulose achieved 928 μmol h^{-1} g^{-1} compared to 36 μmol h^{-1} g^{-1} for pristine CdS, and CHC-CN5 showed an increase from ~600 μmol h^{-1} g^{-1} to 3634 μmol h^{-1} g^{-1} under visible light. These enhancements highlight cellulose's role in providing a high-surface-area scaffold, improving charge separation, and facilitating reactant adsorption, resulting in both higher activity and sustained reusability. However, some limitations remain, including the relatively high cost and limited long-term stability of noble metal cocatalysts, as well as reduced efficiency under natural irradiation compared to simulated light. Addressing these issues is critical for practical deployment. Moving forward, several key perspectives can guide further research:

- While several cellulose-based systems exhibit excellent lab-scale apparent quantum efficiencies, the translation to high quantum efficiencies under natural sunlight remains a challenge. Future research should focus on band gap engineering and heterojunction design to broaden light absorption across the visible and near infrared regions.
- Development of cellulose-based photocatalytic papers, foam, and hydrogels supports device-level scalability. Such systems enable floating, solid-gas biphasic configurations, which not only reduce mass transfer limitations but also show great potential for outdoor hydrogen production from humid air or solar steam.
- Cellulose-based photocatalysts could be integrated into photoelectrochemical systems, serving as flexible, porous photocatalytic layers that facilitate gas evolution and electrolyte diffusion, enhancing overall system efficacy.

Table 5 Summary of different catalysts use for hydrogen production via photocatalysis

Catalyst system	Light source	Non-cellulose benchmark performance	Cellulose-supported photocatalyst performance	Reusability	Reference
Porous CdS sheets	300 W Xe lamp	CdS:36 μmol h^{-1} g^{-1}	928 μmol h^{-1} g^{-1}	4	[172]

View Article Online
DOI: 10.1039/D5TA07511D

CHC-CN5	Visible lamp	CN: 600 μmol h^{-1} g^{-1}	3634 μmol h^{-1} g^{-1}	4	[174]
Pt-CdS/regenerated cellulose film	250-W Xe	CdS film: 0.652 mmol g^{-1} h^{-1}	1.323 mmol g^{-1} h^{-1}	3	[175]
CF/PDA/ZnS composite	300 W Xe lamp	CF/ZnS: 5805 μmol h^{-1} g^{-1}	18706.8 μmol h^{-1} g^{-1}	3	[176]
Cu/Ni-TiO_2 cellulose	UV LED lamp	TiO_2: 125 μmol h^{-1} g^{-1}	489 μmol h^{-1} g^{-1}	-	[177]

6.1.2 Hydrogen peroxide production

Hydrogen peroxide (H_2O_2) has garnered significant attention as a green oxidant due to its high active oxygen content, environmentally benign byproducts, and broader applicability in medical, chemical, energy, and environmental sectors [178]. However, the conventional production methods, such as the Anthraquinone process, are energy-intensive and environmentally burdensome, while direct synthesis from hydrogen and oxygen involves safety and scalability challenges [15]. In this context, the photocatalytic production of H_2O_2 using solar energy offers a sustainable, safe, and decentralized alternative [170]. The cellulose-supported photocatalysts have shown great promise, leveraging the structural tunability, and functional diversity to enhance light absorption, charge transfer, and oxygen activation for efficient H_2O_2 generation [36,73]. For H_2O_2 production, the CB electrons reduce molecular oxygen (O_2) via a two-electron pathway to form H_2O_2, rather than the four-electron pathway to water. This selectivity is favored by appropriate tuning of band positions and surface sites. Concurrently, the holes oxidize water or organic donors to regenerate the catalyst surface [36,179].

Highly efficient GCN/carboxylated cellulose nanofibers (CNF) were developed by rationally extending hydrogen bonds/π-bonds intermolecular networks between GCN and carboxylated CNF and polydopamine to enhance solar-driven peroxide synthesis. The photocatalyst exhibited a remarkable H_2O_2 generation rate of 130 μmol L^{-1} h^{-1}, significantly surpassing that of pure GCN. This improvement was attributed to the enhanced interaction between GCN and carboxylated CNF through hydrogen bonding and π-π stacking, which facilitated superior oxygen adsorption, accelerated charge carrier separation, and efficient charge transfer. In in-situ FT-IR spectroscopy, the bands at 1156, 1278, and 1362 cm^{-1} corresponded to $\cdot O_2^-$, O-O stretching of surface-adsorbed ·OOH, and the bending mode of ·HOOH, confirming H_2O_2 formation via a $\cdot O_2^-$ intermediate pathway. The bands at 1103 and 1434 cm^{-1}, attributed to C-OH and C-O bonds, indicated the presence of OH species, a key intermediate in this process. The theoretical calculations and experimental data confirm that the introduction of CNF enhances O_2 adsorption, separation, and transfer of photogenerated charge carriers [66]. Balakrishnan et al. (2024) synthesized a homojunction through a simple wet impregnation method, comprising phosphorylated and sulfur-self-doped g-C_3N_4 (SPGCN). The homojunction system was subsequently integrated into hydrogel beads using CMC through a crosslinking reaction, resulting in the formation of SPGCN/CMC beads. The photocatalytic studies demonstrated a notable H_2O_2 production of 3.5 mM after 60 min with a reusability of 10 cycles. The higher catalytic activity is attributed to the improved visible light

View Article Online
DOI: 10.1039/D5TA07511D

absorption through proper tuning of the band gap, which ensures the utilization of light in a broader spectrum. The suppression of electron-hole pairs is achieved through the construction of a Z-scheme between phosphorylated and sulfur-self-doped g-C_3N_4 (**Fig. 9 iia**). The mechanistic studies also indicated that superoxide radicals were involved in the generation of H_2O_2 with the reaction following a selective two-electron reduction pathway [36].

In another study, hydrothermal carbonaceous carbon (HCC) was assessed for H_2O_2 production due to its semiconductor properties, despite its slower charge carrier separation and energy utilization. Thus, pyrrole-doped HCC (PHCC) was prepared using cellulose from balsa wood and pyrrole. The resulting π-conjugated structure, formed by the stacking of electron donor furan units and acceptor pyrrole units, reduces the band gap, enhances light absorption, and accelerates charge transfer, while reducing particle size to expose more active sites. The PHCC achieved an impressive H_2O_2 production of 1.4 mM under simulated sunlight, which is 3.8 times higher than its pyrrole-free catalyst. This enhancement is ascribed to improved energy utilization, faster oxygen reduction kinetics, and a photothermal-assisted effect. The theoretical calculations showed that the furan-pyrrole-alternating structures may optimize energy levels, improve charge separation efficacy and enhances oxygen adsorption/activation, driving the increased photocatalytic H_2O_2 synthesis [180]. Zhou et al. (2024) proposed anchoring of aldehyde functionalized cellulose nanofibers onto GCN microtubes through covalent and hydrogen bonding. The grafting of functionalized nanofibers onto the GCN microtubes is achieved via amide bonding between the aldehyde groups of the nanofiber and amino groups at the edge of GCN microtubes heptazine ring. The incorporation significantly improved the wettability of GCN, promoting the oxygen adsorption. The experimental and DFT calculations revealed that the firm surface interfacial interactions have boosted the electron transfer, facilitating an efficient single-electron oxygen reduction reaction for H_2O_2 production of 67.44 μmol L^{-1}. As highlighted in **Fig. 9ii b,** under the illumination of visible light, photoexcited electrons migrate to the aldehyde functionalized CNF, facilitating H_2O_2 generation via a two-step single-electron oxygen reduction pathway [181].

Cellulose-supported photocatalysts have emerged as up-and-coming platforms for the sustainable and efficient production of H_2O_2 (**Table 6**), owing to their abundant functional groups, higher surface area, and excellent structural tunability. For instance, g-C_3N_4 homojunctions with nanofibrous carbon reach 136.9 μmol L^{-1} versus 27.5 μmol L^{-1} for pristine GCN, and metal-free cellulose-derived catalysts achieve 2.09 mmol h^{-1} g^{-1}, highlighting the benefits of cellulose in improving charge separation, surface area, and active site accessibility. Predominantly, cellulose and its derivatives such as carboxylated, sulfonated, phosphorylated, and aldehyde functionalized nanofibers have been integrated with carbon nitride frameworks to form highly active photocatalytic systems. These composites exploit hydrogen bonding, π-π interactions, covalent linkages, improve oxygen adsorption, and facilitate selective two-electron-oxygen reduction pathways for H_2O_2 synthesis. However, future development of cellulose-supported photocatalysts should focus on several key directions, including: (i) Rational engineering of cellulose through targeted functional group modification can further tune electronic interactions and catalytic interfaces. Simultaneously, non-metal heteroatom doping and utilization of carbon substrates can modulate band structures and facilitates interfacial charge transfer dynamics. (ii) The utilization of in-situ spectroscopic techniques such and Fourier Transform infrared spectroscopy (FTIR), and electron paramagnetic resonance (EPR) combined with density functional theory (DFT)

View Article Online
DOI: 10.1039/D5TA07511D

simulations will be crucial to unravel reaction intermediates, charge migration pathways, and active sites structures, thereby enabling more predictive catalyst design. (iii) To transition this system toward industrial relevance, comprehensive life-cycle assessments and techno-economic analyses must be conducted to evaluate sustainability and cost-effectiveness of cellulose based photocatalysts with respect to conventional production strategies.

Table 6 Summary of different photocatalysts employed for hydrogen peroxide production

Catalyst	Light Source	Non-cellulose benchmark performance	Cellulose-supported photocatalyst performance	Reusability	Pathway	Reference
KOH-activated bagasse cellulose carbon aerogel ZnO composite	300 W Xe lamp	NA	96.39 mmol L^{-1}	5	Two-step-two-electron oxygen reduction	[182]
Spent Coffee ground derived biochar	300 W Xe lamp	Hydrochar: 0.341 mmol L^{-1}	0.61 mmol L^{-1}	5	1-electron reduction oxygen reaction	[183]
Aldehyded cellulose nanofibers/GCN	300 W Xe lamp	CN: 0.01679 mmol L^{-1}	67 µmol L^{-1}	-	Two-step-two-electron oxygen reduction	[181]
Furan-resin-structured hydrothermal carbon	300 X white LED light	-	480 µmol L^{-1}	6	Two-step-two-electron oxygen reduction	[184]
GCN homojunction with nanofibrous carbon	300 W Xe lamp	GCN: 27.5 µmol L^{-1}	136.9 µmol L^{-1}	-	Two-step-two-electron oxygen reduction	[185]
Hydrothermal carbonaceous carbon	300 W Xe lamp	NA	1.16 mmol h^{-1} g^{-1}	-	Two-step-two-electron oxygen reduction	[186]
Metal-free catalyst from cellulose	Visible	NA	2.09 mmol h^{-1} g^{-1}	-	Two-step-two-electron	[187]

View Article Online
DOI: 10.1039/D5TA07511D

					oxygen reduction	
Defect-rich and dimensionally confined double functionalized GCN homojunction hydrogel	250 W medium-pressure Hg lamp	GCN: 0.075 mmol h^{-1} g^{-1}	1.05 mmol h^{-1} g^{-1}	6	Two-step-two-electron oxygen reduction	[94]
In_2S_3/Bi_2WO_6/CdS hydrogel	250 W medium-pressure Hg lamp	GCN:<100 μmol L^{-1}	302 μmol L^{-1}	5	Two-step-two-electron oxygen reduction	[188]
Ternary carbon nitride homojunction hydrogels	250 W medium-pressure Hg lamp	Bi_2WO_6: 125 μM	1204 μmol L^{-1}	5	Two-step-two-electron oxygen reduction	[56]

6.1.3 Carbon dioxide reduction

The accelerating pace of scientific and technological development has intensified global energy consumption, deepening reliance on fossil fuels and elevating CO_2 emissions, with atmospheric concentrations projected to rise from 400 to 750 ppm. As global energy demand is expected to increase by 28% by 2040, the need for sustainable and eco-friendly strategies for clean energy generation and carbon mitigation has become urgent [189]. Photocatalytic CO_2 reduction offers a promising pathway by using water as an electron donor to convert CO_2 into value-added fuels such as CO, CH_4, CH_3OH, and formic acid [190,191]. Integrating cellulose-based materials as supports or templates has recently gained traction, as they enhance photocatalytic performance by improving charge separation, increasing active surface area, and strengthening CO_2 adsorption.

Shi et al. (2022) demonstrated that cellulose fibers (30–50 μm) serve as effective templates for synthesizing 3D CuO–ZnO (CuO–ZnOCel-T) and Cu–ZnO (Cu–ZnOCel-T) nanocomposites for solar-driven CO_2 conversion. The abundant hydroxyl groups and fibriform structure of cellulose facilitated uniform nanoparticle dispersion and prevented aggregation, unlike carbon fiber-supported or template-free CuO–ZnO, which suffered from severe clustering and lower catalytic activity. CuO–ZnOCel-T achieved a CO production rate of 8.61 μmol g^{-1} h^{-1} (99.8% selectivity), outperforming CuO–ZnOC-T (4.10 μmol g^{-1} h^{-1}) and bare CuO–ZnO powder (0.84 μmol g^{-1} h^{-1}). Remarkably, metallic Cu^0 incorporation via wheat-straw reduction in Cu–ZnOCel-T increased CO production to 30.17 μmol g^{-1} h^{-1}, highlighting the synergistic effect of surface plasmon resonance (SPR) and enhanced charge separation. Structural and spectroscopic analyses (HRTEM, XRD, XPS, PL, EIS) confirmed high nanoparticle dispersion, oxygen defects, and efficient electron-hole separation, while photocurrent measurements validated

View Article Online
DOI: 10.1039/D5TA07511D

improved carrier transfer. Optimizing the Cu/Zn ratio (1:4) further enhanced activity, and the catalyst maintained 87% performance over six cycles, demonstrating excellent stability [192].

Aminated cellulose nanocrystals (NCC-EDA) serve as an effective multifunctional support for TiO_2, enhancing crystallinity, charge separation, and CO_2 adsorption. XRD and TG analyses confirm that NCC-EDA promotes the formation of high-crystallinity anatase TiO_2, while TEM shows that the NCC-EDA coating reduces TiO_2 particle size (~20 nm) and prevents crystal overgrowth. Surface characterization (EDX, XPS, FTIR, Raman) demonstrates strong interaction between amino groups and TiO_2, with graphitized cellulose structures analogous to graphene, facilitating electron transfer and suppressing e^-–h^+ recombination. The TiO_2/NCC-EDA composite exhibits a reduced band gap (2.86 eV vs. 3.17 eV for TiO_2), extended visible-light absorption, increased BET surface area (174 $m^2 g^{-1}$ vs. 43 $m^2 g^{-1}$), and enhanced CO_2 adsorption. Photocurrent, PL, and EIS studies confirm that NCC-EDA accelerates charge separation and maintains sustained electron availability under illumination. As a result, CO_2 reduction to $HCOOCH_3$ is 4.5 times higher than pure TiO_2 (372.85 μmol g^{-1} in 6 h), with optimal activity at 54 g L^{-1} NCC-EDA. Mechanistically, NCC-EDA acts as an electron mediator and structural stabilizer, enabling efficient CO_2 activation and conversion while minimizing electron-hole recombination. Overall, cellulose in TiO_2/NCC-EDA functions as a structural scaffold, electronic promoter, and surface modifier, demonstrating a clear advantage over non-cellulose-supported TiO_2 for visible-light-driven CO_2 photocatalysis [193].

Cellulose nanocrystals derived from the low-cost bamboo were used to develop a topologically chiral cellulose nanocrystals (CNC)@ZIF-8 3D network via Zn-N-S and Zn-O-S bond formation. This unique architecture not only enhances electron transport and reduces electron-hole recombination in ZIF-8 but also facilitates charge accumulation due to the larger bond angle and stronger electron-withdrawing nature of the Zn-O-S linkage. The CNCs@ZIF-8 photocatalyst achieved a CO yield of 301.16 μmol·g^{-1}, 9.43 times higher than that of pure ZIF-8. The higher content of CNC leads to greater optical rotation and UV sensitivity, showing a positive correlation between catalytic activity and topological chirality. The mechanistic studies (**Fig. 9 iiia**) revealed that the photogenerated electrons transferred to CNCs participate in forming superoxide radicals ($•O_2^-$), which further enhance the CO_2 reduction process. In the 3D chiral network OF CNCs@ZIF-8, adsorbed CO_2 molecules react with electrons and protons to form COOH• intermediates, which subsequently undergo protonation to yield CO [145].

In summary, novel cellulose-based hybrid composites (CNC@BOC) were synthesized via an innovative interfacial bonding strategy, demonstrating remarkable and consistent activity for CO_2 photoreduction under blue LED light, achieving a CO production rate of 15.22 μmol g^{-1} h^{-1} with 97% selectivity (**Fig. 9 iii** b-c). Theoretical calculations and experimental studies revealed that the hydroxyl groups on CNC interact with surface Bi ions of $Bi_2O_2CO_3$ (BOC), forming robust Bi–O–C covalent bonds. These interfacial bonds play multiple key roles in the catalytic system. First, the newly formed metal coordination polymer acts as a photosensitizer via ligand-to-metal charge transfer (LMCT), enhancing visible-light absorption and increasing the affinity of the catalyst toward CO_2 molecules. Second, the covalent linkage facilitates rapid electron transfer from BOC to CNC, generating highly oxidized Bi species and stabilizing oxygen vacancies (OVs) on the BOC surface, which are essential for CO_2 activation. Third, the integration of CNC and BOC establishes a type II heterostructure that promotes efficient separation of photoinduced charge

View Article Online
DOI: 10.1039/D5TA07511D

carriers, reduces electron-hole recombination, and enables facile formation of the key *COOH intermediate. Additionally, the covalent bonding, LMCT effect, and stabilized OVs collectively contribute to a narrowed bandgap, higher reactant adsorption, and accelerated charge transport pathways. These synergistic effects improve both photocatalytic activity and selectivity toward CO formation. [194].

The incorporation of cellulose and its derivatives as templates or supports in photocatalytic systems has emerged as a sustainable and versatile strategy to enhance CO_2 reduction performance (**Table 7**). Cellulose offers unique structural and chemical advantages, including high surface area, tunable functional groups, polar surfaces for CO_2 adsorption, and three-dimensional or chiral architectures, which collectively promote light harvesting, charge separation, and electron transfer. These features facilitate strong interactions between CO_2 molecules and the catalytic surface, improving adsorption, activation, and conversion efficiency. For instance, TiO_2 supported on aminated cellulose nanocrystals (NCC-EDA) achieves a CO_2 reduction rate of 372.85 μmol g^{-1} in 6 h, nearly seven times higher than the benchmark TiO_2 system (54 μmol g^{-1} cat^{-1}). Mechanistic studies indicate that covalent interfacial bonding between cellulose and the photocatalyst induces ligand-to-metal charge transfer (LMCT), narrows the bandgap, and generates highly reactive sites such as oxygen vacancies, thereby facilitating CO_2 activation and *COOH intermediate formation. Despite these advantages, several critical aspects remain underexplored: surface functionalization via amination, oxidation, or other modifications could further improve CO_2 adsorption and reactivity, but optimized protocols and their effects on electron transfer and reduction kinetics are not yet fully established. Similarly, the interactions of CO_2 with cellulose-supported reaction pathways.

Table 7 Summary of different photocatalysts employed for CO_2 reduction

Catalyst system	Light source	Non-cellulose benchmark performance	Cellulose-supported photocatalyst performance	Products	Reusability	Reference
TiO_2/nanocellulose crystals-EDA	300W Xe lamp	NCC-EDA: 54 μmol g^{-1} Cat^{-1}	372.85 μmol g^{-1} Cat^{-1}	CH_3OH, $HCOOCH_3$, $HCOOC_2H_5$, C_2H_5OH, and CH_2Cl_2	3	[193]
Cellulose nanocrystal bonded $Bi_2O_2CO_3$	3 W Blue LED lamp	$Bi_2O_2CO_3$: 0.26 μmol g^{-1} h^{-1}	15.22 μmol g^{-1} h^{-1} (CO)	CO, CH_4 and O_2	5	[194]
Cu modified GCN nanorod bundles	300W Xe lamp	g--C_3N_4: 4.16 μmol g^{-1} h^{-1}	49.57 μmol g^{-1} h^{-1} (CO)	CO, and CH_4	5	[195]
Cellulose nanocrystal ZIF-8 3D network aerogel	300W Xe lamp	ZIF-8: 31.94 μmol g^{-1}	136.37 μmol g^{-1} (CO)	CO	-	[145]

6.1.4 Nitrogen Fixation

Ammonia is a key industrial feedstock widely used in the production of fertilizers and chemicals [196]. Conventional synthesis through the Haber-Bosch process is energy-intensive and emits tons of carbon dioxide into the environment

View Article Online
DOI: 10.1039/D5TA07511D

[197]. As the demand for cleaner technologies grows, photocatalytic nitrogen fixation has emerged as a promising green alternative, utilizing solar energy to convert atmospheric nitrogen into ammonia under mild conditions using water as a proton source [198]. Wang et al. (2024) utilized cellulose as a sacrificial reagent for photocatalytic nitrogen fixation using oxygen-vacancy modified MoO_3 nanosheets. The MoO_3 samples exhibited photocatalytic activity for ammonia production using CH_3OH as a sacrificial agent, as confirmed by the Nessler's reagent method. The activity of the catalyst is closely associated with surface oxygen vacancies. Upon utilization of cellulose as an electron donor, the MoO_3-400 showed the highest NH_3 production (146 μmol $h^{-1}g^{-1}$). However, overall activity was lower than in the methanol system, likely due to cellulose's weaker reducing ability and limited charge-transfer pathways. The cellulose oxidation was primarily driven by hydroxyl radicals generated by the holes [199].

Balakrishnan et al. (2024) demonstrated that carboxymethyl cellulose (CMC), a cellulose derivative, plays a critical role in constructing citric acid-functionalized carbon nitride homojunction (ICN)/CMC hydrogel beads via a simple $FeCl_3$-assisted crosslinking strategy. The abundant hydroxyl and carboxyl groups of CMC facilitated strong hydrogen bonding and electrostatic interactions with ICN, ensuring uniform immobilization of ICN, enhanced water retention, and a higher surface area for nitrogen adsorption. This structural synergy significantly improved visible-light absorption, charge separation, and electron transfer, leading to efficient photocatalytic nitrogen fixation. Under visible-light irradiation with distilled water as the proton source, the ICN/CMC beads achieved a maximum ammonia yield of 501 μmol h^{-1} g^{-1}, which increased to 1168 μmol h^{-1} g^{-1} when methanol was used as a sacrificial agent, highlighting a more than twofold enhancement due to the sacrificial donor. For comparison, pristine g-C_3N_4 exhibited a much lower yield of 65 μmol h^{-1} g^{-1}, emphasizing the significant enhancement imparted by the ICN/CMC hybrid structure. In contrast, ICN without CMC exhibited lower activity and less effective charge separation, confirming that CMC not only acts as a structural scaffold but also contributes actively to the photocatalytic performance by facilitating proton transport and adsorption sites. Mechanistic studies revealed that the photoinduced electrons are efficiently transferred to adsorbed nitrogen molecules, reducing them to ammonium ions, while holes are effectively consumed, demonstrating that the CMC matrix enhances both the stability and activity of the photocatalyst. These results underscore the dual role of CMC as both a structural support and an electronic facilitator, providing a renewable, green scaffold that markedly improves nitrogen fixation efficiency [200].

In the photocatalytic system coupling nitrogen fixation with glucose conversion, cellulose serves as a critical substrate that is first enzymatically saccharified to glucose, which then donates electrons and protons during the photocatalytic reaction. The FIS/Fe-Pal composite, with a Fe-Pal to $FeIn_2S_4$ mass ratio of 0.4:1, achieved the highest ammonia production of 583 μmol g^{-1} after 6 h of visible-light irradiation surpassing $FeIn_2S_4$ (100 μmol g^{-1}). The cellulose-derived glucose acts as a sacrificial electron donor, facilitating rapid photogenerated charge separation in the S-scheme heterojunction between Fe-Pal and $FeIn_2S_4$. Sulfur vacancies and Fe ions on the FIS/Fe-Pal surface provide dual active sites for N_2 adsorption and activation, while the electrons derived from glucose oxidation reduce N_2 to NH_4^+. In comparison, in the absence of glucose, the same catalyst exhibits lower ammonia yield (314 μmol g^{-1}), underscoring the essential role of cellulose in enhancing photocatalytic nitrogen fixation. This highlights that cellulose not only

View Article Online
DOI: 10.1039/D5TA07511D

participates as a renewable sacrificial substrate but also improves electron transfer efficiency, thereby boosting NH_4^+ production in the coupled reaction system [201].

Across the reported nitrogen fixation systems, cellulose-supported catalysts consistently outperform their non-cellulose counterparts, exhibiting higher ammonia yields, improved charge separation, and enhanced stability. This highlights cellulose's dual role as both a structural scaffold and an electron/proton mediator, which is absent in conventional catalysts. However, challenges such as limited light absorption, catalyst stability, and scalability need to be addressed to advance practical applications: (i) The utilization of sustainable electron donors like cellulose and lignin derivatives offers eco-friendly alternatives to methanol or ethanol. (ii) Translating laboratory-scale findings into real-world applications requires the development of a scalable, continuous flow photoreactor system with optimized light distribution, and solar tracking technologies. (iii) Deeper mechanistic understanding using isotope labelling studies and DFT-based computational studies can elucidate reaction pathways, catalyst design, and enhance selectivity towards ammonia over by-products.

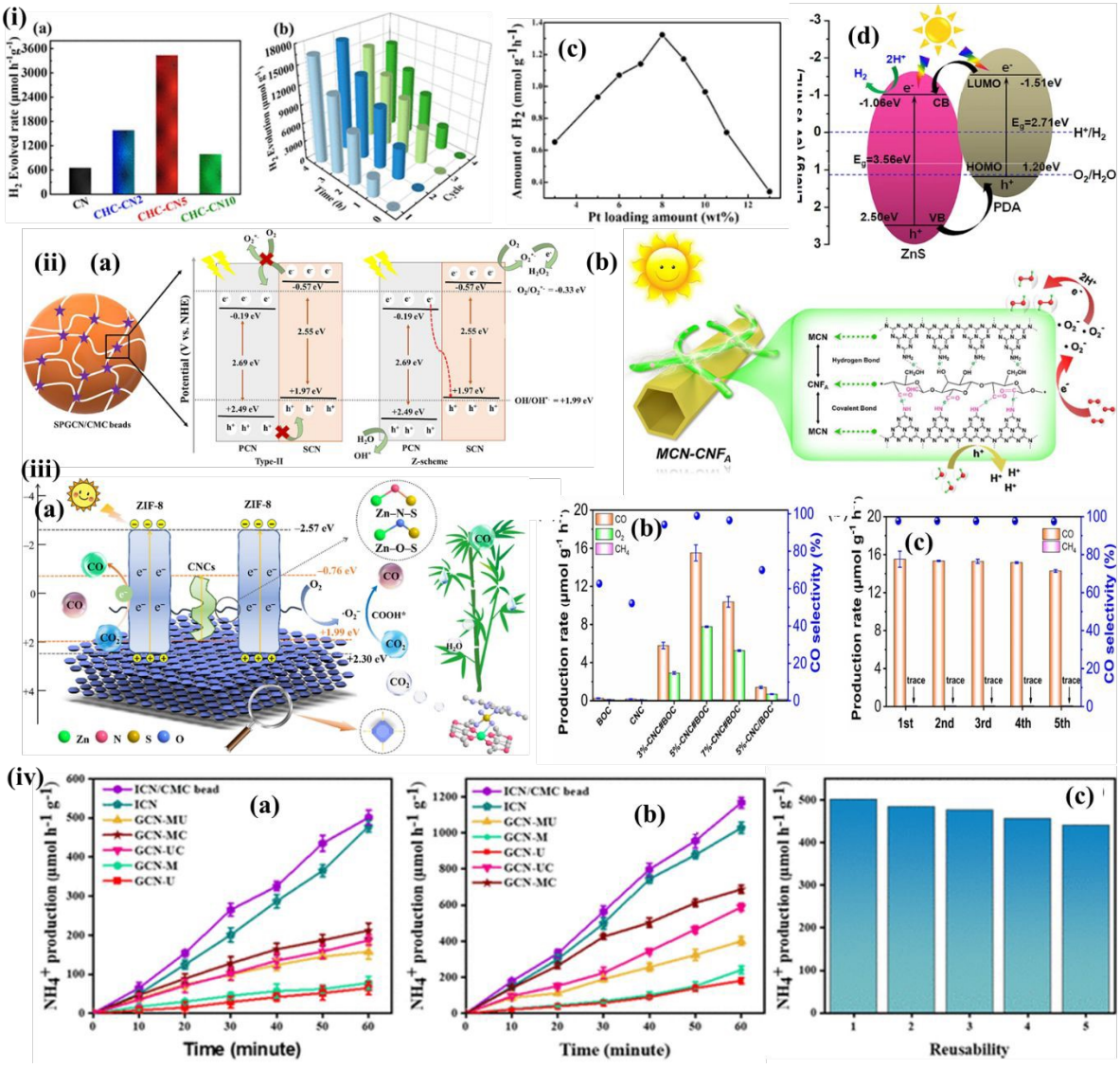

View Article Online
DOI: 10.1039/D5TA07511D

Fig. 9 (i) (a) Photocatalytic hydrogen evolution (b) Reusability of CHC-CN5 photocatalysts. Reprinted with permission from ref.[174], American Chemical Society, (2023). (c) Influence of platinum-loading amount on photocatalytic hydrogen evolution rate using CdS/RC-4.5 films. Reprinted with permission from Ref. [175], American Chemical Society (2009). (d) Band structures of ZnS and PDA charge transfer pathway in ZnS/PDA heterojunction. Reprinted with permission from [176], Springer (2024). (ii) (a) Proposed Z-scheme heterojunction mechanism for H_2O_2 production using SPGCN/CMC beads. Reprinted with permission from ref.[36], Elsevier (2024). (b) Mechanism of photocatalytic H_2O_2 production using MCN-CNF_A. Reprinted with permission from ref.[181], Elsevier (2024). (iii) (a) Mechanism of photocatalytic CO_2 reduction using CNCs@ZIF-8 3D network. Reprinted with permission from ref.[145], Elsevier (2024) (b) Photocatalytic CO_2 reduction performance of CNC@BOC, (c) Recovery experiments using the 5% CNC@BOC sample. Reprinted with permission from ref.[194], Elsevier (2024). (iv) Photocatalytic nitrogen fixation efficacy of ICN/CMC beads (a) Using water, (b) Using Sacrificial agents, (c) Reusability of ICN/CMC beads towards nitrogen fixation. Reprinted with permission from ref.[200], American Chemical Society, (2024).

A systematic strengths, weaknesses, opportunities, and threats (SWOT) analysis was conducted to provide a comparative evaluation of four major photocatalytic conversion processes: hydrogen production, hydrogen peroxide evolution, nitrogen fixation, and carbon dioxide reduction. **Fig. 10** presents the SWOT analysis of cellulose-supported photocatalysts for photocatalytic energy production. These solar-driven pathways are integral to the development of carbon-neutral energy systems and sustainable chemical manufacturing. Photocatalytic hydrogen production is relatively well-developed and benefits from its high energy density and clean combustion characteristics. Hydrogen peroxide synthesis offers a green alternative to the traditional anthraquinone process, operating under ambient conditions using water and oxygen as primary inputs. Photocatalytic nitrogen fixation, though less mature, holds promise as an energy-efficient and decentralized approach to ammonia production. Carbon dioxide reduction facilitates the conversion of greenhouse gases into valuable chemicals and fuels, aligning with the principles of a circular economy. The strengths of cellulose-supported photocatalytic systems include sustainability, mild operating conditions, and the ability to convert abundant, low-cost feedstocks into useful fuels. Weaknesses involve challenges such as charge recombination losses and material durability. Opportunities lie in the development of advanced cellulose-based composites and the integration of this technology into decentralized energy systems. Threats include competition from established energy technologies and the requirement for cost-effective, scalable production methods. Overall, continued research and innovation are essential to fully realize the potential of cellulose-supported photocatalysts in sustainable fuel generation.

View Article Online
DOI: 10.1039/D5TA07511D

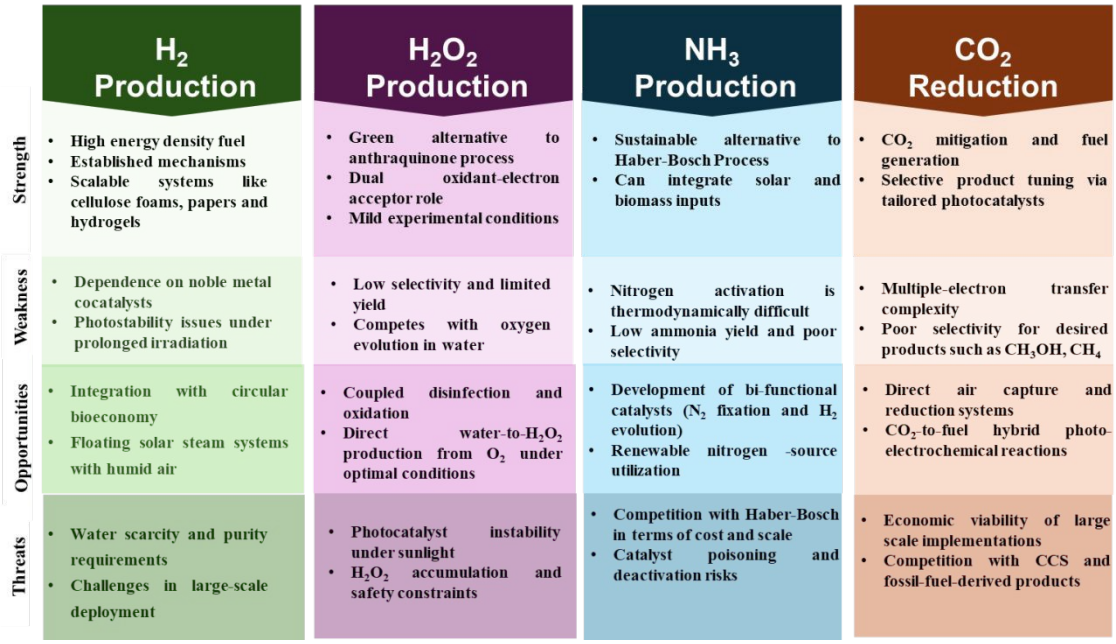

Fig. 10 SWOT analysis of cellulose-based photocatalysis for energy applications

6.2 Wastewater remediation

With significant advancements of industrialization, the environmental repercussions of human activities have become increasingly severe, raising widespread concern [8,202]. Among the most critical challenges is the protection of water resources, which has become a focal point in environmental research. Water pollutants typically include heavy metals, pharmaceuticals, dyes, and pesticides [203]. Among different methods, solar-driven photocatalysis stands out as a clean and sustainable method [204]. The cellulose-supported photocatalysts, leveraging cellulose's biodegradability, porosity, and structural stability [63]. This significantly enhances light absorption, charge separation, and overall photocatalytic performance, offering a promising pathway for efficient solar water purification [128]. **Fig. 11** explains the generalized degradation mechanism for aqueous pollutants using cellulose-based photocatalysts via photocatalysis, Fenton's process, and sulfate-based AOPs.

View Article Online
DOI: 10.1039/D5TA07511D

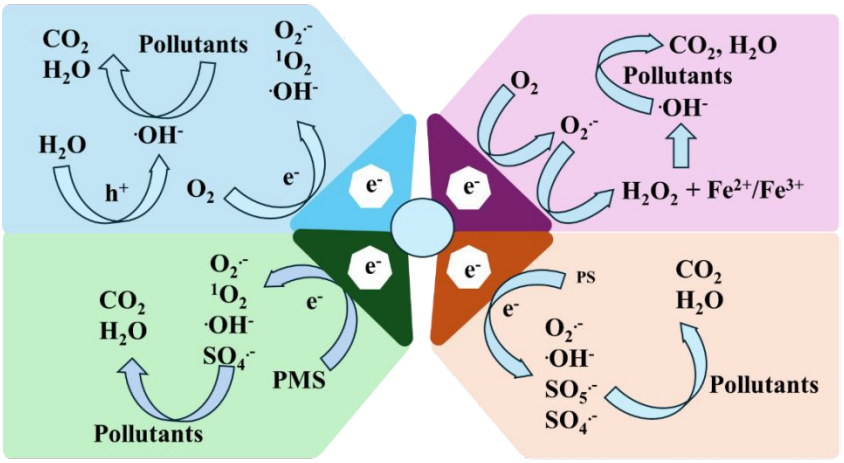

Fig. 11 Generalized wastewater degradation mechanisms using cellulose-based photocatalysts

Yan et al. (2024) emphasized the construction of a bamboo-based photocatalyst loaded with ZnO/WO_3 towards the redemption of organic dyes. The pretreatment of bamboo with NaOH facilitates the formation of active nucleation sites within the cellulose microchannels, which in turn promotes the uniform growth of the metal oxides. The ZnO/WO_3 was immobilized onto the pretreated bamboo via a hydrothermal strategy. The experimental studies claimed that the ZnO/WO_3/bamboo photocatalyst exhibited 93% dye degradation even after 20 consecutive cycles. The enhanced catalytic efficacy is ascribed to the synergistic interaction between ZnO and WO_3, which ensured the effective charge separation via a type-II pathway. The construction of heterojunctions promotes electron delocalization, enhancing hole migration from the valence band of ZnO to that of WO_3 and suppressing electron-hole recombination. The mechanistic studies revealed that ZnO–WO_3 forms a type II heterojunction, enabling effective separation of photogenerated charges. Under light irradiation, electrons in ZnO's conduction band transfer to WO_3, while holes in WO_3's valence band migrate to ZnO. This directional charge flow inhibits electron–hole recombination and facilitates redox reactions, including the reduction of W^{6+} to W^{5+}. It is also noted that the fibrous network and porosity of bamboo offer mechanical stability and abundant active sites, making it appealing as a scaffold for constructing heterojunctions towards the degradation of noxious pollutants [205]. Nitrogen- and boron-codoped carbon dots prepared through hydrothermal methods were embedded into a 3D porous aerogel matrix for photocatalysis. The Cd(II)-loaded aerogel was sulfurized and achieved a 95% efficiency against methylene blue (MB) degradation. Even after six reuse cycles, the photocatalyst maintained over 90% efficiency. The scavenger studies revealed that photogenerated holes (h^+), hydroxyl radicals (•OH), and superoxide radicals ($•O_2^-$) played key roles in the degradation mechanism, with $•O_2^-$ being the dominant reactive species [206].

Tian et al. (2024) developed an efficient 3D cellulose-TiO_2 through freeze drying forming a highly porous, tubular architecture. The photocatalytic studies confirmed 100% rhodamine B degradation even under low-light conditions in 4.5 hours. Even after 10 cycles of reuse, the removal efficiency declined by just 3% indicated phenomenal durability and reusability of the aerogel [207]. Jin et al. (2024) developed a composite composed of Mxene, ZnS, and chitosan-

View Article Online
DOI: 10.1039/D5TA07511D

cellulose for the efficient removal of anionic dyes through synergistic interaction between adsorption and photocatalytic degradation. The Mxene served as a cocatalyst, forming Schottky heterostructure with ZnS to enhance photocarrier separation and photocatalytic activity. The composite removed 100% of a 50 mg/L anionic dye solution, driven by electrostatic adsorption and photocatalytic generation of $\bullet O_2^-$, h^+, and •OH [208]. Ag-doped Cu_2O immobilized on cellulose-derived carbon beads was prepared via chemical reduction and in situ solid-phase precipitation reaction to obtain a highly porous interconnected structure. The Ag-doped Cu_2O immobilized on cellulose derived carbon beads exhibited 99% levofloxacin degradation, following pseudo-first-order kinetics. The improved efficacy is attributed to the presence of Ag, which benefits from enhanced charge carrier separation, while CBs act as electron reservoirs to improve the photocatalytic performance [209]. Sarkodie et al. (2024) employed flame spray pyrolysis to synthesize Bi_2O_3 nanoparticles, which were subsequently integrated with cellulose acetate (CA) polymer via electrospinning to fabricate a nanofiber membrane. The study revealed a strong interaction between CA and Bi_2O_3 nanoparticles, resulting in enhanced electron transport across the membrane surface, a reduced band gap, and suppressed recombination. The Bi_2O_3/CA nanofiber membrane exhibited a photocatalytic dye degradation efficiency of 95% within 90 minutes. The electron spin resonance and radical scavenger tests identified •OH as the primary reactive species responsible for the high photocatalytic activity [210]. **Table 8** summarizes different cellulose-based photocatalysts towards wastewater remediation.

The escalating environmental challenges posed by industrialization have intensified the urgency for effective water purification technologies. The integration of cellulose-based materials as supports for photocatalysts offers distinct advantages, including enhanced light absorption, improved charge separation, and mechanical stability, while also aligning with principles of biodegradability and environmental friendliness. The 3D cellulose-based catalysts exhibited phenomenal reusability and ease in catalyst recovery in hybrid forms. The following points must be focused on to establish an efficient photocatalytic system:

- Exploring bio-derived and renewable scaffolds to enhance the sustainability and scalability of photocatalytic materials while maintaining mechanical resilience and chemical stability.
- Developing multifunctional, integrated systems capable of simultaneous detection, adsorption, and photocatalytic degradation of emerging contaminants to address complex pollution scenarios.
- Addressing practical deployment challenges such as catalyst recovery, cost effectiveness, and long-term environmental impacts to facilitate real-world applications.
- Leveraging computational methods better to understand charge transfer mechanisms and reactive species dynamics, enabling rational design of next-generation photocatalysts with tailored functionalities.

Table 8 Review of different cellulose-based photocatalysts towards wastewater remediation

Catalyst	Light source	Pollutant	Initial concentration	Efficiency	Reusability	Reference

View Article Online
DOI: 10.1039/D5TA07511D

TiO_2-cellulose (mandarin peels) based nanocomposite	UV lamp (254 nm)	Methyl orange	100	98.87% in 30 min	6	[211]
Ag/N-TiO_2 Aerogel	500 W Xe lamp	Methylene Blue	10	100% in 120 min	-	[212]
CdS nanoparticles anchored on cotton short-based carbon aerogels	Visible light	Methylene Blue	15	95% in 90 min	5	[213]
Cellulose nanocrystals-TiO_2	Sunlight	Azithromycin	10	98% in 300 min	-	[214]
Au-TiO_2 bacterial cellulose aerogel	150W UV lamp	Methylene Blue	1.28	89% in 360 min	5	[215]
ZnO/SnO_2/Carbon xerogel	300 X Vitalux	Methylene Blue	25	88% in 300 min	3	[216]
Carbon dots loaded cellulose nanofibrils hydrogels incorporated Bi_2O_3/BiCOOH	500 W Hg lamp	Lignin	100	93% in 180 min	10	[217]
$BiVO_4$ lignocellulosic	250 W UV lamp	Rhodamine B	10	90% in 120 min	7	[218]
Cellulose modified Cu-Al double hydroxide composite	50 W LED lamp	Doxycycline	40	100% in 120 min	4	[219]
Cu_2O/Ag_2MoO_4 nanofibers on cellulose fibers	250 W Xe lamp	Reactive Blue 19	25	98% in 150 min	5	[220]
TiO_2 using nanocrystal cellulose	300 W Xe lamp	Phenol	0.01	97.4% in 60 min	6	[221]
Cellulose acetate membrane doped with Ag-rGO nanocomposites	250 W Hg lamp	Rhodamine B	20	97% in 60 min	4	[222]
Cellulose-chitosan/β-FeOOH hydrogel	100 W Xe lamp	Methyl orange	40	97% in 40 min	5	[223]
Polydopamine-bacterial cellulose/GCN	100 W LED lamp	Methylene Blue	10	95% in 150 min	3	[224]
Cellulose composite membrane decorated with Prussian blue analogue	300 W Xe lamp	Tetracycline	10	90%	5	[225]
Cellulose-chitosan-Ag/Ag_2O/ZnO	UV light (253 nm)	Methyl Orange	10	97% in 50 min	3	[226]

View Article Online
DOI: 10.1039/D5TA07511D

Titania loaded cellulose functional hybrid material.	UV-C lamp	Methylene Blue	50	98.5% in 40 min	5	[227]
$H_3PW_{12}O_{40}$ /Fe_3O_4 nanocomposite with cellulose scaffolds	300 W Hg lamp	Methylene Blue	10	95% in 5 min	15	[228]
Ag_3PO_4/nanocellulose composite	Sunlight	Methylene Orange	-	90% in 80 min	-	[229]

6.2.1 Photo-Fenton process

Recent advancements in cellulose-based composite photocatalysts have significantly improved the efficiency, stability, and sustainability of photo-Fenton processes for wastewater treatment. By integrating metal or metal oxide catalysts such as Fe, Cu, TiO_2, and Fe_3O_4 into cellulose matrices, hydrogels, or membranes. These multifunctional systems have enhanced visible-light activity, broader pH applicability, and excellent reusability. These innovative materials present environmentally friendly and cost-effective solutions for the degradation of noxious compounds in wastewater. For instance, Fe-complex incorporated into a cellulose acetate (CA) membrane via tape casting has demonstrated promising visible-light-driven photocatalytic performance. Under visible light and low H_2O_2 concentrations, the Fe-complex/CA membrane efficiently degraded basic fuchsin (100%), methylene blue (93.4%), and sulfadiazine (95.7%) within 60 minutes. The system followed first-order kinetics and retained catalytic efficiency over four cycles [230].

Xu et al. (2023) emphasized a heterojunction photocatalyst, $BiYO_3$/g-C_3N_4, which was successfully prepared for the efficient reclamation of tetracycline under visible light irradiation. Later, $BiYO_3$/g-C_3N_4 composite was further immobilized on carbon nanofibers via an electrostatic self-assembly method, resulting in $BiYO_3$/GCN/cellulose nanofibers with a fluffy, and porous structure. This structure enhanced visible light absorption and facilitated rapid separation and transfer of photoinduced electron-hole pairs (**Fig. 12a**). The synergistic combination of adsorption and photocatalysis enabled by the cellulose nanofiber led to phenomenal tetracycline degradation. The composite maintained approximately 90% of its initial photocatalytic performance after five reuse cycles, demonstrating good stability and reusability [137]. A sustainable Fe^0@CS/CF hybrid catalyst, synthesized via eco-friendly methods, has shown high efficiency in the photo-Fenton degradation of levofloxacin (LVX). The photocatalytic studies reported that a complete degradation of 25 mg L^{-1} LVX was achieved within 40 minutes under neutral pH (7.0), with a catalyst dosage of 0.5 g L^{-1} and 0.5 mL H_2O_2. The enhanced catalytic activity is attributed to the synergistic interactions among chitosan, cellulose fibers (CF), and their composite support, which improve surface area, adsorption capacity, and interfacial contact with Fe^0. The Fe^0@CS/CF-mediated photo-Fenton degradation of LVX operates via a synergistic mechanism involving visible-light-induced photocatalysis and Fenton oxidation, where photoexcited electron–hole pairs generate reactive oxygen species (•OH and O_2•$^-$) that initiate and sustain the degradation process (**Fig. 12 b**). The adsorption of LVX onto the catalyst surface, photolysis of H_2O_2, and cyclic redox conversion between Fe^{2+}/Fe^{3+}

View Article Online
DOI: 10.1039/D5TA07511D

boosted the radical generation and contributed to the degradation of LVX. The mechanistic analysis indicates that hydroxyl radicals drive a multi-step oxidative pathway involving hydroxylation, demethylation, decarboxylation, and quinolone ring cleavage, aiding LVX reclamation [231].

A recent study reported the development of a cellulose-based nanocomposite hydrogel incorporating TiO_2 and Fe_3O_4 as dual catalysts, synthesized via] situ synthesis and mineralization. Here, TiO_2 was found to modulate the hydrogen bonding network, contributing to faster gelation, reduced pore size, and improved mechanical strength. Meanwhile, Fe_3O_4 imparted magnetic properties by anchoring onto cellulose chains. This dual-functional hydrogel demonstrated enhanced photocatalytic activity in the photo-Fenton process, achieving up to 97.5% removal of methylene blue within 60 minutes. Notably, the system maintained high degradation efficiency across a pH range of 4-7 and exhibited excellent stability over five reuse cycles without significant pollutant leakage [232]. Li et al. (2022) emphasized that the in-situ co-precipitation was employed to fabricate PVA/CNF/Fe_3O_4 hybrid hydrogels, wherein Fe_3O_4 nanoparticles are uniformly dispersed within a polyvinyl alcohol (PVA) and cellulose nanofiber (CNF) matrix. The hydrogel not only provides structural stability and magnetic recoverability but also facilitates enhanced Fe^{2+}/Fe^{3+} redox cycling under light irradiation. When applied as a photo-Fenton catalyst, the system effectively activated H_2O_2 to generate reactive •OH radicals, enabling efficient degradation of tetracycline. Under optimal conditions (pH 3, 100 mM H_2O_2, 0.3 g L^{-1} catalyst, 25 °C), the hybrid hydrogel achieved 98% removal within 120 minutes, following pseudo-first-order kinetics [233].

A Co_3O_4@Fe_3O_4/cellulose membrane, prepared by integrating Co_3O_4-coated MOF-derived Fe_3O_4 with a cellulose matrix, was applied in a visible-light-driven photo-Fenton system for PFOA degradation. The EPR and scavenger studies revealed a synergistic mechanism involving photogenerated electrons, holes, and multiple radical species. The membrane achieved 94.5% PFOA removal within 180 minutes, with minimal metal leaching (Fe: 0.05 ppm, Co: 0.49 ppm), and retained 80.4% efficiency after five cycles [234]. To enhance both catalytic performance and recyclability, a cellulose-derived carbon-supported Cu–Fe composite (MA-Cu-Fe@C) was synthesized via mechanical activation of precursors followed by one-step calcination. The mechanical activation promoted the formation of abundant active sites, strong Cu–Fe interactions, and uniform embedding within the carbon matrix, enabling synergistic enhancement in a photo-Fenton system. The catalyst demonstrated high activity across pH 3–9, achieving 98.8% methylene blue degradation and 73.7% TOC removal. Remarkably, it retained over 96% degradation efficiency after 20 reuse cycles, highlighting excellent stability and reusability [235].

The developments of cellulose-based photocatalysts have marked a significant step towards sustainable and efficient wastewater remediation (**Table 9**). By combining the structural versatility and biodegradability of cellulose with the redox activity of metal or metal oxide components, these materials offer enhanced photocatalytic performance, broader pH operating ranges, and excellent reusability. However, challenges remain in terms of scalability, affordability, and the fundamental understanding of mechanisms under dynamic environmental conditions. Addressing these aspects will be essential to transition from lab-scale innovation to practical deployment.

View Article Online
DOI: 10.1039/D5TA07511D

- Utilization of natural sunlight as the effective light source to reduce the energy dependence of the proposed technology
- Employment of in-situ characterization techniques to unravel radical generation pathways and pollutant degradation mechanisms.
- Development of multifunctional designs that integrate additional capabilities such as antimicrobial activity, pollutant sensing, or self-healing characteristics.
- Prioritize sustainable synthesis using bio-based precursors and solvent-free processes for the preparation of cellulose-based photocatalysts.

Table 9 Summary of different cellulose-based catalysts employed for the photo-Fenton system

Catalyst	**Pollutant**	**Initial concentration mg L^{-1}**	**Efficiency**	**Reusability**	**Reference**
Co, Fe-bimetallic MIL-88A/MCC composites	Rhodamine B	5	87% in 100 min	5	[236]
CMC assisted litchi-like zinc ferrite	Tetracycline	0.04 mM	80% in 18 min	4	[237]
CuS@carbon nanocomposites	2,4-DCP	25	90% in 150 min	5	[238]
Magnetite nanoparticles decorated cellulose aerogel	p-nitrophenol	2000	92% in 60 min	5	[239]
Fe(II) crosslinked alginate CMC beads	Malachite Green	10	98% in 30 min	-	[240]
Polydopamine-coated carbonized cotton fabrics with β-FeOOH nanorods	Methylene Blue	50	80% in 70 min	6	[241]
Wood converted porous carbon decorated with MIL-101(Fe)	Ciprofloxacin	10	99% in 120 min	5	[242]
Lignin-based electrospun nanofiber membrane decorated with photo-Fenton Ag@MIL-100(Fe)	Methylene Blue		99% in 30 min	-	[243]
Durian fiber loaded with FeOOH nanoparticles	Tetracycline	5	96% in 100 min	-	[244]

View Article Online
DOI: 10.1039/D5TA07511D

Cu-Fe/Wood converted porous carbon	Methylene blue Sulfamethoxazole	10	100% in 5 min	5	[245]
Fe_3O_4 -starch-derived carbon	Tetracycline	5 mM	98% in 35 min	5	[246]
MOF-on-MOF-derived Fe-Zr bimetal oxides supported on hierarchically porous carbon	Ciprofloxacin	20	99% in 120 min	5	[247]
Red mud supported on rice husk biochar	Ciprofloxacin	20	95% in 120 min	-	[248]

6.2.2 Sulfate-based AOPs

Advanced oxidation processes (AOPs) have gained prominence as an effective strategy for removing persistent organic pollutants (POPs) from water, owing to their capability to generate abundant and highly reactive oxygen species (ROS) that drive rapid contaminant degradation.. Among these, hydroxyl radicals (E^0=2.8V) and sulfate radicals (E^0=2.5-3.1 V) are particularly notable for their oxidative strength and broad-spectrum reactivity [249]. In comparison with traditional AOPs, sulfate-based AOPs have gained substantial attention due to their higher redox potential, longer half-life, and superior reactivity towards a wide range of pollutants [94]. Peroxymonosulfate (PMS) and persulfate (PS) are commonly used oxidants for sulfate radicals' generation, activated via thermal, chemical, photolytic, or catalytic pathways [250]. Despite its strong oxidative potential, sulfate-based AOPs often fail to fully mineralize pollutants, necessitating the integration of catalytic systems for enhanced activation [251]. These hybrid catalysts enable dual PMS activation via both radical and non-radical pathways, achieving rapid and selective degradation of pollutants.

Tian et al. (2025) explored an integrated approach for fabricating a cellulose based electrospun photocatalytic membrane via synchronous electrospinning of cellulose acetate and electrospraying of core-shell PMMA@PDA@ZIF-67 heterojunction. The catalytic membrane exhibited degradation against tetracycline (93%) and methylene blue (99%) through PMS activation under visible light. The improved efficacy is ascribed to the enhanced light absorption, charge separation, while the electrospun architecture ensured uniform catalyst distribution and reusability. The synergistic action of light and PMS, a case of reactive species such as singlet oxygen assisted non-radical pathway facilitated rapid abatement of micropollutants as shown in **Fig. 12 c** [252]. Ren et al. (2018) described that the zeolitic imidazole framework (ZIF) materials such as ZIF-9 and ZIF-12 were immobilized on cellulose aerogels to fabricate hybrid aerogels, which acted as efficient activator towards PMS activation. The hybrid catalytic systems demonstrated a superior catalytic activity towards the reclamation of Rhodamine B, tetracycline and p-nitrophenol. The mechanistic studies using EPR analysis and radical quenching techniques affirmed that the PMS

View Article Online
DOI: 10.1039/D5TA07511D

activation by the hybrid aerogels generated both $SO_4\bullet^-$ and •OH, with $SO_4\bullet^-$ identified as the dominant reactive species [253].

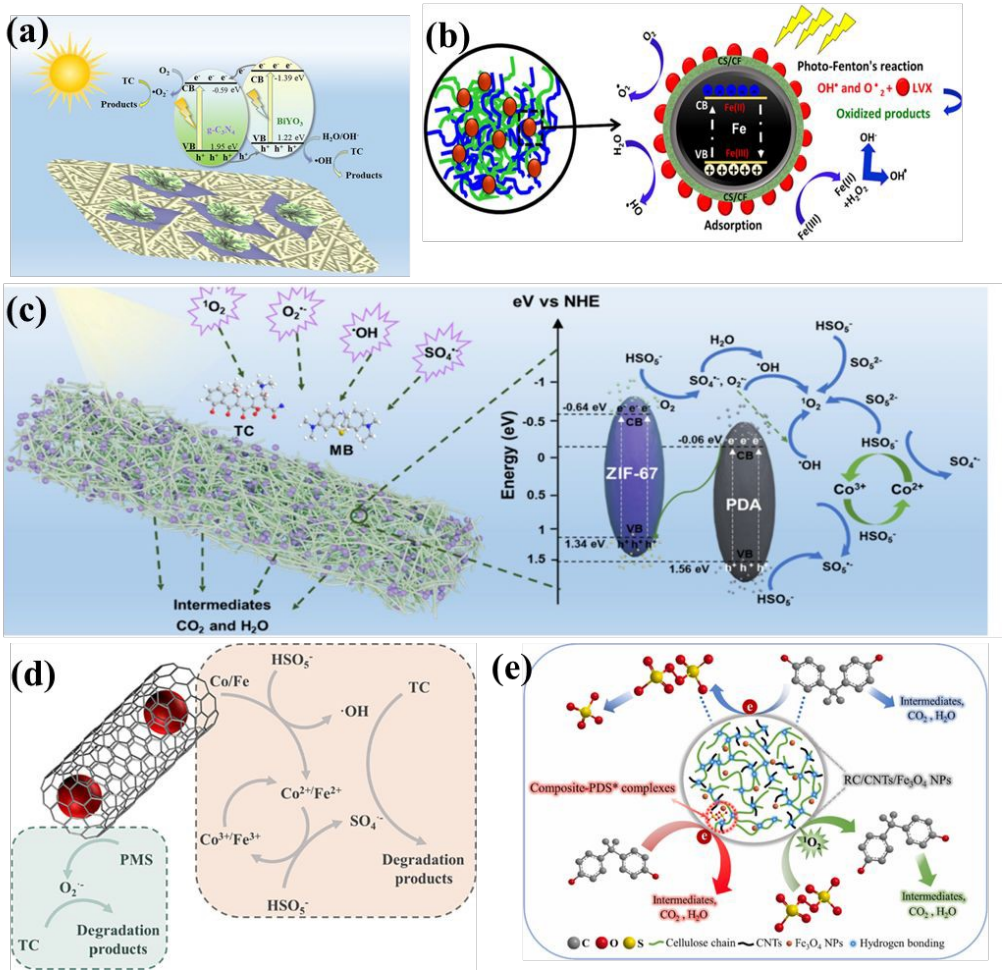

Fig. 12 (a) Diagrammatic representation of tetracycline degradation using GCN/$BiYO_4$ via photocatalysis. Reprinted with permission from ref. [137], Elsevier (2023). (b) Photo-Fenton assisted degradation mechanism of LVX. Using Fe0@chitosan/Cellulose green hybrid structures. Reprinted with permission from ref. [202], Elsevier (2024), (c) Degradation mechanism of tetracycline using PMS system. Reprinted with permission from [252], Elsevier (2025). (d) Schematic illustration of proposed tetracycline degradation using catalytic system. Reprinted with permission from ref. [254], Elsevier (2022). (e) Diagrammatic representation of bisphenol-A degradation using RC/CNTs/Fe_3O_4 nanoparticles. Reprinted with permission from [255].

Han et al. (2022) explained the diclofenac degradation using wood pulp cellulose biochar/GCN composite via PMS activation. The experimental studies reported complete degradation of diclofenac in 25 minutes with a reusability of 5 cycles. The integration of waste pine biochar with GCN significantly enhanced visible light absorption, improved charge separation, reduced electrical resistance, and boosted both photocatalytic activity and PMS activation. The key reactive species such as •OH, h^+, and $\bullet O_2^-$ were implicated in the radical mechanism, while $^1O_2$ and direct electron

View Article Online
DOI: 10.1039/D5TA07511D

transfer dominated the nonradical degradation pathway [256]. Similarly, Nitrogen doped carbon catalysts were synthesized using waste cotton fibers with four distinct crystalline structures as carbon sources via carbonization process towards the degradation of Reactive Blue 19. The results indicated that within 40 min, the degradation efficiency of nitrogen doped carbon catalysts against the Reactive Blue 19 reached 99% with a reusability of 4 cycles. The scavenger analysis claimed the superior role of $^1O_2$ as the main ROS and involved in non-radical based electron transfer mediated dye degradation [257]. Gan et al. (2019) described that the carbon nanofibers derived from cellulose were employed for the support to enhance the catalytic performance of $CoFe_2O_4$ for PMS activation. The carbon nanofibers/$CoFe_2O_4$ nanocomposites demonstrated high efficiency in degrading dimethyl phthalate, a model organic pollutant in aqueous media. The phenomenal degradation is indicated to the presence of carbon nanofiber which enhanced the potential of cobalt ferrite by reducing the prone towards agglomeration and enhanced the electron transfer. The spinel structured $CoFe_2O_4$ imparted magnetic separability, enabling easy recovery, and reusability of 5 cycles [258].

In another study, $CoFe_{0.8}$@NCNT@CA composite, wherein carbon nanotubes (NCNTs) derived from a Co-Fe bimetallic MOFs are uniformly loaded onto a cellulose aerogel matrix. The hybrid material has demonstrated remarkable catalytic activity for the activation of PMS achieving a tetracycline degradation pathway of 97% in 20 min. The high performance is attributed to the synergistic interplay between the bimetallic active centers, graphitic nitrogen functionalities, and the hierarchical porous structure of the aerogel. Notably, the unique semi-coated architecture formed between the carbon nanotubes, and the cellulose scaffold enhances CNT adhesion and stability, exposes abundant catalytic sites, and facilitates efficient mass transport factors that are crucial higher rate degradation in aqueous environment. The mechanistic investigations reveal that the $CoFe_{0.8}$@NCNT@CA/PMS system operates through a combination of direct electron transfer and radical-mediated pathways (**Fig. 12 d)** [254]. Dong et al. (2022) explained the development of magnetic and porous regenerated cellulose/carbon nanotubes (CNTs)/Fe_3O_4 nanoparticle composites were synthesized in a green alkaline-urea medium and applied for peroxydisulfate activation to degrade bisphenol A (BPA). The regenerated cellulose/carbon nanotubes (CNTs)/Fe_3O_4 nanoparticle composites achieved complete 100% removal of bisphenol-A. This enhanced performance was attributed to defect sites, nitrogen doping, functional groups, and the formation of a conductive network. The mechanistic studies revealed a dominant non-radical mediated degradation pathway as shown in **Fig. 12e** [255].

Cellulose-based photocatalytic-PMS/PS systems have demonstrated significant promise for the efficient degradation of POP's in aqueous environment (**Table 10**). The integration of cellulose with photocatalysts has led to the development of highly efficient hybrid catalysts with charge carrier dynamics, surface area, light utilization, and pollutant adsorption. These systems not only leverage radical mechanisms but also exploit non-radical pathways, especially $^1O_2$ and direct electron transfer, which are gaining attention due to their selective and less toxic degradation routes. The dual or synergistic activation using light and PMS/PS opens new avenues for effective pollutant abatement. However, future research may focus on (i) Rational design of cellulose derived frameworks with precisely controlled pore structures, surface functionalities and hierarchical architectures will enhance pollutant-catalyst interaction and activation efficiency. (ii) With increasing environmental concerns regarding metal leaching, there is a growing interest

View Article Online
DOI: 10.1039/D5TA07511D

in developing robust, metal free-cellulose supported catalysts for water treatment applications. Translating lab-scale efficiency of pilot and industrial scale systems requires efforts in reactor design, membrane modularization, and continuous flow operations.

Table 10 Summary of different cellulose-based photocatalysts employed for sulfate-based AOPs

Catalyst	Pollutant	Initial concentration	Efficiency	Reusability	Reference
S-doped cellulose nanocrystals with edge sulfur vacancies	Ciprofloxacin	40	100% in 25 min	5	[259]
CuS hollow nanospheres@N-doped Cellulose nanocrystal composites	Ciprofloxacin	20	99.5% in 180 min	-	[260]
Fe-MOF (MIL-101-Fe) derived porous carbon material	Sulfadiazine	20	100% in 15 min	3	[261]
Co-ZIF@cellulose aerogels	p-nitrophenol	10	98% in 70 min	3	[262]
MOF/bacterial cellulose derived octahedral MnO/carbon nanofiber	Tetracycline	50	90% in 30 min	5	[263]
Amphoteric CMC/sodium alginate/polyethyleneimine/ZIF-67	Rhodamine B	20	100% in 120 min	5	[264]
ZIF-67/MXene/carbon nanofiber aerogels	Tetrabromobisphenol-A	40	99% in 40 min	5	[265]
Cellulose@carbon nitride@ZIF-67	Nofloxacin	50	99% in 60 min	7	[266]
Fe doped black phosphorous carbonized cotton fiber	Tetracycline	10	95% in 150 min	-	[267]
	Congo Red	40	98% in 60 min	7	
	Methylene blue	5	99% in 60 min	-	
ZIF-67/cellulose membrane	Methylene blue	10	100% in 1min	4	[268]
	Rhodamine B			-	

Photocatalytic wastewater remediation offers a sustainable and energy efficient approach to degrade noxious contaminants using efficient photocatalysts. The integration of cellulose as a support material not only enhances pollutant adsorption and catalyst dispersion but also promotes effective charge separation by acting as an electron mediator, thereby enhancing photocatalytic efficiency. This green strategy aligns with environmental goals due to its low toxicity, biodegradability, and ability to operate under mild conditions. A SWOT analysis reveals strong potential due to its renewable energy basis and environmental compatibility, though limitations such as narrow light absorption and scalability must be addressed (**Fig. 13**). The future opportunities lie in engineering multifunctional cellulose-based

View Article Online
DOI: 10.1039/D5TA07511D

hybrid materials with enhanced light absorption, pollutant selectivity, and reusability as well as in deploying decentralized treatment units for remote areas. However, challenges such as ensuring cost-effectiveness, long term operational stability, and competing with well-established conventional treatment technologies remains critical barriers to widespread adoption.

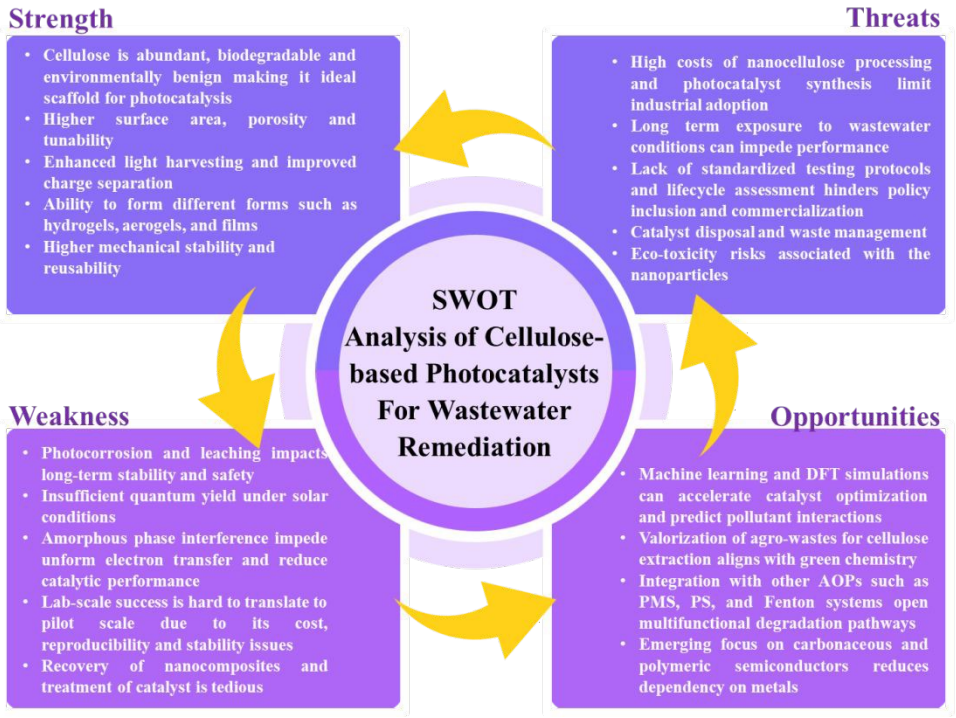

Fig. 13 SWOT analysis of cellulose-based photocatalysts for wastewater remediation including photocatalysis, photo-Fenton's, and sulfate-based AOP's

6.3 Disinfection

The proliferation of pathogenic microorganisms in water environment poses critical health hazards, contributing towards the outbreaks of infectious diseases and ecological imbalance [4]. Compared to conventional antimicrobial methods often fall short due to poor efficacy, secondary pollution, and microbial resistance. In the context, photocatalytic disinfection has garnered growing attention as a sustainable alternative in environmental applications [269]. The engineered cellulose-photocatalysts exposed to visible light generates the highly active charge carriers that initiate oxidative degradation pathways. These photoinduced ROS species such as •OH and $\bullet O_2^-$ are potent enough to disrupt the microbial membranes damaging intercellular components, and leading to cell death [270]. Cellulose, owing to its high surface area, porosity, and abundant -OH provides an excellent scaffold for uniform catalyst dispersion and improved light-catalyst interaction. Maslana et al. (2022) developed a scalable cellulose-based substrate functionalized with exfoliated GCN and silver nanoparticles demonstrated effective self-cleaning and antimicrobial activities. The composite exhibited 100% inactivation of *E. Coli* and *S. Aureus* within 2 hours under light and 24 hours under dark

View Article Online
DOI: 10.1039/D5TA07511D

conditions. The material exhibited strong potential for antimicrobial surfaces, however concerns such as nanoparticle leaching, long-term stability, and reusability must be addressed [271].

CMC-based hydrogels offer a renewable and biocompatible platforms for supporting sunlight-responsive photocatalysts; however, their dense matrix often induces a light shielding effect that hampers disinfection efficacy. To overcome this, Wang et al. (2025) utilized polydopamine has been introduced as an interfacial mediator, leveraging its quinhydrone charge-transfer ability to facilitate electron transport between the embedded catalysts. A double network CMC/PDA gel, formed via chemical crosslinking and hydrogen bonding, enables the in-situ formation of Ag/AgCl/ZnO heterojunction with greater catalytic activity. The composite gel achieved almost complete bactericidal activity under sunlight, with inhibition zone larger under irradiation than in the dark conditions, highlighting its light dependent efficacy [272]. A TiO_2NPs@CMC hydrogel was developed by incorporating hydrothermally synthesized TiO_2 nanoparticles into a carboxymethyl cellulose (CMC) matrix, followed by $CaCl_2$ crosslinking. The hydrogel exhibited strong antimicrobial and antibiofilm activity against key waterborne pathogens, including *S. typhi*, *E. coli* O157, *Shigella dysenteriae*, and *B. cereus*, with inhibition zones up to 29 mm. At 100 μg mL^{-1}, it significantly reduced bacterial counts, achieving complete pathogen inactivation in sewage within 180 minutes [273]. Huang et al. (2023) developed photocatalytic hydrogel by in situ immobilization of ZnO and/or Ag/AgCl nanoparticles, with epichlorohydrin serving as a crosslinker and Cl source for AgCl deposition. The resulting nanocomposite gels exhibited pH-responsive swelling and enhanced Zn^{2+} release under acidic conditions. Ag/AgCl-loaded gels demonstrated superior antibacterial performance against *E. coli* and *S. aureus* under 6 h of sunlight, significantly outperforming dark conditions. The materials showed no cytotoxicity below 0.33 mg mL^{-1} and maintained structural stability [274].

Bacterial cellulose (BC) derived from *Acetobacter xylinum* served as a robust 3D scaffold for in-situ synthesis of TiO_2 nanoparticles. The BC/N-F-TiO_2 composite exhibited superior catalytic disinfection performance under visible light, effectively targeting both gram negative and gram-positive bacteria. It is also noticed that antibacterial activity is influenced by both bacterial type and the doping level, indicating the need for precise compositional tuning [275]. In another study, Shen et al. (2022) reported one-step biosynthetic approach to immobilize into BC to yield MoS_2/BC composites, demonstrated synergistic photodynamic and photothermal activity. In the presence of H_2O_2, BC/MoS_2 generated hydroxyl radicals (•OH) and achieved >99% (6-log) reduction of *E. coli* and *S. aureus* under near-infrared (NIR) light (100 W, 760–5000 nm) within 5 minutes. The mechanistic insights highlighted the dual action of ROS-mediated oxidative stress and MoS_2-induced hyperthermia as the key contributor towards disinfection efficacy [276]. A GO–TiO_2 nanohybrid was integrated into bacterial cellulose (BC) to form a porous, photocatalytically active composite. TiO_2 nanoparticles (10–30 nm) with mixed anatase–rutile phases were uniformly anchored on GO sheets, maintaining strong ROS generation under near-UV light. The GO–TiO_2/BC composite showed effective antibacterial activity against *S. aureus* upon irradiation, with no dark cytotoxicity observed. The hybrid leveraged GO's charge transport and TiO_2's reactivity, while BC provided structural support. Though promising for antimicrobial and photocatalytic applications, its UV-dependence and oxidative stress risks require further evaluation [277].

View Article Online
DOI: 10.1039/D5TA07511D

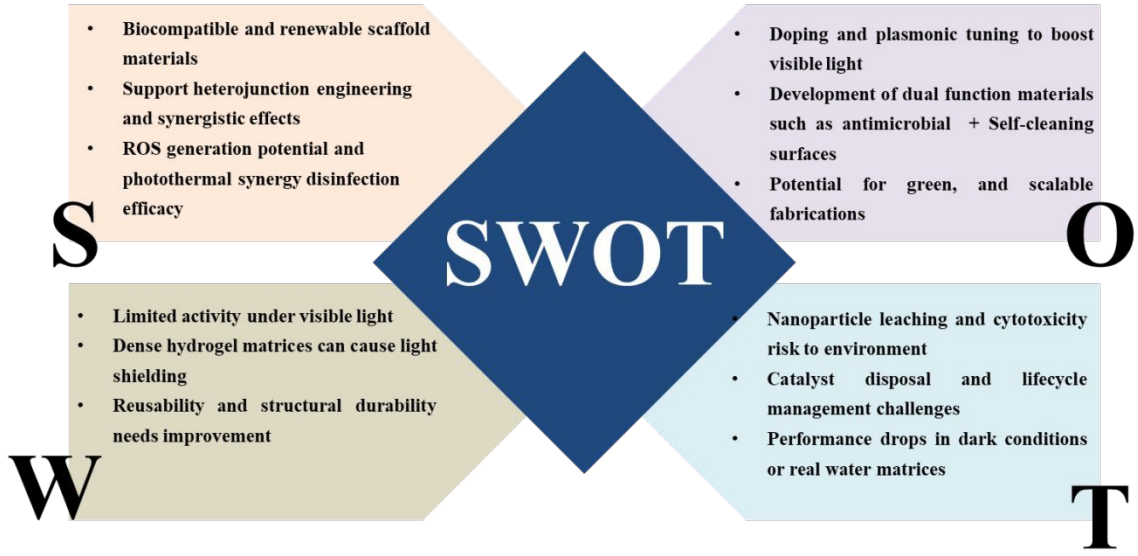

Fig. 14 SWOT analysis for cellulose-based photocatalysis towards disinfection

Cellulose-supported photocatalysts particularly those based on CMC and bacterial cellulose offer a sustainable, biocompatible platform for light-assisted disinfection. The integration of photocatalysts into these matrices has enabled efficient antimicrobial action through ROS production, photothermal effect and heterojunction engineering. These systems demonstrated broad spectrum pathogen inactivation including bacterial and viral surrogates, with strong performance under sunlight or UV irradiation. However, key challenges like nanoparticle leaching, limited visible light responsiveness, long term stability, and environmental safety remains unsolved. Thus, future efforts should focus on (i) Enhancing visible -light activity via doping and plasmonic effects, (ii) Ensuring reusability and structural durability, (iii) Minimizing toxicity through safe-by-design nanostructures. **Fig. 14** discuss the SWOT analysis for cellulose-based photocatalysis towards disinfection. With these advancements, cellulose-based photocatalytic materials hold strong potential for real-world applications in water purification, antimicrobial surfaces and public health protection.

7. Environmental and economic analysis

The environmental impact of cellulose-based composites is mainly concentrated during their production and uses phases (**Fig. 15**). The cellulose is sourced from renewable plant biomass such as agricultural residues and wood pulp, obtained through eco-friendly and cost-effective processes that minimize ecological harm [256,278]. In contrast, conventional materials like petroleum-based plastics, metals, and synthetic rubbers come from finite mineral reserves whose extraction and refining are resource intensive. For example, fossil-based plastics can produce 1.6–6.4 kg CO_2-eq per kg over their life cycle [279]. Meanwhile, bio-derived cellulose materials such as nanofibrils have reported life-cycle carbon footprints ranging from −1.6 to +12.2 kg CO_2-eq per kg, depending on the synthesis route and how biogenic carbon is handled [280]. The fabrication of cellulose composites is generally simpler and potentially more environmentally benign. For example, advanced nanocellulose production processes, especially those using hybrid mechanical + enzymatic treatments, show significantly lower environmental burdens. Life-cycle inventory studies

View Article Online
DOI: 10.1039/D5TA07511D

report cumulative energy demands in the range of a few MJ per kg for certain optimized CNF production routes, and pretreatment wastewater volumes of 0.44–1.6 L per 10 g of nanofibrils [281,282]. These numbers underscore how emerging process designs can minimize resource consumption compared with more energy- and chemically-intensive manufacturing routes.

Cellulose-based composites also offer strong biodegradability, preventing long-term environmental accumulation [283]. For instance, carboxymethyl cellulose (CMC) shows quantifiable biodegradation in activated-sludge systems: OECD 301B tests report 41–46.7% mineralization by day 28 and 55.2–63.7% by day 70. Under higher inoculum conditions, degradation accelerates to >60% DOC removal within 15 days. OECD 314B studies further show >60% mineralization in just 6 hours, with ultimate biodegradation rate constants of 0.8–1.6 h^{-1} and rapid primary depolymerization at 5.0 h^{-1}. These values clearly demonstrate the rapid microbial breakdown of cellulose derivatives, underscoring their suitability as environmentally benign alternatives to persistent synthetic polymers [284]. Additionally, cellulose composites often exhibit strong adsorption and photocatalytic properties, making them effective for water purification and environmental remediation [159]. For example, cellulose/ZnO composites derived from agricultural waste exhibited 45% dye removal of bromophenol blue and methyl orange within 20 minutes of UV irradiation and 65% removal of methylene blue under either UV or white light, with only a 15–19% loss in performance after three reuse cycles, indicating both strong adsorption and durable photocatalytic activity [285].

Cellulose-based materials exhibit markedly better reusability and lower operational cost than nano-sized photocatalysts [36]. Regenerated cellulose–carbon hybrids retain 82–85% of their capacity after 10 cycles (2% loss per cycle) [286], whereas granular carbon based materials often recovers only 65% after a single regeneration cycle [287]. Life-cycle assessments further report production costs of US$1.06 kg^{-1} for biochar-based materials, compared with US$1.34 kg^{-1} for commercial AC [288]. These metrics confirm that cellulose-derived materials offer a significantly lower cost-per-use and superior long-term stability for sustainable adsorption applications.

Mechanically, cellulose composites show enhanced strength and toughness, combined with environmental sustainability attributes that many traditional materials lack. For example, ZnO/cellulose fiber composite membranes exhibit strong wet-state mechanical stability, with tensile stress increasing from 0.07 ± 0.01 MPa (microfiber-dominated structure) to 0.67 ± 0.02 MPa at an optimized nano-/micro-fiber ratio, while maintaining low mass loss (4.68 ± 1.35 wt%) after 48 h of dynamic oscillation in water, confirming the reinforcing synergy between microfibers and nanofibers [289]. Furthermore, cellulose possesses natural antibacterial properties, where synthetic materials typically require added antimicrobial agents [273].For instance, Ag@AgCl–cellulose hybrids have shown inhibition zones of 6.9 mm against *E. coli* and 10.8 mm against *S. aureus*, confirming effective microbial suppression through synergy between the cellulose matrix and active species. Similar cellulose–metal hybrid systems commonly achieve 3–5 log bacterial reduction, underscoring their strong antimicrobial potential. Such multifunctionality enables cellulose composites to integrate photocatalysis, adsorption, and antibacterial activity within a single biodegradable platform, enhancing their environmental and application value [290]. These reductions in carbon footprint, energy demand, wastewater generation, and regeneration cost translate into lower operational expenditure (OPEX) and

View Article Online
DOI: 10.1039/D5TA07511D

improved process efficiency, thereby strengthening the industrial scalability and market adoption potential of cellulose-supported photocatalysts.

Overall, cellulose-supported photocatalysts integrate low material cost, renewable feedstock availability, excellent recyclability, tunable physicochemical functionality, and strong environmental compatibility [257]. This broad relevance supports their expansion across water remediation, biomedical coatings, active packaging, and sustainable energy systems. The global cellulose market, valued at approximately USD 219.5 billion in 2018, is projected to reach USD 305.1 billion by 2026 at a CAGR of 4.2%, reflecting growing industrial demand for low-carbon materials [291]. Ongoing scale-up of green fabrication technologies is expected to further reduce costs and improve device-level efficiencies, strengthening the competitiveness of cellulose-based photocatalytic technologies. Such reductions in embodied energy, synthesis-related emissions, and regeneration costs directly translate to improved photocatalytic cost–performance ratios, thereby enhancing the feasibility of large-scale deployment and accelerating the commercial adoption of cellulose-supported photocatalytic systems.

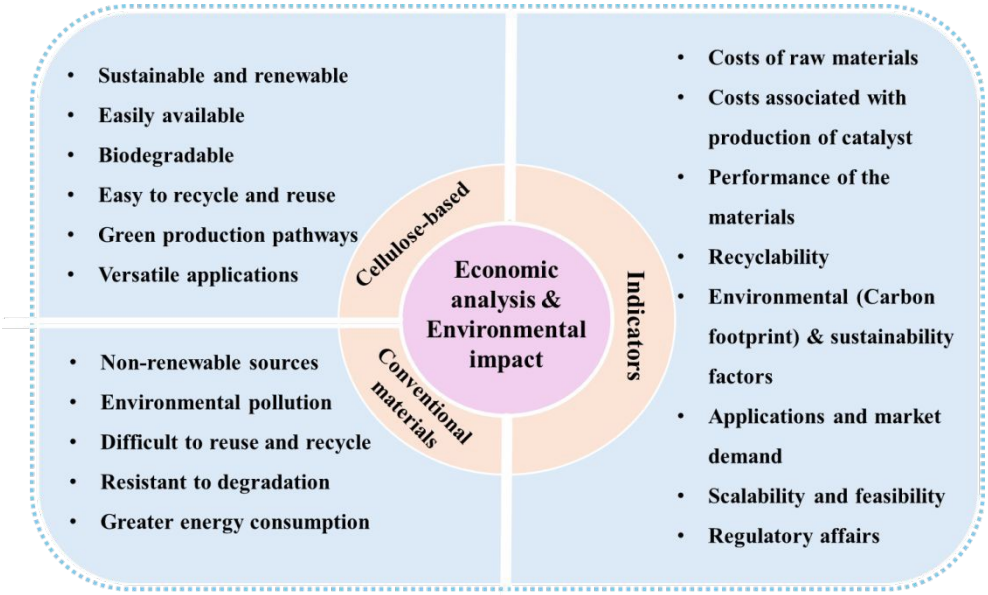

Fig. 15 Economic and environmental analysis of cellulose-based photocatalysts

8. Current challenges and prospects

The cellulose-based photocatalysts has attained prominent importance in the field of environmental remediation and sustainable fuel productions which contributed to the concept of green economy, circular economy, and SDGs. Despite of its functionality and efficacy, challenges are to be addressed to ensure the complete exploration of cellulose as a photocatalyst support. The major identified research areas that must be considered for the future research are discussed below:

(i) Technological advancements in cellulose-based photocatalysts: The deployment of cellulose-supported or derived photocatalysts is limited by intrinsic constraints such as low solubility, high crystallinity, restricted chain mobility,

View Article Online
DOI: 10.1039/D5TA07511D

and limited accessibility of surface-active hydroxyl groups. Conventional cellulose extraction and modification routes remain energy-intensive and environmentally taxing, limiting scalability. Future research must focus on developing processing methods that directly exploit cellulose's inherent physicochemical characteristics—hierarchical morphology, tunable crystallinity, and dense hydrogen-bond networks to optimize light absorption, interfacial charge separation, and catalytic site availability, instead of relying heavily on chemical post-modification. The integration of nano- and microcrystalline cellulose via in-situ assembly or self-templating routes can provide higher surface area and more uniform dispersion of catalytic components. Moreover, AI-assisted optimization of processing parameters, defect engineering, and rational dopant selection can improve performance reproducibility and accelerate the transition from laboratory demonstrations to practical systems.

(ii) Engineering smart cellulose platforms towards photocatalytic applications: The chemical richness of cellulose particularly its abundant reactive –OH groups enables versatile structure–property tuning through controlled functionalization. Tailored modifications (carbonization, carboxylation, grafting) can improve adsorption, wettability, and interfacial electron transfer, enhancing its role as an active contributor rather than a passive support. Challenges remain in achieving long-term structural stability, scalable processing, and reproducible functionalization. To avoid overlap with technological constraints, green-chemistry strategies are emphasized here specifically in the context of platform design such as solvent-free functionalization, bio-based modifiers for targeted surface chemistry, and energy-efficient activation pathways that allow the creation of adaptive cellulose architectures with tunable surface states. These engineered platforms can help establish consistent material properties and high compatibility with a wide range of photocatalytic semiconductors.

(iii) Heterostructures in cellulose-based catalysts: Incorporating heterostructures into cellulose matrices offers a promising pathway for achieving superior photocatalytic performance through enhanced charge separation, broadened light harvesting, and synergistic interfacial interactions. The intrinsic multi-scale structural order, mechanical flexibility, and high-aspect-ratio fibrils of cellulose enable efficient nanoparticle anchoring, dispersion, and stabilization attributes that conventional supports often lack. Despite these advantages, several materials-science challenges associated with heterostructure construction remain underexplored. Major obstacles include poorly controlled heterointerface formation that generates interfacial defects; lattice mismatch between inorganic semiconductors and the semi-crystalline cellulose framework; unpredictable band alignment arising from heterogeneous surface chemistry; and non-uniform nucleation leading to particle aggregation. Additionally, the effects of interfacial strain, exciton transport behaviour, and charge-transfer pathways across the organic–inorganic boundary are not yet fully understood. Current studies also lack mechanistic clarity on how cellulose modulates recombination dynamics through hydrogen bonding networks, surface functional groups, or crystalline polymorphs. To overcome these limitations, future work must emphasize defect-controlled and morphology-preserving fabrication strategies, coupled with green, solvent-minimal processing routes that align with sustainable material development. Equally important is the implementation of advanced characterization approaches including operando spectroscopies, interface-resolved electron microscopy, and multiscale theoretical modeling to establish clear structure–property–

View Article Online
DOI: 10.1039/D5TA07511D

performance correlations. Such integrated strategies will be essential for engineering next-generation cellulose-based heterojunction systems with predictable interfaces, optimized charge transport, and scalable manufacturability.

(iv) Hydrogels, sponges, and membranes for enhanced reuse: A major challenge for cellulose-based photocatalysts in real-world applications is achieving easy recovery, mechanical robustness, and long-term operational stability. Conventional powder catalysts often aggregate, exhibit poor recyclability, and lose activity over repeated cycles, motivating the shift toward structured formats such as hydrogels, sponges, and membranes. Cellulose imparts mechanical reinforcement, flexibility, and tunable functionality while enabling uniform dispersion of catalytic components. These macroscopic architectures improve reusability, stability, and scalability, making them better suited for practical water treatment. Future research should prioritize mechanical strengthening strategies, optimization of the porosity–strength balance, and enhanced fatigue resistance to support sustained performance in continuous-flow systems.

(v) AI-enhanced predictive modeling and kinetic analysis: AI/ML approaches can unravel complex dependencies between cellulose structure, material morphology, and photocatalytic behavior. Algorithms such as support vector regression, random forests, and neural networks can enable data-driven prediction of band structures, heterojunction stability, charge-transfer rates, and reaction kinetics, minimizing the need for iterative experimentation and accelerating material discovery.

(vi) Expanding photocatalytic applications towards fuel generation: Cellulose-supported photocatalysts are gaining traction in clean energy and green chemical synthesis, particularly for hydrogen, ammonia and hydrogen peroxide production. Their high surface area, functional tunability, and ability to support efficient charge separation make them ideal for coupling with semiconductors and co-catalysts. In hydrogen generation, cellulose scaffolds enhance light harvesting and charge transport, but challenges remain in achieving higher efficacy under visible light and ensuring catalyst durability. For ammonia synthesis via photocatalytic nitrogen fixation, cellulose-based system offers eco-friendly alternatives to the energy-intensive Haber-Bosch process; however low conversion rates and interference from combining reactions limits scalability. In hydrogen peroxide production, cellulose supports enable selective two-electron oxygen reduction, but requires precise control over reaction pathways to prevent undesired by-products. Across all applications, real-world deployment is hindered by limited quantum yields reliance on sacrificial agents.

(vii) Consideration of real wastewater scenarios: despite of extensive research and efficacy, the cellulose supported photocatalysts remain limited to laboratory scale studies. In contrast, industrial wastewater is complex and composed of variety of pathogens, organic, and inorganic pollutants, Cellulose-based catalysts must be designed not only for higher efficacy under ideal conditions but also for resilience and adaptability in real world applications. Further efforts should be given to fabrication of hybrid cellulose platforms that are capable of integrating multiple functional units for simultaneous degradation noxious pollutants. Finally, toxicity studies and pilot scale validations are critical in transforming cellulose based photocatalytic systems from proof-of-concept studies to industrial wastewater treatment technologies.

View Article Online
DOI: 10.1039/D5TA07511D

(viii) Advancing disinfection applications via photocatalysis: While cellulose-based photocatalysts exhibit strong potential for pathogen inactivation, challenges remain in understanding cellulose–microorganism interactions, ensuring non-toxicity of surface modifiers, and maintaining structural integrity in biological environments. Smart antimicrobial platforms with triggered ROS generation, anti-fouling surfaces, and biofilm disruption capabilities must be prioritized.

(ix) Challenges towards commercialization: The commercialization of cellulose-based photocatalysts faces several challenges that hinder their transition from laboratory to industrial scale. Cellulose is abundant and readily available from renewable resource such as wood pulp, cotton, bio-waste, and agricultural wastes, ensuring consistent quality, purity, and functional compatibility for advanced photocatalytic applications requires substantial processing and modifications which resulted in higher processing costs. Chemical treatments, surface functionalization, and integration with photocatalytic components involves complex, multi-step procedures that can limit scalability and introduces variability. One of the major technical hurdles lies in maintaining the inherent biodegradability, flexibility, and renewability of cellulose while imparting enhanced photocatalytic functionality, stability, and reusability. Further, performance optimization remains essential to meet industrial demands for thermal stability, mechanical strength, and long-term photocatalytic activity under diverse environmental conditions. standardized production protocols, rigorous quality control, and reproducibility are required to ensure consistent product performance. Environmental consideration must also be addressed, especially regarding the use of toxic chemicals or solvents during cellulose modifications and the generation of waste streams. Market uncertainty and lack of established models for bio-based photocatalytic materials further complicate commercialization efforts. To overcome these obstacles, it is vital to invest in green synthesis technologies, develop low-cost and eco-friendly modification methods. Strengthen R&D partnerships with industries, and engage with regulatory bodies to streamline approvals. The strategic collaborations, policy support, and pilot-scale demonstrations will be key to enabling the commercialization of cellulose-based photocatalysts as viable, scalable solutions for environmental remediation and clean energy applications.

9. Conclusions

Cellulose-supported photocatalysts represent a promising and sustainable solution to meet critical global challenges in clean energy production and environmental remediation. Their intrinsic properties including high surface area, biocompatibility, porosity, and chemical tunability make cellulose an ideal support material for photocatalysts. This review has provided as in-depth exploration of photocatalytic mechanisms, structural strategies, material classifications and application specific advances in cellulose based systems. A detailed emphasis is given to the design engineering aspects of cellulose-photocatalysts. This is followed by the classification of cellulose-supported photocatalysts into cellulose-based composite photocatalyst, and structured cellulose-based photocatalytic systems. The potential applications of cellulose-based catalysts are explored in the areas of hydrogen production, hydrogen peroxide production, ammonia generation, carbon dioxide sequestration, wastewater remediation, and disinfection. Among them, the citric acid functionalized g-C_3N_4 homojunction CMC hydrogels is the most efficient versatile photocatalyst capable of generating hydrogen peroxide (2341 μmol h^{-1} g^{-1}), ammonia (501 μmol h^{-1} g^{-1}) and degrading tetracycline (87%) with a reusability of 12 cycles. To comprehensively evaluate the field, a SWOT analysis was

View Article Online
DOI: 10.1039/D5TA07511D

conducted, which offers a systematic perspective on the current technological landscape, potential advantages, existing barriers, and future research opportunities. Despite significant progress, critical challenges remain in scaling up of fabrication, enhancing visible-light activity, ensuring long-term operational stability, and achieving commercial viability. Moving forward, innovations in heterostructure design, green processing methods, AI-driven optimizations, and real-world system integration will be pivotal. With focused interdisciplinary efforts, cellulose-supported photocatalysts can play a central role in enabling scalable, eco-friendly, and multifunctional technologies aligned with the principles of circular economy and United Nations Sustainable Development Goals.

Acknowledgment

Dr. Akash Balakrishnan gratefully acknowledges the financial support received under the *Research Seed Money (RSM) Scheme* from APJ Abdul Kalam Technological University (KTU), Kerala, India.

Reference

1 H. Dong, G. Zeng, L. Tang, C. Fan, C. Zhang, X. He and Y. He, *Elsevier Ltd*, 2015, DOI: 10.1016/j.watres.2015.04.038.

2 X.-J. Wen, X. Wu, L. Hu, X.-K. Wu, H. Guo, B.-B. Qian, Z.-T. Liu, H.-Z. Li and Z.-H. Fei, *Coord. Chem. Rev.*, 2025, **526**, 216377.

3 A. Balakrishnan, F. P. Mathew, E. Sebastian Kunnel, M. M. Varghese, S. Trivedi, M. Binoy, M. Chinthala, N. Rajamohan and B. Weng, *Nanoscale*, DOI:10.1039/D5NR02485D.

4 A. Balakrishnan, M. M. Jacob, M. Chinthala, N. Dayanandan, M. Ponnuswamy and D.-V. N. Vo, *Environ. Chem. Lett.*, 2024, **22**, 635–656.

5 A. Balakrishnan, S. Appunni, M. Chinthala and D. V. N. Vo, *Springer International Publishing*, 2022, DOI: 10.1007/s10311-022-01443-8.

6 X. Song, Y. Duan, S. Li, P. Ouyang, L. Chen, H. Ma, W. Wang, Y. Li and F. Dong, *Coord. Chem. Rev.*, 2025, **526**, 216351.

7 B. Weng, M. Zhang, Y. Lin, J. Yang, J. Lv, N. Han, J. Xie, H. Jia, B. Su, M. Roeffaers, J. Hofkens, Y. Zhu, S. Wang and W. Choi, *Nat. Rev. Clean Technol.*, 2025, **1**, 201–215.

8 A. Balakrishnan, S. Appunni and K. Gopalram, *Int. J. Biol. Macromol.*, 2020, **161**, 282–291.

9 Q. Xu, B. Zhu, C. Jiang, B. Cheng and J. Yu, *Sol. RRL*, 2018, **2**, 1–10.

10 Z. Ding, S. Wang, X. Chang, D. H. Wang and T. Zhang, *RSC Adv.*, 2020, **10**, 26246–26255.

11 S. Li, S. Meng, H. Zhang, A. R. Puente-Santiago, Z. Wang, S. Chen, M. J. Muñoz-Batista, Y.-M. Zheng and B. Weng, *Adv. Funct. Mater.*, 2025, **n/a**, e13682.

View Article Online
DOI: 10.1039/D5TA07511D

12 N. Rana, S. Chand and A. K. Gathania, *Int. Nano Lett.*, 2016, **6**, 91–98.

13 K. Wang, Z. Xing, M. Du, S. Zhang, Z. Li, S. Yang, K. Pan, J. Liao and W. Zhou, *J. Colloid Interface Sci.*, 2021, **592**, 259–270.

14 Q. Chen, Z. Zhang, Y. Chen, J. C. Yu, C. Liu and L. Wu, *Appl. Catal. B Environ. Energy*, 2026, **380**, 125823.

15 A. Balakrishnan, K. Vijaya Suryaa, M. Chinthala and A. Kumar, *J. Colloid Interface Sci.*, 2024, **669**, 366–382.

16 Y. Ai, S. A. C. Carabineiro, X. Xiong, H. Zhu, Q. Wang, B. Weng and M.-Q. Yang, *Chinese J. Catal.*, 2025, **75**, 147–163.

17 H. Yan, Z. Zhu, Y. Long and W. Li, *Colloids Surfaces A Physicochem. Eng. Asp.*, 2019, **582**, 123857.

18 A. Balakrishnan and M. Chinthala, *Chemosphere*, 2022, 134190.

19 A. Balakrishnan, E. S. Kunnel, R. Sasidharan, M. Chinthala and A. Kumar, *Chem. Eng. J.*, 2023, 146163.

20 C. F. H DOng, G. Zeng, L. Tang, *Water Res.*, DOI:10.1016/j.watres.2015.04.038.

21 S. H. Khan and B. Pathak, *Environ. Nanotechnology, Monit. Manag.*, 2020, **13**, 100290.

22 Y. Ren, Y. Li, G. Pan, N. Wang, Y. Xing and Z. Zhang, *J. Mater. Sci. Technol.*, 2024, **171**, 162–184.

23 J. Thomas, K. S. Ambili and S. Radhika, *Catal. Today*, 2018, **310**, 11–18.

24 A. Balakrishnan, R. Sasidharan, M. Chinthala and A. Kumar, *Ind. Eng. Chem. Res.*, 2024, **63**, 2605–2618.

25 K. Vijaya Suryaa, A. Balakrishnan, M. Chinthala, K. Bidya Devi, H. Tripathy, A. Kumar, T. M. Aminabhavi and S. Rtimi, *Chem. Eng. J.*, 2025, **505**, 159470.

26 I. E. Khalil, C. Xue, W. Liu, X. Li, Y. Shen, S. Li, W. Zhang and F. Huo, *Adv. Funct. Mater.*, 2021, **31**, 2010052.

27 D. Wang, X. Huang, Y. Huang, X. Yu, Y. Lei, X. Dong and Z. Su, *Colloids Surfaces A Physicochem. Eng. Asp.*, 2021, **611**, 125780.

28 P. Zhou, X. Meng, L. Li and T. Sun, *J. Alloys Compd.*, 2020, **827**, 154259.

29 D. Hao, Q. Huang, W. Wei, X. Bai and B. J. Ni, *J. Clean. Prod.*, 2021, **314**, 128033.

30 C. Liu, J. You, Y. Li, H. Zhu, L. Xia and X. Zhuang, *Carbohydr. Polym.*, 2023, **316**, 121072.

31 H. M. Ali, F. Arabpour Roghabadi and V. Ahmadi, *Sol. Energy*, 2023, **255**, 99–125.

32 H. Musarurwa and N. T. Tavengwa, *Carbohydr. Polym.*, 2022, **275**, 118743.

View Article Online
DOI: 10.1039/D5TA07511D

33 H. N. Abdelhamid and A. P. Mathew, *Coord. Chem. Rev.*, 2022, **451**, 214263.

34 M. A. Mohamed, M. Abd Mutalib, Z. A. Mohd Hir, M. F. M. Zain, A. B. Mohamad, L. Jeffery Minggu, N. A. Awang and W. N. W. Salleh, 2017, DOI: 10.1016/j.ijbiomac.2017.05.181.

35 M. Li, W. Yao, M. Yu, C. Sun, X. Deng, F. Chen, L. Zhou and Y. Zheng, *Sep. Purif. Technol.*, 2022, **299**, 121758.

36 A. Balakrishnan, K. Vijaya Suryaa, H. Tripathy, S. Trivedi, A. Kumar and M. Chinthala, *J. Colloid Interface Sci.*, DOI:https://doi.org/10.1016/j.jcis.2024.02.110.

37 J. Wen, J. Xie, X. Chen and X. Li, *Appl. Surf. Sci.*, 2017, **391**, 72–123.

38 A. Balakrishnan, M. Chinthala, R. Polagani and D.-V. N. Vo, *Environ. Res.*, 2023, **216**, 18–52.

39 S. Meenakshi and M. Farzana, *Ind. Eng. Chem. Res.*, 2013, **53**, 55–63.

40 R. Bariki, S. Kumar Pradhan, S. Panda, S. Kumar Nayak, D. Majhi, K. Das and B. G. Mishra, *Sep. Purif. Technol.*, 2023, **314**, 123558.

41 K. Das, R. Bariki, S. K. Pradhan, D. Majhi, P. Dash, A. Mishra, R. Dhiman, B. Nayak and B. G. Mishra, *Chemosphere*, 2022, **306**, 135600.

42 Y. Li, Y. Fang, Z. Cao, N. Li, D. Chen, Q. Xu and J. Lu, *Appl. Catal. B Environ.*, 2019, **250**, 150–162.

43 M. Chinthala, A. Balakrishnan, P. Venkataraman, V. Manaswini Gowtham and R. K. Polagani, *Environ. Chem. Lett.*, 2021, **19**, 4415–4454.

44 K. Das, R. Bariki, D. Majhi, A. Mishra, K. K. Das, R. Dhiman and B. G. Mishra, *Appl. Catal. B Environ.*, 2022, **303**, 120902.

45 S. Vigneshwaran, P. Sirajudheen, C. P. Nabeena, V. P. Sajna and S. Meenakshi, *Int. J. Biol. Macromol.*, 2021, **183**, 2088–2099.

46 A. Balakrishnan, M. Chinthala, A. Kumar, N. Dayanandan and S. Trivedi, *Int. J. Hydrogen Energy*, 2025, **98**, 1020–1033.

47 W. Kong, Z. Xing, B. Fang, Y. Cui, Z. Li and W. Zhou, *Appl. Catal. B Environ.*, 2022, **304**, 120969.

48 Y. Xue, C. Ma, Q. Yang, X. Wang, S. An, X. Zhang and J. Tian, *Chem. Eng. J.*, 2023, **457**, 141146.

49 X. Liu, R. Ma, L. Zhuang, B. Hu, J. Chen, X. Liu and X. Wang, *Crit. Rev. Environ. Sci. Technol.*, 2021, **51**, 751–790.

50 L. Jiang, X. Yuan, Y. Pan, J. Liang, G. Zeng, Z. Wu and H. Wang, *Elsevier B.V.*, 2017, DOI: 10.1016/j.apcatb.2017.06.003.

View Article Online
DOI: 10.1039/D5TA07511D

51 S. Singh, H. Mahalingam and P. K. Singh, *Elsevier*, 2013, DOI: 10.1016/j.apcata.2013.04.039.

52 J. Fu, J. Yu, C. Jiang and B. Cheng, *Adv. Energy Mater.*, 2018, **8**, 1–31.

53 J. Low, J. Yu, M. Jaroniec, S. Wageh and A. A. Al-Ghamdi, *Adv. Mater.*, 2017, **29**, 1–20.

54 J. Lee, L. L. Tan and S. P. Chai, *Nanoscale*, 2021, **13**, 7011–7033.

55 A. Balakrishnan, G. J. Gaware and M. Chinthala, *Chemosphere*, 2023, **310**, 136853.

56 A. Balakrishnan, M. Chinthala, A. Kumar and S. Rtimi, *Chem. Eng. J.*, 2024, **496**, 153899.

57 S. Chen, D. Huang, P. Xu, W. Xue, L. Lei, M. Cheng, R. Wang, X. Liu and R. Deng, *J. Mater. Chem. A*, 2020, **8**, 2286–2322.

58 H. Park, H. Il Kim, G. H. Moon and W. Choi, *Energy Environ. Sci.*, 2016, **9**, 411–433.

59 C. Zhang, Y. Li, D. Shuai, Y. Shen and D. Wang, *Chem. Eng. J.*, 2019, **355**, 399–415.

60 A. Y. Shan, T. I. M. Ghazi and S. A. Rashid, *Appl. Catal. A Gen.*, 2010, **389**, 1–8.

61 A. Balakrishnan, E. S. Kunnel, R. Sasidharan, M. Chinthala and A. Kumar, *ACS Sustain. Chem. Eng.*, DOI:10.1021/acssuschemeng.3c07961.

62 M. Lee, B. Y. Chen and W. Den, *MDPI AG*, 2015, DOI: 10.3390/app5041272.

63 A. A. Adesibikan, S. S. Emmanuel, C. O. Olawoyin and P. Ndungu, *J. Organomet. Chem.*, 2024, **1010**, 123087.

64 A. Sudhaik, P. Raizada, T. Ahamad, S. M. Alshehri, V.-H. Nguyen, Q. Van Le, S. Thakur, V. K. Thakur, R. Selvasembian and P. Singh, *Int. J. Biol. Macromol.*, 2023, **226**, 1284–1308.

65 P. Xu, J. Yang, Y. Chen, Y. Li, X. Jia and H. Song, *Mater. Des.*, 2019, **183**, 108179.

66 T. Shan, Y. Wang, D. Luo, Z. Huang, F. Zhang, H. Wu, L. Huang, J. Li, L. Chen and H. Xiao, *Appl. Catal. B Environ. Energy*, 2024, **349**, 123872.

67 W. Chen, C. Hou, Y. Wang, L. Fu, S. Zhang and J. Wang, .

68 A. Liu, J. Liu, S. He, J. Zhang and W. Shao, *Int. J. Biol. Macromol.*, 2023, **225**, 40–50.

69 B. S. T. K, J. C. C. S, S. Sasi and C. K. Arundhathi, eds. S. Thomas, M. Hosur, D. Pasquini and C. Jose Chirayil, Springer Nature Singapore, Singapore, 2023, pp. 1–37.

70 B. A. Marinho, R. O. Cristóvão, R. Djellabi, J. M. Loureiro, R. A. R. Boaventura and V. J. P. Vilar, *Appl. Catal. B Environ.*, 2017, **203**, 18–30.

71 M. A. Mohamed, W. W. N. Salleh, J. Jaafar, A. F. Ismail, M. A. Mutalib, N. A. A. Sani, S. E. A. M. Asri

View Article Online
DOI: 10.1039/D5TA07511D

and C. S. Ong, *Chem. Eng. J.*, 2016, **284**, 202–215.

72 Y. Zhang, F. Liu, L. Zhong, Z. Dong, C. Chen and Z. Xu, *Appl. Surf. Sci.*, 2023, **641**, 158425.

73 H. Xiao, Y. Shan, S. Wu, T. Shan, H. Luo, F. Zhang, L. Huang, L. Chen and G. Liao, *Chem. Eng. J.*, 2024, **492**, 152228.

74 M. Österberg, K. A. Henn, M. Farooq and J. J. Valle-Delgado, *Chem. Rev.*, 2023, **123**, 2200–2241.

75 H. Nasser Abdelhamid, S. Sultan and A. P. Mathew, *Chem. Eng. J.*, 2023, **468**, 143567.

76 R. N. Goldberg, J. Schliesser, A. Mittal, S. R. Decker, A. F. L. O. M. Santos, V. L. S. Freitas, A. Urbas, B. E. Lang, C. Heiss, M. D. M. C. Ribeiro da Silva, B. F. Woodfield, R. Katahira, W. Wang and D. K. Johnson, *J. Chem. Thermodyn.*, 2015, **81**, 184–226.

77 E. Dinand, M. Vignon, H. Chanzy and L. Heux, *Cellulose*, 2002, **9**, 7–18.

78 Y. Liang, W. Zhu, C. Zhang, R. Navik, X. Ding, M. S. Mia, M. N. Pervez, M. I. H. Mondal, L. Lin and Y. Cai, *Cellulose*, 2021, **28**, 7435–7453.

79 C. Huang, H. Yu, S. Y. H. Abdalkarim, Y. Li, X. Chen, X. Yang, Y. Zhou and L. Zhang, *Carbohydr. Polym.*, 2022, **276**, 118766.

80 D. Zhi, J. Wang, Y. Zhou, Z. Luo, Y. Sun, Z. Wan, L. Luo, D. C. W. Tsang and D. D. Dionysiou, *Chem. Eng. J.*, 2020, **383**, 123149.

81 R. S. Riseh, M. G. Vazvani, M. Hassanisaadi and V. K. Thakur, *Ind. Crops Prod.*, 2024, **208**, 117904.

82 P. Gao, H. Y. Khong, A. Wibowo, Y. Zhen, C. Peng and W. Miao, *Heliyon*, DOI:10.1016/j.heliyon.2024.e32321.

83 R. Roy, M. Eldhose, C. George and A. Joseph, eds. S. Thomas, A. AR, C. Jose Chirayil and B. Thomas, Springer Nature Singapore, Singapore, 2023, pp. 1059–1084.

84 M. Sumini, G. J. S. Andrade, C. A. Tischer, R. K. T. Kobayashi and G. Nakazato, *Cellulose*, 2025, **32**, 81–94.

85 S. Balkissoon, J. Andrew and B. Sithole, *Biomass Convers. Biorefinery*, 2023, **13**, 16607–16642.

86 N. Lavoine, I. Desloges, A. Dufresne and J. Bras, *Carbohydr. Polym.*, 2012, **90**, 735–764.

87 K. J. Nagarajan, N. R. Ramanujam, M. R. Sanjay, S. Siengchin, B. Surya Rajan, K. Sathick Basha, P. Madhu and G. R. Raghav, *Polym. Compos.*, 2021, **42**, 1588–1630.

88 A. Sharma, M. Thakur, M. Bhattacharya, T. Mandal and S. Goswami, *Biotechnol. Reports*, 2019, **21**, e00316.

View Article Online
DOI: 10.1039/D5TA07511D

89 G. Yang, H. Kong, Y. Chen, B. Liu, D. Zhu, L. Guo and G. Wei, *Carbohydr. Polym.*, 2022, **279**, 118947.

90 Y. Shan, Y. Guo, Y. Wang, X. Du, J. Yu, H. Luo, H. Wu, B. Boury, H. Xiao, L. Huang and L. Chen, *J. Colloid Interface Sci.*, 2021, **599**, 507–518.

91 T. T. Hong, H. Okabe, Y. Hidaka, B. A. Omoldi and K. Hara, *Polymer (Guildf).*, 2019, **181**, 121772.

92 A. Rana, A. Sudhaik, P. Raizada, A. A. P. Khan, Q. Van Le, A. Singh, R. Selvasembian, A. Nadda and P. Singh, *Nanotechnol. Environ. Eng.*, 2021, **6**, 40.

93 X. Qian, Y. Xu and Y. Xu, *Int. J. Biol. Macromol.*, 2024, **259**, 127873.

94 A. Balakrishnan, M. Chinthala, A. Kumar, D. Barceló and S. Rtimi, *Chem. Eng. J.*, 2025, **503**, 158378.

95 Y. Guo, J. Bae, Z. Fang, P. Li, F. Zhao and G. Yu, *Chem. Rev.*, 2020, **120**, 7642–7707.

96 Y. Wang, X. Wang, Y. Xie and K. Zhang, *Cellulose*, 2018, **25**, 3703–3731.

97 A. Kumar, G. Sharma, M. Naushad, A. H. Al-Muhtaseb, A. García-Peñas, G. T. Mola, C. Si and F. J. Stadler, *Chem. Eng. J.*, 2020, **382**, 122937.

98 C. Shi, B. An, L. Zhang, Z. Zai, Z. Shi, Z. Wang and J. Ma, *Appl. Surf. Sci.*, 2023, **618**, 156633.

99 B. Mohan, *Top. Curr. Chem.*, 2025, **383**, 44.

100 K. M. Alam, P. Kumar, N. Chaulagain, S. Zeng, A. Goswami, J. Garcia, E. Vahidzadeh, M. L. Bhaiyya, G. M. Bernard, S. Goel, V. K. Michaelis, A. E. Kobryn, S. Gusarov and K. Shankar, *J. Phys. Chem. C*, 2022, **126**, 15635–15650.

101 Y. Li, M. Wang, Y. Meng, Q. Wang, Q. Fu, C. Yu, L. Zhu, L. Cai, C. Chen, C. Xia and S. Wang, *ACS Appl. Mater. Interfaces*, 2025, **17**, 30365–30401.

102 S. Ghosh, D. Sarkar, S. Bastia and Y. S. Chaudhary, .

103 Y. Shchipunov and I. Postnova, *Adv. Funct. Mater.*, 2018, **28**, 1705042.

104 A. Etale, A. J. Onyianta, S. R. Turner and S. J. Eichhorn, *Chem. Rev.*, 2023, **123**, 2016–2048.

105 M. Hasanin, R. M. Abdelhameed, S. Dacrory, H. Abou-Yousef and S. Kamel, *Mater. Sci. Eng. B*, 2021, **270**, 115231.

106 H. Tian and J. He, *Langmuir*, 2016, **32**, 12269–12282.

107 S. Habibi and M. Jamshidi, *Mater. Sci. Semicond. Process.*, 2020, **109**, 104927.

108 C. Shi, L. Zhang, Z. Shi, Z. Wang and J. Ma, *Int. J. Biol. Macromol.*, 2023, **228**, 435–444.

109 M. Yan, B. An, X. Li, Z. Zai, S. Wu, J. Ma and L. Zhang, *Appl. Surf. Sci.*, 2023, **637**, 157974.

View Article Online
DOI: 10.1039/D5TA07511D

110 J. Liu, S. Tang, P. Zhang, Z. Wang, W. Dai, R. Wen, L. Wang, W. Wang and J. Wang, *J. Colloid Interface Sci.*, 2025, **700**, 138411.

111 A. Manuscript, *J. Mater. Chem. A*, DOI:10.1039/C9TA12665A.

112 G. Chu, H. Yin, H. Jiang, D. Qu, Y. Shi, D. Ding and Y. Xu, *J. Phys. Chem. C*, 2016, **120**, 27541–27547.

113 C. Shi, L. Zhang, H. Bian, Z. Shi, J. Ma and Z. Wang, *J. Clean. Prod.*, 2021, **288**, 125089.

114 S. Liu, T. Xu, L. Zhu, K. Liu, X. Ji, Z. Yuan and C. Si, *Chem. Eng. J.*, 2025, **503**, 158564.

115 N. Lakshmana Reddy, V. Navakoteswara Rao, M. Mamatha Kumari, R. R. Kakarla, P. Ravi, M. Sathish, M. Karthik, S. Muthukonda Venkatakrishnan and Inamuddin, *Nanostructured semiconducting materials for efficient hydrogen generation*, Springer International Publishing, 2018, vol. 16.

116 N. Shehzad, M. Tahir, K. Johari, T. Murugesan and M. Hussain, *J. CO2 Util.*, 2018, **26**, 98–122.

117 X. Zhang and S. P. Jiang, *Mater. Today Energy*, 2022, **23**, 100904.

118 B. Palanivel, R. R. Macadangdang, M. S. Hossain, F. A. Alharthi, M. Kumar, J.-H. Chang and S. Gedi, *J. Rare Earths*, 2023, **41**, 77–84.

119 J. Qin, Y. Dou, J. Zhou, V. M. Candelario, H. R. Andersen, C. Hélix-Nielsen and W. Zhang, *Adv. Funct. Mater.*, 2023, **33**, 2214839.

120 F. Guo, W. Shi, W. Guan, H. Huang and Y. Liu, *Sep. Purif. Technol.*, 2017, **173**, 295–303.

121 X. Hu, Y. Yu, D. Chen, W. Xu, J. Fang, Z. Liu, R. Li, L. Yao, J. Qin and Z. Fang, *Chem. Eng. J.*, 2022, **432**, 134375.

122 S. Sugashini, T. Gomathi, R. A. Devi, P. N. Sudha, K. Rambabu and F. Banat, *Environ. Res.*, 2022, **204**, 112047.

123 N. Janpetch, N. Saito and R. Rujiravanit, *Carbohydr. Polym.*, 2016, **148**, 335–344.

124 H. Li, L. Zhang, H. Lu, J. Ma, X. Zhou, Z. Wang and C. Yi, *Carbohydr. Polym.*, 2020, **250**, 116873.

125 H. Helmiyati, N. Fitriana, M. L. Chaerani and F. W. Dini, *Opt. Mater. (Amst).*, 2022, **124**, 111982.

126 S. Pushpalatha, M. V Arularasu, C. Palanivel, T. V Rajendran and A. Manikandan, *Biomass Convers. Biorefinery*, DOI:10.1007/s13399-024-05708-w.

127 V. Soni, M. Malhotra, P. Singh, A. A. P. Khan, W. A. Bawazir, V.-H. Nguyen, T. Ahamad, Q. Van Le, P. Raizada and K. A. Alzahrani, *J. Environ. Chem. Eng.*, 2025, **13**, 115151.

128 M. Malhotra, A. Sudhaik, Sonu, P. Raizada, T. Ahamad, V.-H. Nguyen, Q. Van Le, R. Selvasembian, A. K. Mishra and P. Singh, *Ind. Crops Prod.*, 2023, **202**, 117000.

View Article Online
DOI: 10.1039/D5TA07511D

129 T. Zhang, Y. Xiang, Y. Su, Y. Zhang, X. Huang and X. Qian, *Ind. Crops Prod.*, 2022, **187**, 115357.

130 Q. Wang, Y. Xiang, X. Li, W. Zhang, X. Huang and X. Qian, *Ind. Crops Prod.*, 2021, **170**, 113695.

131 Z. Xu, M. He, Y. Zhou, M. Zhang, S. Feng, Y. Wang, R. Xu, H. Peng and X. Chen, *Chem. Eng. J.*, 2022, **428**, 131127.

132 S. Jiang, Q. Hu, M. Xu, S. Hu, X.-C. Shi, R. Ding, P.-L. Tremblay and T. Zhang, *Carbohydr. Polym.*, 2020, **250**, 116909.

133 N. Tavker and M. Sharma, *J. Environ. Manage.*, 2020, **255**, 109906.

134 C. Liao, W. Jing, F. Wang and Y. Liu, *Mater. Today Catal.*, 2023, **3**, 100030.

135 Y. Liang, J. Xiong, Q. Yang and S. Wang, *J. Colloid Interface Sci.*, 2023, **651**, 976–986.

136 P. Zhang, J. Zhang, D. Wang, F. Zhang, Y. Zhao, M. Yan, C. Zheng, Q. Wang, M. Long and C. Chen, *Appl. Catal. B Environ.*, 2022, **318**, 121749.

137 H. Xu, Y. Zhang, Y. Wang, L. Zhang, Z. Zhang, L. Zhong, Z. He, Y. Zheng and Y. Shen, *Carbohydr. Polym.*, 2023, **312**, 120829.

138 C. Zhao, F. Ran, L. Dai, C. Li, C. Zheng and C. Si, *Carbohydr. Polym.*, 2021, **255**, 117343.

139 N. S. N. Hasnan, M. A. Mohamed, N. A. Nordin, W. N. R. Wan Ishak and M. B. Kassim, *Carbohydr. Polym.*, 2023, **317**, 121096.

140 C. Yue, L. Chen, H. Zhang, J. Huang, H. Jiang, H. Li and S. Yang, *Environ. Sci. Water Res. Technol.*, 2023, **9**, 669–695.

141 A. Balakrishnan, M. M. Jacob, N. Dayanandan, M. Chinthala, M. Ponnuchamy, D. V. N. Vo, S. Appunni and A. S. Gajendhran, *Mater. Adv.*, 2023, **4**, 5920–5947.

142 S. Bej, H. Sarma, M. Ghosh and P. Banerjee, *Environ. Pollut.*, 2023, **323**, 121278.

143 J. Khodayari, K. Zare, O. Moradi, M. Kalaee and N. Mohammad Mahmoodi, *J. Photochem. Photobiol. A Chem.*, 2024, **446**, 115097.

144 L. Zheng, S. Wang, S. Zhang, Y. Zu, X. Huang and X. Qian, *J. Colloid Interface Sci.*, 2024, **676**, 532–542.

145 J. Wang, W. Wang, Y. Deng, T. Yang, Z. Zhang, H. Wang and Y. Wu, *Sep. Purif. Technol.*, 2024, **340**, 126840.

146 S. Jiang, Z. Yan, Y. Deng, W. Deng, H. Xiao and W. Wu, *Int. J. Biol. Macromol.*, 2024, **262**, 129854.

147 Z. Yuan, Y. Chen, C. Qiu, M.-C. Li, J. Qi, C. F. de Hoop, A. Zhao, J. Lai, X. Zhang and X. Huang, *Int. J. Biol. Macromol.*, 2023, **249**, 126118.

View Article Online
DOI: 10.1039/D5TA07511D

148 J.-X. Ren, J.-L. Zhu, S.-C. Shi, M.-Q. Yin, H.-D. Huang and Z.-M. Li, *Carbohydr. Polym.*, 2022, **296**, 119957.

149 Y. Xue, Y. Lu, K. Feng, C. Zhang, X. Feng, Y. Zhao and L. Chen, *Int. J. Biol. Macromol.*, 2023, **250**, 125891.

150 X. Qi, X. Xiong, M. Liu, Y. Zhang, X. Zhang, P. Jiang, Y. Wu, X. Guo and H. Tong, *Carbohydr. Polym.*, 2024, **326**, 121623.

151 S. Kang, M. Chen, Y. Wang, F. Tang, Y. Liu, L. Cui and M. Dong, *Sustain. Energy Fuels*, 2022, **7**, 409–419.

152 D. Zhu, S. Handschuh-Wang and X. Zhou, *Recent progress in fabrication and application of polydimethylsiloxane sponges*, 2017, vol. 5.

153 P. Zhou, B. Qin, L. Zhang, Z. Wu, Y. Dai, C. Hu, H. Xu and Z. Mao, *Int. J. Biol. Macromol.*, 2023, **239**, 124233.

154 J. You, C. Liu, X. Feng, B. Lu, L. Xia and X. Zhuang, *Carbohydr. Polym.*, 2022, **288**, 119332.

155 E. F. Assanvo, S. Nagaraj, D. Boa and P. Thanikaivelan, *Sci. Rep.*, 2023, **13**, 13365.

156 L. Xia, L. Shi, J. Zhao, C. Liu, Y. Di and X. Zhuang, *Front. Chem. Sci. Eng.*, 2025, **19**, 33.

157 S. Nardecchia, D. Carriazo, M. L. Ferrer, M. C. Gutiérrez and F. del Monte, *Chem. Soc. Rev.*, 2013, **42**, 794–830.

158 L. Chen, S. Liu, X. Guo, S. Wang, Z. He, Q. Xu, Q. Zhang, J. Zhu, P. Zhao, S. Yang and Q. Wang, *Sep. Purif. Technol.*, 2024, **330**, 125192.

159 N. Amaly, A. Y. EL-Moghazy, N. Nitin, G. Sun and P. K. Pandey, *Chem. Eng. J.*, 2022, **430**, 133077.

160 B. Yan, Y. Dai, Y. Li, L. Xin, M. Li, H. Long and X. Gao, *Int. J. Biol. Macromol.*, 2025, **306**, 141748.

161 X. Zou, L. Yao, S. Zhou, G. Chen, S. Wang, X. Liu and Y. Jiang, *Carbohydr. Polym.*, 2022, **296**, 119970.

162 J. Pan, D. Hua, Y. Hong, X. Cheng, F. Guo, K. Bing Tan, Z. Zhong and G. Zhan, *Chem. Eng. J.*, 2023, **466**, 143164.

163 C. N. Rani, S. Karthikeyan and S. Prince Arockia Doss, *Chem. Eng. Process. - Process Intensif.*, 2021, **165**, 108445.

164 W. Lu, C. Duan, Y. Zhang, K. Gao, L. Dai, M. Shen, W. Wang, J. Wang and Y. Ni, *Carbohydr. Polym.*, 2021, **258**, 117676.

165 E. J. M. Dantas, M. E. Alves, S. Arias, A. G. Camara, J. V. F. L. Cavalvanti, G. L. Silva, C. M. B. M. Barbosa and J. G. A. Pacheco, *Catal. Today*, 2024, **441**, 114846.

View Article Online
DOI: 10.1039/D5TA07511D

166 H. Wu, T. Inaba, Z.-M. Wang and T. Endo, *Appl. Catal. B Environ.*, 2020, **276**, 119111.

167 A. Rajeswari, S. Vismaiya and A. Pius, *Chem. Eng. J.*, 2017, **313**, 928–937.

168 Z. Yin, X. Chen, T. Zhou, M. Xue, M. Li, K. Liu, D. Zhou, J. Ou, Y. Xie, Z. Ren, Y. Luo and Z. Hong, in *Separation and Purification Technology*, 2022, vol. 286, p. 120504.

169 T. Li, N. Tsubaki and Z. Jin, *J. Mater. Sci. Technol.*, 2024, **169**, 82–104.

170 H. Hou, X. Zeng and X. Zhang, *Angew. Chemie Int. Ed.*, 2020, **59**, 17356–17376.

171 D. Majhi, K. Das, R. Bariki, S. Padhan, A. Mishra, R. Dhiman, P. Dash, B. Nayak and B. G. Mishra, *J. Mater. Chem. A*, 2020, **8**, 21729–21743.

172 M. Zhou, J. Chen, C. Hou, Y. Liu, S. Xu, C. Yao and Z. Li, *Appl. Surf. Sci.*, 2019, **470**, 908–916.

173 P. Wang, Z. Geng, J. Gao, R. Xuan, P. Liu, Y. Wang, K. Huang, Y. Wan and Y. Xu, *J. Mater. Chem. A*, 2015, **3**, 1709–1716.

174 Y. Chen, W. Shao, C. Zhou, G. Tai, G. Wu and W. Xing, *ACS Appl. Energy Mater.*, 2023, **6**, 11705–11717.

175 D. Ke, S. Liu, K. Dai, J. Zhou, L. Zhang and T. Peng, *J. Phys. Chem. C*, 2009, **113**, 16021–16026.

176 L. Zheng, K. Zhong, X. Huang and X. Qian, *Cellulose*, 2024, **31**, 2523–2540.

177 S. Belda-Marco, P. Ayala, S. N. Myakala, D. Eder, M. Á. Lillo-Ródenas, A. Cherevan and M. C. Román-Martínez, *Environ. Res.*, 2025, **271**, 121141.

178 Z. Chen, D. Yao, C. Chu and S. Mao, *Chem. Eng. J.*, 2023, **451**, 138489.

179 L. Deng, J. Sun, J. Sun, X. Wang, T. Shen, R. Zhao, Y. Zhang and B. Wang, *Appl. Surf. Sci.*, 2022, **597**, 153586.

180 Y. Wu, S. Yan, L. Wang, L. Chen, Y. Li and K. Shen, *Appl. Catal. B Environ. Energy*, 2025, **375**, 125418.

181 J. Zhou, T. Shan, S. Wu, J. Li, F. Zhang, L. Huang, L. Chen and H. Xiao, *Chem. Eng. J.*, 2024, **492**, 152441.

182 G. Zhang, X. Rong, W. Huang, Z. Xiao, Z. Xue, H. Cheng, J. Feng and L. Li, *Colloids Surfaces A Physicochem. Eng. Asp.*, 2025, **709**, 136202.

183 X. Wang, S. Yuan, B. Feng, X. Qiu, C. Yu, W. Lu, X. Xu, Y. Hu and Y. Shi, *J. Colloid Interface Sci.*, 2025, **691**, 137371.

184 W. Miao, D. Yao, C. Chu, Y. Liu, Q. Huang, S. Mao and K. (Ken) Ostrikov, *Appl. Catal. B Environ.*, 2023, **332**, 122770.

185 J. Zhou, T. Shan, F. Zhang, B. Boury, L. Huang, Y. Yang, G. Liao, H. Xiao and L. Chen, *Adv. Fiber Mater.*, 2024, **6**, 387–400.

View Article Online
DOI: 10.1039/D5TA07511D

186 L. Xu, Y. Liu, L. Li, Z. Hu and J. C. Yu, *ACS Catal.*, 2021, **11**, 14480–14488.

187 Y. Liu, X. Wang, Y. Zhao, Q. Wu, H. Nie, H. Si, H. Huang, Y. Liu, M. Shao and Z. Kang, *Nano Res.*, 2022, **15**, 4000–4007.

188 H. Tripathy, A. Balakrishnan, M. Chinthala and A. Kumar, *Ind. Eng. Chem. Res.*, 2024, **63**, 20125–20143.

189 S. Patnaik, D. P. Sahoo and K. Parida, *Carbon N. Y.*, 2021, **172**, 682–711.

190 P. Chen, X. Dong, M. Huang, K. Li, L. Xiao, J. Sheng, S. Chen, Y. Zhou and F. Dong, *ACS Catal.*, 2022, **12**, 4560–4570.

191 D. Liu, L. Jiang, D. Chen, Z. Hao, B. Deng, Y. Sun, X. Liu, B. Jia, L. Chen and H. Liu, *ACS Catal.*, 2024, **14**, 5326–5343.

192 C. Shi, L. Zhang, Z. Shi, J. Ma and Z. Wang, *Ind. Crops Prod.*, 2022, **186**, 115223.

193 H. Maimaiti, A. Awati, G. Yisilamu, D. Zhang and S. Wang, *Appl. Surf. Sci.*, 2019, **466**, 535–544.

194 J. Li, Y. Xiao, S. Gu, K. Wu, X. Zhao, X. Zhao, J. Nan and X. Xiao, *Chem. Eng. J.*, 2024, **480**, 147969.

195 L. Wang, L. Zang, F. Shen, J. Wang, Z. Yang, Y. Zhang and L. Sun, *J. Colloid Interface Sci.*, 2022, **622**, 336–346.

196 Y. Sun, Y. Ahmadi, K.-H. Kim and J. Lee, *Renew. Sustain. Energy Rev.*, 2022, **170**, 112967.

197 J. Liu, S. Wang, C. Zhao and J. Zheng, *MDPI*, 2023, DOI: 10.3390/nano13030499.

198 Z. Shen, F. Li, J. Lu, Z. Wang, R. Li, X. Zhang, C. Zhang, Y. Wang, Y. Wang, Z. Lv, J. Liu and C. Fan, *J. Colloid Interface Sci.*, 2021, **584**, 174–181.

199 Z.-Y. Wang, B. Yuan, F.-G. Zhang, Y. Chen, J.-P. Tang, L. Bao and Y.-J. Yuan, *Inorg. Chem.*, 2024, **63**, 9715–9719.

200 A. Balakrishnan, E. S. Kunnel, R. Sasidharan, M. Chinthala and A. Kumar, *ACS Sustain. Chem. Eng.*, DOI:10.1021/acssuschemeng.3c07961.

201 T. Liu, L. Sun, Z. Cao, Y. Xue, X. Lu, C. Yao and X. Li, *J. Alloys Compd.*, 2023, **962**, 171181.

202 A. Balakrishnan, S. Appunni, M. Chinthala, M. M. Jacob, D. V. N. Vo, S. S. Reddy and E. S. Kunnel, *Environ. Chem. Lett.*, DOI:10.1007/s10311-023-01563-9.

203 A. Balakrishnan, S. Appunni, M. Chinthala and D. Viet, *Environ. Chem. Lett.*, DOI:10.1007/s10311-022-01443-8.

204 H. Liu, C. Wang and G. Wang, *Chem. – An Asian J.*, 2020, **15**, 3239–3253.

205 X. Yan, M. Chen, J. Wang, Z. Wang, R. Xin, D. Wu, Y. Song, S. Li, W. Zhu, C. Wang and Y. Mao, *Chem.*

View Article Online
DOI: 10.1039/D5TA07511D

Eng. J., 2024, **495**, 153431.

206 M. Li, P. Zhang, J. Mao, J. Li, D. Wang, B. Xu, J. Zhou, J. Zhang, Q. Cao, Y. Zhang and H. Xiao, *Desalination*, 2025, **600**, 118497.

207 L. Tian, Y. Feng, X. Chen, H. Wang, J. Lin, W. Shi, L. Wei, W. Xia, Q. Sun, Y. Yang and Y. Li, *Int. J. Biol. Macromol.*, 2025, **286**, 138377.

208 J. Lin, D. Gao, J. Zeng, Z. Li, Z. Wen, F. Ke, Z. Xia and D. Wang, *Int. J. Biol. Macromol.*, 2024, **269**, 131994.

209 Y. Wang, J. Yang, Z. Zhang, P. Zhao, Y. Chen, Y. Guo and X. Luo, *Int. J. Biol. Macromol.*, 2024, **269**, 131885.

210 B. Sarkodie, E. K. Howard, Q. Feng, C. Xu and Y. Hu, *Ceram. Int.*, 2024, **50**, 21951–21957.

211 M. Ezzine, A. S. El-Shafie, K. M. Youssef and M. El-Azazy, *Int. J. Biol. Macromol.*, 2025, **306**, 141753.

212 J. Li, Y. Ning, X. Liu, X. Ren and W. Liu, *Cellulose*, 2024, **31**, 1827–1841.

213 X. Yang, C. Hu, X. An, X. Chen and C. Ding, *J. Alloys Compd.*, 2024, **1003**, 175594.

214 A. Saha and S. Varanasi, *Appl. Nanosci.*, 2024, **14**, 675–686.

215 L. Kumalayanti, W. Khamhom, N. Chankhunthod, P. Kidkhunthod and S. Pinitsoontorn, *Radiat. Phys. Chem.*, 2024, **221**, 111757.

216 N. P. de Moraes, R. A. Pereira, T. V. C. da Silva, B. H. B. da Silva, G. P. de Assis, T. M. B. Campos, G. P. Thim, M. R. de Vasconcelos Lanza, L. de Freitas and L. A. Rodrigues, *Int. J. Biol. Macromol.*, 2024, **254**, 127826.

217 X. Qi, X. Xiong, H. Cai, X. Zhang, Q. Ma, H. Tan, X. Guo and H. Lv, *Carbohydr. Polym.*, 2024, **346**, 122601.

218 W. Leng, X. Jiang, S. He, X. Wang, S. Zhai, J. Shi and X. Zhang, *Int. J. Biol. Macromol.*, 2024, **283**, 137948.

219 M. Bansal and B. Pal, *Int. J. Biol. Macromol.*, 2025, **285**, 138329.

220 V.-D. Doan, T. T. N. Nguyen, H. A. Le Pham, T. L. H. Nguyen, O. E. Lebedeva, H. P. Dang, A.-T. Nguyen, V. A. Tran and V. T. Le, *J. Mol. Liq.*, 2024, **398**, 124261.

221 W. Cui, S. Luo, H. Hou, Z. Wu, B. An, M. Xu, C. Ma, S. Liu and W. Li, *Ceram. Int.*, 2024, **50**, 52218–52227.

222 S. Elbakry, F. A. Alharthi, A. A. Abutaleb, M. Alshareef, K. Althumayri and M. E. A. Ali, *J. Mater. Res.*, 2024, **39**, 3218–3231.

View Article Online
DOI: 10.1039/D5TA07511D

223 X. Yang, Y. Ci, P. Zhu, T. Chen, F. Li and Y. Tang, *Int. J. Biol. Macromol.*, 2024, **274**, 133201.

224 P. Charurungsipong, B. Than-ardna and H. Manuspiya, *Int. J. Biol. Macromol.*, 2024, **283**, 137738.

225 C. Duan, X. Liu, G. Tian, D. Zhang, Y. Wen, Y. Che, Z. Xie and Y. Ni, *Int. J. Biol. Macromol.*, 2024, **274**, 133317.

226 Y. Peng, H. Zhou, Y. Wu, Z. Ma, R. Zhang, H. Tu and L. Jiang, *J. Colloid Interface Sci.*, 2022, **609**, 188–199.

227 M. N. Morshed, S. Al Azad, H. Deb, B. B. Shaun and X. L. Shen, *J. Water Process Eng.*, 2020, **33**, 101062.

228 Z. Lin and J. Huang, *Sep. Purif. Technol.*, 2021, **264**, 118427.

229 L. Lebogang, R. Bosigo, K. Lefatshe and C. Muiva, *Mater. Chem. Phys.*, 2019, **236**, 121756.

230 D. Wang, J. Yang, H. Yang, P. Zhao and Z. Shi, *Carbohydr. Polym.*, 2022, **296**, 119960.

231 S. I. Othman, H. E. Alfassam, H. A. Alqhtani, M. A. Al-Waili, A. A. Allam and M. R. Abukhadra, *Int. J. Biol. Macromol.*, 2024, **265**, 130615.

232 J.-L. Zhu, M.-L. Wang, S.-C. Shi, J.-X. Ren, H.-D. Huang, W. Lin and Z.-M. Li, *Cellulose*, 2022, **29**, 1929–1942.

233 Y. Li, H. Cao, W. Liu and P. Liu, *Chemosphere*, 2022, **307**, 135665.

234 J. Gao, W. Chen, H. Shi, Z. Li, L. Jing, C. Hou, J. Wang and Y. Wang, *Surfaces and Interfaces*, 2022, **34**, 102302.

235 Z. Zhao, X. Cai, S. Fan, Y. Zhang, Z. Huang, H. Hu, J. Liang and Y. Qin, *J. Alloys Compd.*, 2021, **877**, 160260.

236 S. Patial, Sonu, S. Thakur, Q. Van Le, T. Ahamad, P. Singh, V.-H. Nguyen, A. A. P. Khan, C. M. Hussain and P. Raizada, *J. Taiwan Inst. Chem. Eng.*, 2023, **153**, 105189.

237 X. Yan and X. Qian, *Int. J. Biol. Macromol.*, 2024, **283**, 137978.

238 Y. Chen, R. Su, F. Wang, W. Zhou, B. Gao, Q. Yue and Q. Li, *Chemosphere*, 2021, **270**, 129295.

239 T. T. Van Nguyen, Q. K. Nguyen, N. Q. Thieu, H. D. T. Nguyen, T. G. T. Ho, B. L. Do, T. T. P. Pham, T. Nguyen and H. Ky Phuong Ha, *Heliyon*, DOI:10.1016/j.heliyon.2023.e22319.

240 D. Karadeniz, N. Kahya and F. B. Erim, *J. Photochem. Photobiol. A Chem.*, 2022, **428**, 113867.

241 W. Chen, T. Zhou, D. Gu, Y. He, Z. Zhang, J. Tian and F. Fu, *Appl. Surf. Sci.*, 2023, **637**, 157955.

242 K. Li, X. Zhang, X. Huang, X. Li, Q. Chang, J. Wang, S. Deng and G. Zhu, *Environ. Sci. Pollut. Res.*, 2024, **31**, 23924–23941.

View Article Online
DOI: 10.1039/D5TA07511D

243 G. Tian, C. Duan, B. Zhou, C. Tian, Q. Wang and J. Chen, *Front. Chem. Sci. Eng.*, 2023, **17**, 930–941.

244 G. Wu, S. Bian, J. Wang, T. Xu, Y. Pan, J. Han, W. Xing and H. Bian, *J. Mol. Struct.*, 2025, **1340**, 142613.

245 K. Li, X. Zhang, J. Wang, L. Guo, S. Deng, T. Xie, J. Wang and G. Zhu, *J. Photochem. Photobiol. A Chem.*, 2026, **470**, 116616.

246 C. Wu, T. Guo, Y. Chen, Q. Tian, Y. Zhang, Z. Huang, H. Hu and T. Gan, *Sep. Purif. Technol.*, 2024, **329**, 125174.

247 K. Li, X. Zhang, X. Huang, X. Li, Q. Chang, S. Deng and G. Zhu, *J. Water Process Eng.*, 2024, **63**, 105442.

248 N. Thi Mai, D. Van Thanh, N. Nhat Huy, D. Danh Bich, T. Thi Minh Hang, N. Huu Hao and N. Manh Khai, *Sep. Purif. Technol.*, 2025, **354**, 129039.

249 Y. Peng, H. Tang, B. Yao, X. Gao, X. Yang and Y. Zhou, *Chem. Eng. J.*, 2021, **414**, 128800.

250 X. Li, B. Jie, H. Lin, Z. Deng, J. Qian, Y. Yang and X. Zhang, *J. Environ. Manage.*, 2022, **308**, 114664.

251 F. Ghanbari and M. Moradi, *Chem. Eng. J.*, 2017, **310**, 41–62.

252 G. Tian, C. Duan, S. Che, B. Zhao, B. Zhou and Y. Ni, *Sep. Purif. Technol.*, 2025, **354**, 129183.

253 W. Ren, J. Gao, C. Lei, Y. Xie, Y. Cai, Q. Ni and J. Yao, *Chem. Eng. J.*, 2018, **349**, 766–774.

254 Y. Wu, Y. Li, T. Zhao, X. Wang, V. I. Isaeva, L. M. Kustov, J. Yao and J. Gao, *Carbohydr. Polym.*, 2022, **296**, 119969.

255 Y.-D. Dong, L.-Q. Zhang, P. Zhou, Y. Liu, H. Lin, G.-J. Zhong, G. Yao, Z.-M. Li and B. Lai, *J. Hazard. Mater.*, 2022, **423**, 127054.

256 Y. Han, L. Gan, H. Gong, J. Han, W. Qiao and L. Xu, *Biochar*, 2022, **4**, 35.

257 W. Yang, L. Yang, Y. Yang, C. Fu, C. Sheng and P. Zhang, *Cellulose*, 2024, **31**, 3221–3242.

258 L. Gan, Q. Zhong, A. Geng, L. Wang, C. Song, S. Han, J. Cui and L. Xu, *Sci. Total Environ.*, 2019, **694**, 133705.

259 Z. Zhang, J. Wang, H. Zhang, Y. Deng, B. Tan, J. Wang, T. Yang and W. Wang, *Appl. Surf. Sci.*, 2024, **671**, 160717.

260 F. Nekouei, S. Nekouei and H. Kargarzadeh, *Chem. Eng. J.*, 2018, **335**, 567–578.

261 K. Zheng and L. Xiao, *Int. J. Biol. Macromol.*, 2023, **248**, 125902.

262 W. Sun, K. Thummavichai, D. Chen, Y. Lei, H. Pan, T. Song, N. Wang and Y. Zhu, *Polymers (Basel).*, 2021, **13**, 1–14.

View Article Online
DOI: 10.1039/D5TA07511D

263 R. Su, Z. Wang, M. Zhao, F. Xiao, L. Zhang, L. Yang, Z. Wu, J. Bai and P. He, *J. Alloys Compd.*, 2023, **968**, 171896.

264 Y. Lin, Q. Wang, Y. Huang, J. Du, Y. Cheng, J. Lu, Y. Tao and H. Wang, *Int. J. Biol. Macromol.*, 2023, **247**, 125559.

265 Y. Wang, L. Ma, F. Xu, R. Ren, J. Wang and C. Hou, *Carbohydr. Polym.*, 2022, **298**, 120100.

266 X. Xue, Z. Sui, Y. Zou, C. Sun, F. Sefat, P. Coates, W. Zhang and C. Lu, *Carbohydr. Polym.*, 2025, **358**, 123508.

267 Y. Zhang, H. Zhang, J. Yao, Y. Song, W. Li and X. Xuan, *Chem. Eng. J.*, 2024, **483**, 149326.

268 S. Zhang, M. Zhao, H. Li, C. Hou and M. Du, *Cellulose*, 2021, **28**, 3585–3598.

269 J. He, A. Kumar, M. Khan and I. M. C. Lo, *Sci. Total Environ.*, 2021, **758**, 143953.

270 Y. Ding, G. Yang, S. Zheng, X. Gao, Z. Xiang, M. Gao, C. Wang, M. Liu and J. Zhong, *J. Environ. Manage.*, 2024, **366**, 121875.

271 K. Maślana, T. Kędzierski, A. Żywicka, B. Zielińska and E. Mijowska, *Environ. Nanotechnology, Monit. Manag.*, 2022, **17**, 100656.

272 J. Wang, C. Huang, Y. Tu, Z. Chen, Y. Zhao and Y. Ke, *Int. J. Biol. Macromol.*, 2025, **309**, 143019.

273 H. M. Abd El-Lateef, M. M. Khalaf, M. A. Alsaeed, M. F. Abou Taleb and M. Gouda, *Int. J. Biol. Macromol.*, 2024, **282**, 137410.

274 C. Huang, M. Xiao, H. Cui, J. Wang, Y. Cai and Y. Ke, *Int. J. Biol. Macromol.*, 2023, **252**, 126495.

275 N. Janpetch, C. Vanichvattanadecha and R. Rujiravanit, *Cellulose*, 2015, **22**, 3321–3335.

276 H. Shen, S. Liao, C. Jiang, J. Zhang, Q. Wei, R. A. Ghiladi and Q. Wang, *Carbohydr. Polym.*, 2022, **277**, 118853.

277 L.-P. Liu, X.-N. Yang, L. Ye, D.-D. Xue, M. Liu, S.-R. Jia, Y. Hou, L.-Q. Chu and C. Zhong, *Carbohydr. Polym.*, 2017, **174**, 1078–1086.

278 Y. D. Chai, Y. L. Pang, S. Lim and W. C. Chong, *Mater. Today Proc.*, 2021, **42**, 50–55.

279 M. Bachmann and M. Bachmann, *From Life Cycle Assessment to Absolute Environmental Sustainability of Plastics from Alternative Carbon Feedstocks Von der Lebenszyklusanalyse zu absoluter ¨okologischer Nachhaltigkeit von Kunststoffen aus alternativen Kohlenstoffquellen*, .

280 A. Sudheshwar, K. Vogel, G. Nyström, N. Malinverno, M. Arnaudo, G. Enrique, R. Hischier and C. Som, 2024, 1487–1497.

View Article Online
DOI: 10.1039/D5TA07511D

281 F. Foroughi, E. R. Ghomi, F. M. Dehaghi and R. Borayek, 2021, 1–22.

282 P. G. Stampino, L. Riva, C. Punta, G. Elegir, D. Bussini and G. Dotelli, 2021, 1–20.

283 A. salah omer, G. A.El Naeem, A. I. Abd-Elhamid, O. O.M. Farahat, A. A. El-Bardan, H. M.A. Soliman and A. A. Nayl, *J. Mater. Res. Technol.*, 2022, **19**, 3241–3254.

284 A. Wilcox, M. Hall, J. Menzies, N. Yates, J. Price, T. Neal, S. Stilianoudakis, S. Isaacs, Y. Sun, M. Sivik and K. McDonough, *Sci. Total Environ.*, 2025, **991**, 179942.

285 J. Belhaj, R. Khiari, V. García-caballero, A. A. Romero and A. García, 2025, 1–23.

286 A. Singh, J. G. Vijayan and K. G. Moodley, *Surface Functionalizations of Nanocellulose for Wastewater Treatment*, .

287 A. Sánchez-Yepes, A. Santos, J. M. Rosas, J. Rodríguez-Mirasol, T. Cordero and D. Lorenzo, *Chemosphere*, 2023, **341**, 140047.

288 J. Shaheen, Y. H. Fseha and B. Sizirici, *Heliyon*, DOI:10.1016/j.heliyon.2022.e12388.

289 X. Li, L. Zhang, Z. Wang, S. Wu and J. Ma, *Colloids Surfaces A Physicochem. Eng. Asp.*, 2022, **636**, 128156.

290 Y.-Y. Dong, Y.-H. Zhu, M.-G. Ma, Q. Liu and W.-Q. He, *Sci. Rep.*, 2021, **11**, 3366.

291 F. business Reports, Cellullose Market, https://www.fortunebusinessinsights.com/cellulose-market-102062.

Data available on request from the authors.

View Article Online
DOI: 10.1039/D5TA07511D